QUANTUM CHAOS USING DELTA KICKED SYSTEMS

By

VIJAYASHANKAR RAMAREDDY

Bachelor of Science
Bangalore University
Bangalore, India
1999

Master of Science in Physics
Bangalore University
Bangalore, India
2001

Submitted to the Faculty of the
Graduate College of
Oklahoma State University
in partial fulfillment of
the requirements for
the Degree of
DOCTOR OF PHILOSOPHY
December, 2008

QUANTUM CHAOS USING DELTA KICKED SYSTEMS

Dissertation Approved:

Dr. Gil S. Summy

Dissertation advisor

Dr. Girish S. Agarwal, FRS

Dr. James P. Wicksted

Dr. Paul A. Westhaus

Dr. Neil Shafer-Ray

Dr. Lionel M. Raff

Dr. A. Gordon Emslie

Dean of the Graduate College

ACKNOWLEDGMENTS

First of all I would like to thank my advisor Dr. Gil Summy who gave his students all the freedom they want and created the best environment in the lab.

I would like to thank my parents Rama Reddy and Suguna Rama Reddy, my uncle Narayana Reddy and brothers and sister for their support and encouragement throughout my studies.

An important person who encouraged me and advised me throughout my PhD studies with his vast experience at OSU and knowledge in physics is Prof. N. V. V. J. Swamy. His tips have been extremely helpful in all the exams and courses I had at OSU and also in planning my career. He made a free translation of original German articles of Albert Einstein on BEC for me.

During my five years of stay at OSU, I have worked with Brian, Peyman, Ghazal, and Ishan, in the OSU BEC lab. I learnt most of my instrumentation and programming using Matlab and Labview from Brian. Peyman is very enthymatic and hard working person from whom I benefitted a lot in getting settled in the lab. Ghazal was a nice addition to our team in the lab who made the working place a lively and fun environment. Finally I would like to thank Ishan who joined the lab much later. Ishan happens to be my room mate as well.

The physics department office at OSU has the best staff Cindy, Susan and Danyelle who are extremely helpful and friendly. Warren is another nice addition to our staff. If we need a power supply or BNC cable or a computer, Warren is the person we contact first. I have worked with Melissa and she is extremely friendly She doesn't treat her TAs with authority. Finally I would like to thank Mike Lucas and his staff.

When we wanted some part for our experiments, we need to tell him our needs and he designs and builds one.

I was fortunate that I took courses of most of the faculty in physics department at OSU. I enjoyed all the lectures of the great faculty we have.

I would like to extend my special thanks to our former graduate coordinator, Professor Paul Westhaus and present graduate coordinator Bob Haunsein. Prof. Paul Westhaus would go to any extent to help students. When a new international student arrives, Prof. Paul Westhaus would take all the responsibilities till the student is settled in Stillwater. I am sure Prof. Haunstein will continue the tradition.

I would like to acknowledge the contributions of my dissertation committee members Prof. G. Summy, Prof. G. Agarwal, FRS, Prof. J. Wicksted, Prof. P. Westhaus, Prof. N. shafer-Ray, and Prof. L. Raff.

Finally I would like to thank Dr Anita Goel, CEO of Nanobiosym for letting me use the conference room at Nanobiosym to write my thesis.

I would like to thank my friends in Stillwater, fellow graduate students for their support and encouragement and making my stay in Stillwater a memorable experience.

TABLE OF CONTENTS

LIST OF TABLES

Table Page

LIST OF FIGURES

CHAPTER 1

Introduction

"It may happen that small differences in the initial conditions produce very great ones in the final phenomena. A small error in the former will produce an enormous error in the latter. Prediction becomes impossible, and we have the fortuitous phenomenon."—-Henri Poincarè

As far back as 1885, King Oscar II of Sweden established a prize for the person who could produce a solution to the "three body problem" in the context of stability of the solar system. The prize was ultimately awarded to Henri Poincarè even though he did not quite solve the puzzle. He identified for the first time that there can be non-periodic orbits that neither increase forever nor approach a fixed point. This was the starting point for what we now know as "chaos". Poincarè's work led to the understanding of mathematical spaces now known as manifolds an important part of chaos. The next major progress in the field of chaos occurred in 1961 when Edward Lorenz [1] serendipitously noticed odd behavior in a numerical model of the atmosphere running on a simple digital computer. He soon realized that the difference between what should have been identical simulations was the result of rounding numbers to three significant figures when the program was reset in the middle. At one point he stopped the simulation and then restarted it, using as initial conditions the results obtained when the program was stopped. Surprisingly the final result of the simulation was completely different to what was found if it ran without interruption. Thus Lorenz discovered that long time weather predictions are exquisitely sensitive to the initial conditions that are used.

Perhaps the signature feature of chaotic motion is its sensitivity to initial conditions [2]. One way of parameterizing this sensitivity is through the Lyapunov exponent which quantifies the divergence of two arbitrarily close initial conditions separated in phase space by δx_0. The time evolution of the difference $\delta x(t)$ is given by

$$\delta x(t) \sim \delta x_0 e^{\lambda_L t}, \tag{1.1}$$

where λ_L is the Lyapunov exponent. For $\lambda_L > 0$, the motion is chaotic. For $t > 1/\lambda_L$, the chaos becomes appreciable. For $\lambda_L < 0$, the motion is regular and the evolution is drawn towards a fixed point in phase space. For chaotic systems, two nearby close initial conditions diverge exponentially. Once the separation between them reaches the size of the phase space, they effectively evolve randomly. This classical chaos has been identified in such diverse fields as chemical reactions [3], laser physics [4], plasma physics [5], and Economics [6].

1.1 Quantum Chaos

The development of quantum mechanics was a major step towards the development of our current understanding of nature. Quantum mechanics allows the description of both matter and radiation using particle and wave behavior. One important consideration is that any result determined using quantum mechanics, often reduces to the classical result as a limit. Ehrnfest's theorem gives the correspondence. One key area where it is difficult to see how classical and quantum mechanics can be compatible is chaos. In the quantum world, chaos can not be defined in the same sense as it is defined in classical dynamics (i.e. through a Lyapunov exponent) since the evolution operator in quantum mechanics is unitary. Thus two initially close states will not diverge exponentially as is the case in a classically chaotic system. To circumvent this difficulty, alternative definitions of chaos have been proposed. For example, Peres [7] suggested observing the overlap of two states after interacting with slightly differing

potentials. The potential chosen is of course important.

In the context of quantum chaos, the δ-kicked rotor model has been extensively used. It has served as a paradigm for quantum chaos ever since it was first studied classically by B. V. Chirikov [8] and quantum mechanically by G. Casati *et al.* [9]. This system has attracted so much attention since its classical and quantum mechanical dynamics can be analytically handled with relative ease. The classical δ-kicked rotor displays chaotic behavior for certain parameter regimes, while the quantum δ-kicked rotor exhibits the phenomena of quantum resonance, quantum anti-resonance and dynamical localization (see chapter 7).

The quantum δ-kicked rotor was first realized in experiments on microwave ionization of highly excited Hydrogen atoms [10, 11]. Despite early success with the microwave system, it was relatively inflexible and difficult to implement. Ultimately the search for a more versatile version of the quantum δ-kicked rotor led to the field of atom optics.

The atom optics version of the quantum δ-kicked rotor was first realized by Mark Raizen *et al.* using cold atoms subjected to a modulated standing wave of off-resonant light [12-14] and they initiated the study of quantum chaos [15-25]. Since the Raizen group's first experiments several other research groups have investigated quantum chaos using this system. For example, Phillips and coworkers at NIST studied the Talbot effect and the related topic of quantum resonances [26-28] The quantum chaos group at the University of Lille, have looked at the effect of two kicking frequencies on dynamical localization. They observed that if the ratio of the two kicking frequencies is a rational fraction, then dynamical localization is retained [29, 30]. A group at the University of Auckland have examined quantum chaos in the presence of decoherence which is introduced by either noise in the amplitude of the kicking potential or the addition of spontaneous emission into the kicking light [31, 32]. A group of researchers at University College London realized the quantum δ-kicked rotor using

cold atoms and studied the quantum ratchet [33-35]. A group in Japan used the Bose-Einstein Condensation of Rb-87 atoms to realize the kicked rotor and study the quantum ratchet mechanism [36] at the same time we started our work on ratchet (see Chapter 7). However, they restrict them selves to small changes in mean momentum, so that the saturation of mean momentum was not observed in their experiments. Furthermore, the work described in Chapter 7 is superior to that of Japanese group since we realized the ratchet at arbitrary quasimomenta.

The realization of the atom optics version of the quantum δ-kicked rotor has also enabled variants of the kicked rotor to be produced. Raizen and coworkers have used the kicked rotor with an additional linear potential to study the Wannier-Stark and Landau Zener tunneling problems [37-43]. Later a group at the University of Oxford started work on the quantum δ-kicked accelerator using cold Cs atoms and studied its properties [44-53]. This thesis reports the realization of the kicked rotor and kicked accelerator and the study of associated resonances using a Bose-Einstein Condensation (BEC) of Rb-87 atoms.

1.2 Bose-Einstein Condensation

The history of BEC begins with Satyendra Nath Bose in 1924, who used the concept of a photon gas and devised the statistics now known as Bose-Einstein statistics and succeeded in establishing Planck's radiation formula on this basis [54]. Later Einstein generalized Bose's idea to particles of integer spin, now known as Bosons. In 1925, Einstein found that (under certain circumstances) there can be a macroscopic occupation of the entire population in the ground state [55-57], now known as Bose-Einstein Condensation. The prediction of BEC was the last major discovery of Albert Einstein. For 70 years after its prediction, except for the indirect evidence of BEC in experiments on liquid Helium [58, 59], it was only a theoretical concept. It was not until 1995 that BEC was finally realized in dilute gases in a remarkable series

of experiments separately conducted by groups at JILA [60] and MIT [61]. A good review article on BEC can be found in reference [62]

The journey towards BEC in dilute atomic samples was long and on the way it led to a greater understanding of atom optics. Ashkin proposed the idea of light exerting a force on particles [63]. Ashkin's proposal is considered to be the starting point of laser cooling and the mechanical manipulation of matter with light (e.g. optical tweezers). Laser cooling was first demonstrated in trapped ions [64, 65], with later work by Phillips demonstrating a method of slowing a beam of atoms using what is now known as a Zeeman slower [66, 67], and magnetically trapping neutral atoms [68]. Steven Chu developed the idea of laser cooling of neutral atoms using six counter propagating laser beams [69] and trapped them using a focused laser beam [70], demonstrating the ideas of optical molasses and dipole trap. In 1987, Chu and co-workers [71] realized the Magneto-Optic Trap (MOT), which has since become the starting point for almost all laser cooling and BEC experiments to this day.

The standard MOT configuration involves using six counter propagating laser beams to cool and trap the atoms in a spatially varying magnetic field. The cooling involves absorbing a photon from a laser beam and then emitting it into random direction via spontaneous emission. This results in the slowing of the atom after many such absorptions and emissions. However the emission into random directions also produces a heating effect. The cooling and subsequent heating sets a limit on the lowest achievable temperature known as the Doppler limit. The MOT was expected to produce a cooling up to, at the most, the Doppler limit. When Phillips and coworkers measured the temperature of the cold cloud in the MOT, the measured temperature was to their surprise much lower than the Doppler limit [72]. This became a basis for the discovery of a new process that occurs in the laser cooling called Sisyphus cooling or polarization gradient cooling [73]. In current experiments, temperatures of the order of a few micro Kelvin can be achieved in a MOT. However

the temperatures and densities achievable in a MOT are not sufficient to realize Bose-Einstein Condensation. Finally, in 1995 a new two-stage cooling technique resulted in a BEC [60, 61]. In these experiments, atoms were first loaded into MOT, then transferred to a magnetic trap and finally evaporatively cooled by selectively removing the most energetic atoms using rf radiation [74, 75]. The group at JILA used a Time Orbiting Potential (TOP) trap [60] to achieve the BEC, while the group at MIT used an optical plug trap to realize the BEC [61]. The atomic physics community quickly turned to testing fundamental physics using this new tool and the field of atom optics has undergone a rapid growth.

1.3 Thesis organization

To study quantum chaos, the δ-kicked rotor (DKR) and the δ-kicked accelerator (DKA) were used. The classical evolution of these kicked systems shows that for some parameter regime, the dynamics becomes chaotic. The quantum evolution of these kicked systems can be studied using Floquet operators. The quantum dynamics shows that resonances occur for kicking periods at rational fraction of a characteristic time known as the half-Talbot time (see Chapter 2). The dynamics near these resonances can be described using a classical picture with an effective Planck's constant related to the separation of the kicking period from the resonances [76, 77]. A study of the quantum dynamics near these resonances for the DKA was undertaken in this thesis. For a quantum DKA, Quantum Accelerator Modes (QAMs) are formed near the resonances. To understand the QAMs, a momentum distribution narrower than a photon recoil is desired. Thus using a BEC is highly desirable. Two experiments were undertaken in the lab at the same time. One experiment was to achieve BEC and the other experiment was to obtain Magneto-Optic Trap (MOT) and kick the cold atoms to produce QAMs. Later these were unified to kick a BEC. In Chapter 2, the theory of QAM is discussed. Two equivalent pictures, the rephasing model

and the ϵ-classical model are discussed. Chapter 3 deals with the kicking of the cold atoms and producing the QAM in cold uncondensed Rubidium atoms. Details of the experimental configuration are given and numerical simulations are used to understand the experimental results. In Chapter 4, a mechanism of achieving a BEC is given. In this process, the observation of multiple micro-optical traps produced by spherical aberration of a lens is discussed. In Chapter 5 the kicking of BEC using standing wave pulses to produce QAMs is presented. Phase space plots described by the effective classical description of the kicked accelerator are mapped onto the quantum dynamics in this Chapter. In Chapter 6, the observation of resonances for kicking periods near rational fractions of the half-Talbot time are reported and a generalized ϵ-classical theory is outlined. The rephasing theory is generalized in this Chapter to include all resonances. The direct observation of the fractional Talbot effect in atom optics is reported. In Chapter 7, the resonances of the quantum δ-kicked rotor are used to produce the quantum ratchet. Both the classical and quantum dynamics of the kicked rotor are outlined before the experimental details to realize the quantum ratchet are discussed. The quantum ratchet using the quantum δ-kicked accelerator is described in Chapter 8. The theory predicts that the ratchet exists only for certain values of the acceleration and the kicks. This is qualitatively verified. Finally in Chapter 9, the conclusions are drawn and the future experiments that can be designed with the existing understanding of the theory and experimental developments are discussed.

CHAPTER 2

Theory of the Quantum δ-Kicked Accelerator

2.1 Introduction

The quantum δ-kicked rotor first realized in an atom optical system by M. Raizen's group [13] was the begining of experimental studies of kicked systems and the Talbot effect for matter waves. A series of experiments were then undertaken by a group at the university of Oxford using a variant of the kicked rotor [44] in which a linear potential was added to the kicking potential. This system is referred to as the δ-kicked accelerator. The resonances in the quantum δ-kicked accelerator (QDKA) are inferred through the observation of quantum accelerator modes (QAMs) which are formed when the time period is close to a rational fraction of the half-Talbot time. The QAMs are identified by linear growth of momentum with kicks of certain atoms (see Fig. 3.9). The Oxford group observed the QAM at the primary resonances which occur when the kicking period is close to integer multiples of the half Talbot time. These are referred to as the primary QAMs (for simplicity, the term QAM will be used to refer to the primary QAM until Chapter 5). The Oxford group also developed a simple picture of the QAM using the rephasing of the momentum states [45], which was followed by a more detailed theory of the QAMs developed by Fishman, Guarnari and Rebizzini [76, 77]. This latter theory, referred to as the ϵ-classical theory describes the QAM in terms of a classical picture with a corresponding set of classical equations of motion. This chapter provides details of the theory of QAM, discussing both rephasing and ϵ-classical models. In section 2.2, the Hamiltonian of the quantum δ-kicked accelerator is detailed. The classical evolution of the δ-kicked accelerator is discussed in section

2.3. The evolution of a plane wave under this time dependent Hamiltonian using the Floquet operators is discussed in section 2.4. The dynamics will be simplified in a free falling frame (FFF) that is accelerating with the external acceleration experienced by atoms. Using the matrix elements of the evolution operators in the FFF, the rephasing model is reformulated in Section 2.5. Finally in Section 2.6, the ϵ-classical theory is presented and it is shown how in a phase space produced by the equations of motion, the QAMs correspond to stable islands in a chaotic sea.

2.2 The Hamiltonian

The quantum δ-kicked accelerator (QDKA) is realized by subjecting a sample of cold atoms to δ-function like pulses from a standing wave optical potential. The Hamiltonian of an atom of mass M interacting with such a sinusoidal potential pulsed with period T is given by,

$$\hat{H(t)} = \frac{\hat{P}^2}{2M} - Mg'\hat{X} + \hbar\phi_d \cos(G\hat{X}) \sum_{n_p=-\infty}^{\infty} \delta(t' - n_p T), \tag{2.1}$$

where P is the momentum, g' is the acceleration experienced by the atom (such as the one produced by gravity), X is the position of the atom, $\hbar$ is Planck's constant, $G = 4\pi/\lambda$ is called the grating wave vector, λ is the wavelength of the light used to make the standing wave, t' is the continuous time variable, and ϕ_d is called the phase modulation depth (representing the strength of the kicking). The parameter ϕ_d plays an important role in the classical dynamics of the kicked accelerator and is given by

$$\phi_d = \frac{U_{\max}\Delta t}{2\hbar}, \tag{2.2}$$

where Δt is the kicking pulse length and $U_{\max}$ is the amplitude of the potential corresponding to the maximum intensity of the standing wave and is given by

$$U_{\max} = \frac{\hbar\Omega^2}{4\delta_L}, \tag{2.3}$$

where Ω is the Rabi frequency between the ground and excited states, and δ_L is the detuning of the kicking laser light with respect to the atomic transition. It is convenient to go to dimensionless units for the development of the theory. In typical kicking experiments such as the ones described in this thesis, the standing wave imparts two photon recoils momentum in quanta of $\hbar G$. It is thus convenient to write the momentum in units of $\hbar G$ as $p = P/(\hbar G)$. The position variable is conveniently written in terms of the wavelength of the standing wave $x = GX$. Defining $\eta = Mg'T/(\hbar G)$, the momentum gain in time T due to the acceleration g', and $\tau = 2\pi T/T_{1/2}$, where $T_{1/2}$ is called the half-Talbot time given by

$$T_{1/2} = \frac{2\pi M}{\hbar G^2}, \tag{2.4}$$

the Hamiltonian in the dimensionless units is then given by

$$\mathcal{H} = \frac{\hat{p}^2}{2} - \frac{\eta}{\tau}\hat{x} + \phi_d \cos(\hat{x}) \sum_{n_p=-\infty}^{\infty} \delta(t - n_p\tau), \tag{2.5}$$

where $\mathcal{H} = H/\left(\hbar^2 G^2/M\right)$, and $t = 2\pi t'/T_{1/2}$ is the dimensionless continuous time variable.

2.3 Classical Evolution

Hamilton's equations of motion in the dimensionless units of Eq. (2.5) are then written,

$$\frac{\partial x}{\partial t} = \frac{\partial \mathcal{H}}{\partial p} \tag{2.6}$$

$$\frac{\partial p}{\partial t} = -\frac{\partial \mathcal{H}}{\partial x}. \tag{2.7}$$

To simplify the algebra of solving these equations, an assumption is made which corresponds to the Raman-Nath approximation in the quantum regime: when the pulse is on (for a duration ϵ_k which is infinitesimally small), the kinetic energy and the acceleration terms in the Hamiltonian of Eq. (2.5) can be ignored. Hamilton's

equation of motion in region ($0 \leq t \leq \epsilon_k$) are given by

$$\begin{aligned} \frac{\partial x}{\partial t} &= 0 \\ \frac{\partial p}{\partial t} &= \phi_d \sin(x)\delta(t - 0\tau). \end{aligned}$$

The dynamical variables x and p after the first kick are then given by

$$\begin{aligned} x(t = \epsilon_k) &= x(t = 0) \\ p(t = \epsilon_k) &= p(t = 0) + \phi_d \sin(x(t = 0)). \end{aligned} \tag{2.8}$$

For the region ($\epsilon_k \leq t \leq \tau$), the Hamilton's equations of motion become,

$$\begin{aligned} \frac{\partial x}{\partial t} &= p \\ \frac{\partial p}{\partial t} &= \frac{\eta}{\tau}. \end{aligned}$$

Integrating these equations results in

$$\begin{aligned} x(t = \tau) &= x(t = \epsilon_k) + p(t = \epsilon_k)(\tau - \epsilon_k) + \frac{\eta}{\tau}\left(\frac{\tau^2}{2} - \frac{\epsilon_k^2}{2}\right) \\ p(t = \tau) &= p(t = \epsilon_k) + \eta, \end{aligned} \tag{2.9}$$

Combining Eqs. (2.8) and (2.9) with $\epsilon_k \to 0$, one obtains the position and momentum of the particle after the first kick:

$$\begin{aligned} x_1 &= x_0 + \tau p_1 - \eta\tau/2, \\ p_1 &= p_0 + \phi_d \sin(x_0) + \eta, \end{aligned} \tag{2.10}$$

where x_0 and p_0 are the position and momentum before the first kick. To simplify further, defining the variables

$$p' = \tau(p - \eta/2), \tag{2.11}$$

and

$$\tilde{k'} = \tau\phi_d, \tag{2.12}$$

x and p' after one kick are given by

$$\begin{aligned} x_1 &= x_0 + p'_1, \\ p'_1 &= p'_0 + \tilde{k'}\sin(x_0) + \eta\tau. \end{aligned} \tag{2.13}$$

Solving these equations for second and later kicks, it is found that after $n_p + 1$ kicks (a kick includes kicking followed by a free evolution),

$$\begin{aligned} x_{n_p+1} &= x_{n_p} + p'_{n_p+1} \\ p'_{n_p+1} &= p'_{n_p} + \tilde{k'}\sin(x_{n_p}) + \eta\tau. \end{aligned} \tag{2.14}$$

This mapping is similar to the standard map [76] except for the constant shift $\eta\tau$ in the momentum variable. Thus the classical dynamics of the δ-kicked accelerator results in the map of Eq. (2.14) which are displayed in the phase-space portraits of Figs. 2.1 to 2.4. The value of the acceleration g' used in Figs. 2.1, 2.2, 2.3, and 2.4 are respectively, 0 ms^{-2}, 0.5 ms^{-2}, 1 ms^{-2} and 6 ms^{-2}. The value of $g' = 6$ ms^{-2} (*natural* value) corresponds to the experimental value used in chapter 5. This value is referred to as the *natural* value since in the experiments, the standing wave was oriented at an angle and the component of of gravitational acceleration in the direction of standing wave was 6 ms^{-2}. It should be noted that as g' increases, the phase space becomes more and more chaotic for small values of $\tilde{k'}$. In Chapter 5, these maps have been explored experimentally.

2.4 Quantum evolution

2.4.1 Floquet operators

The quantum evolution of the system is given by the kick-to-kick Floquet operator,

$$\begin{aligned} \hat{U} &= \hat{K}\hat{F}, \\ &= \mathrm{e}^{-i\phi_d\cos(\hat{x})}\hat{F}, \end{aligned} \tag{2.15}$$

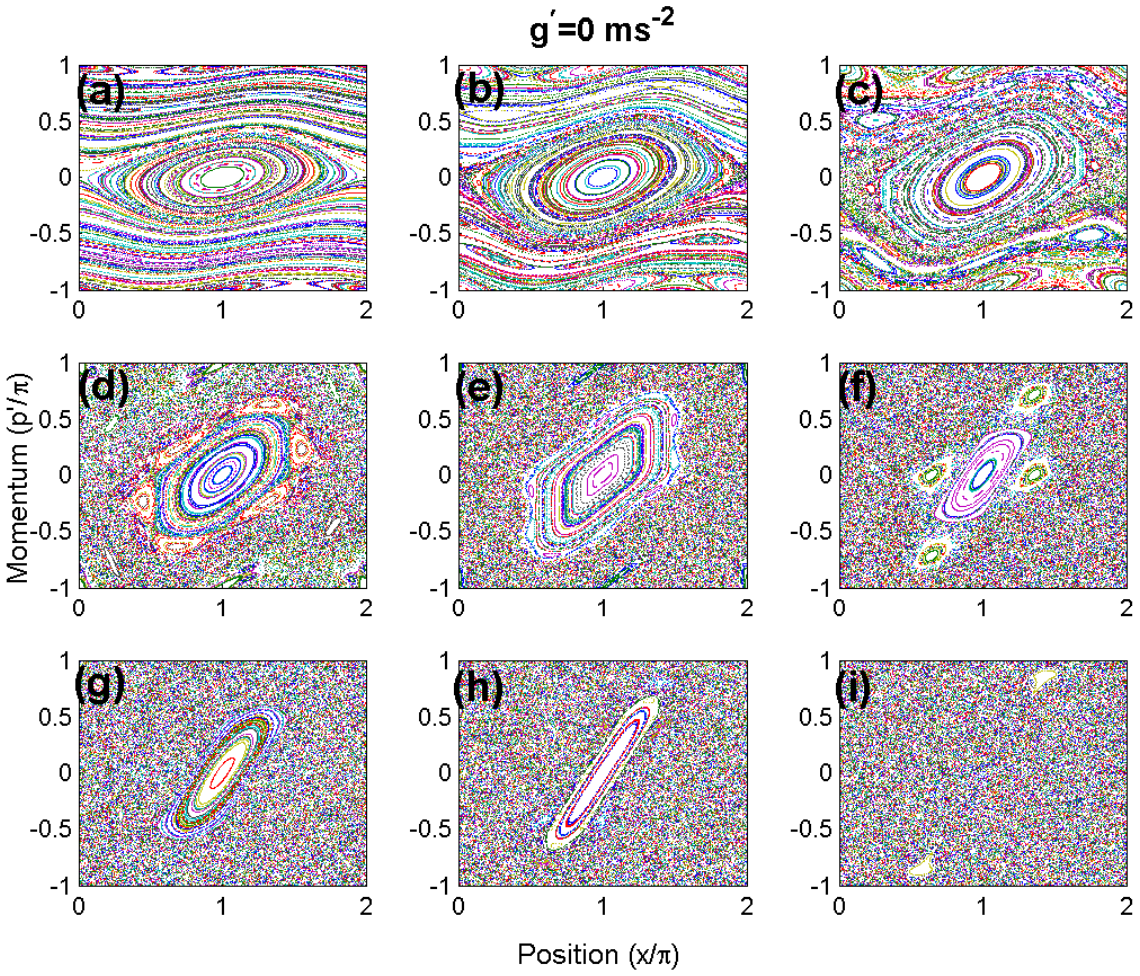

Figure 2.1: Phase space plots of the classical δ-kicked accelerator for $g' = 0$ ms^{-2} and $\tau = 2\pi$. The value of $\tilde{k'}$ used are (a) $\tilde{k'} = 0.4$, (b) $\tilde{k'} = 0.7$, (c) $\tilde{k'} = 1.0$, (d) $\tilde{k'} = 1.5$, (e) $\tilde{k'} = 2.0$, (f) $\tilde{k'} = 2.5$, (g) $\tilde{k'} = 3.0$, (h) $\tilde{k'} = 4.0$, and (i) $\tilde{k'} = 5.5$. For $\tilde{k'} = 0.4$, the dynamics are regular. As $\tilde{k'}$ increases, the regular region shrinks and for $\tilde{k'} > 5.5$, chaos is dominant.

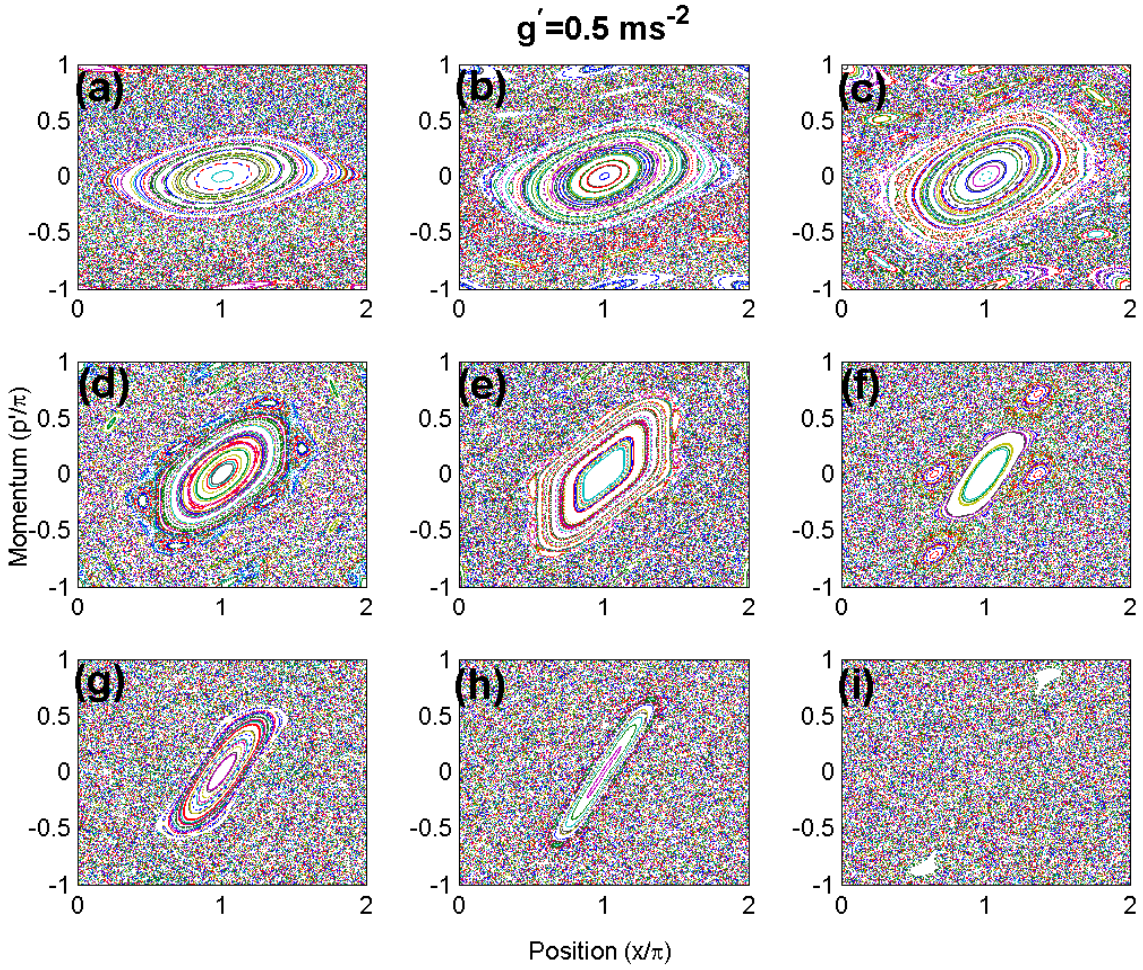

Figure 2.2: Phase space plots of the classical δ-kicked accelerator for $g' = 0.5$ ms^{-2} and $\tau = 2\pi$. The value of $\tilde{k}'$ used was (a) $\tilde{k}' = 0.4$, (b) $\tilde{k}' = 0.7$, (c) $\tilde{k}' = 1.0$, (d) $\tilde{k}' = 1.5$, (e) $\tilde{k}' = 2.0$, (f) $\tilde{k}' = 2.5$, (g) $\tilde{k}' = 3.0$, (h) $\tilde{k}' = 4.0$, and (i) $\tilde{k}' = 5.5$. Note that apart from g', the parameters used are same as in Fig 2.1. Thus the addition of a linear term in the potential (for small acceleration such as 0.5 ms^{-2}) increases the chaotic regions at small $\tilde{k}'$.

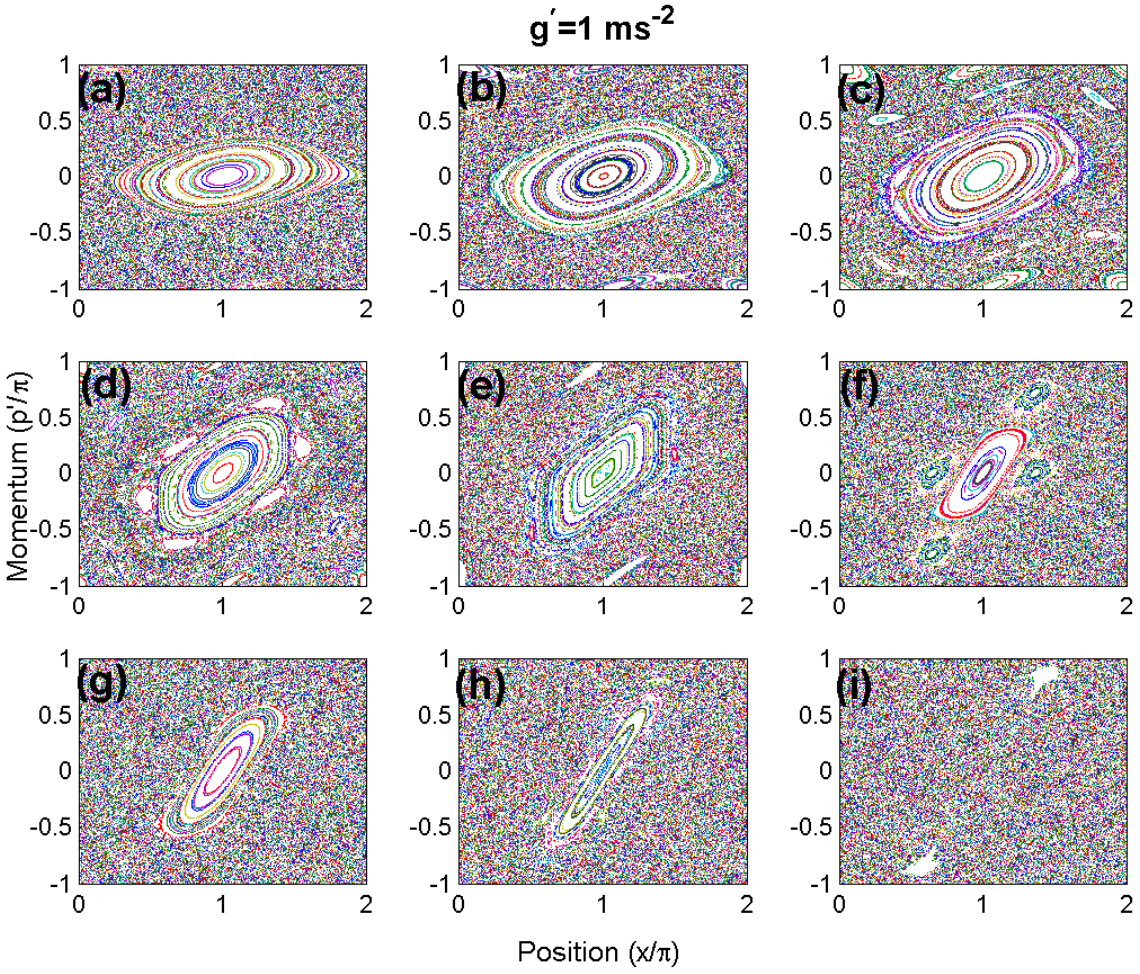

Figure 2.3: Phase space plots of the classical δ-kicked accelerator for $g' = 1$ ms^{-2} and $\tau = 2\pi$. The value of $\tilde{k}'$ used was (a) $\tilde{k}' = 0.4$, (b) $\tilde{k}' = 0.7$, (c) $\tilde{k}' = 1.0$, (d) $\tilde{k}' = 1.5$, (e) $\tilde{k}' = 2.0$, (f) $\tilde{k}' = 2.5$, (g) $\tilde{k}' = 3.0$, (h) $\tilde{k}' = 4.0$, and (i) $\tilde{k}' = 5.5$.

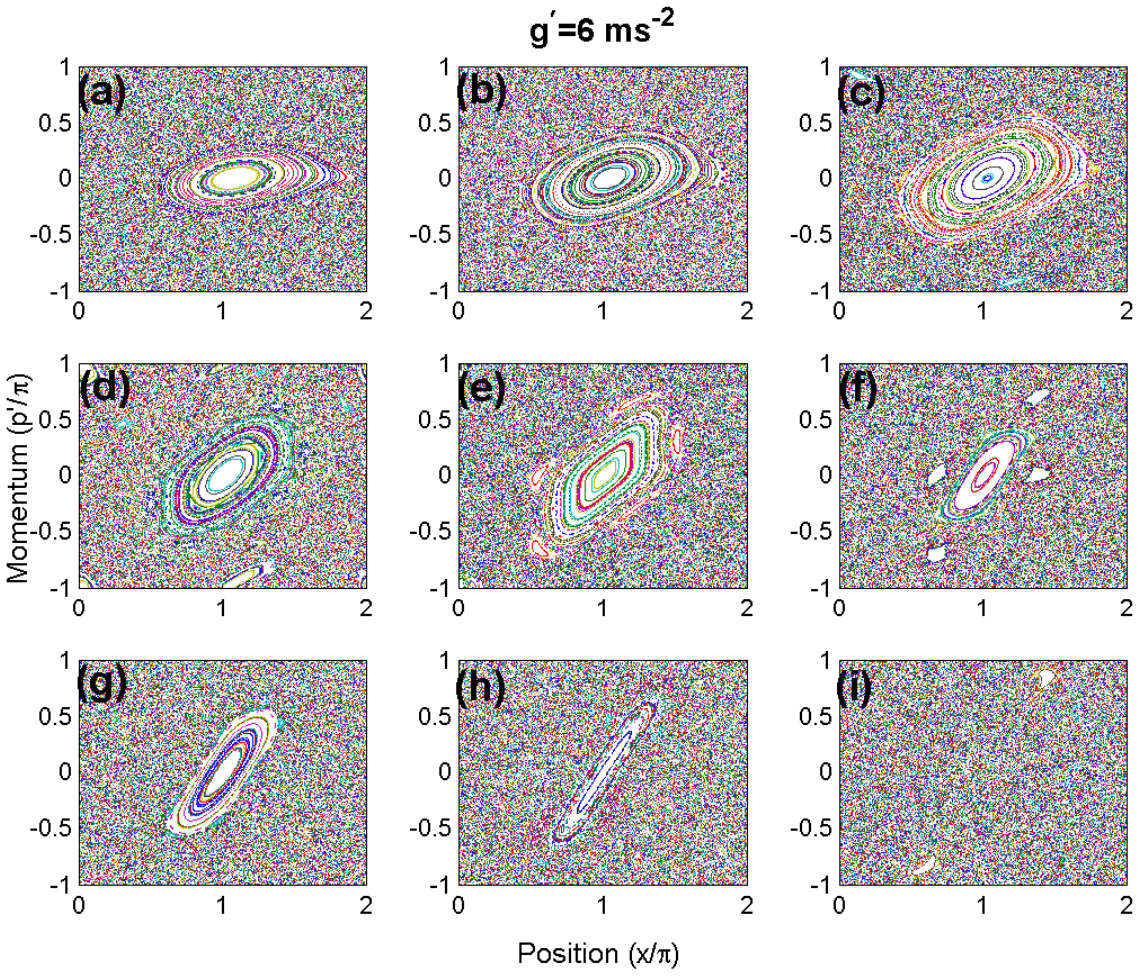

Figure 2.4: Phase space plots of the classical δ-kicked accelerator for $g' = 6$ ms^{-2} and $\tau = 2\pi$. The value of $\tilde{k}'$ used was (a) $\tilde{k}' = 0.4$, (b) $\tilde{k}' = 0.7$, (c) $\tilde{k}' = 1.0$, (d) $\tilde{k}' = 1.5$, (e) $\tilde{k}' = 2.0$, (f) $\tilde{k}' = 2.5$, (g) $\tilde{k}' = 3.0$, (h) $\tilde{k}' = 4.0$, and (i) $\tilde{k}' = 5.5$. Note that $g' = 6$ms^{-1} corresponds to the *natural* value of the acceleration used in experiments described in Chapter 5.

where $\hat{K}$ represents the kicking and the $\hat{F}$ describes the evolution under the linear potential during the time between the kicks. To find the states that enable the matrix elements of the operator $\hat{F}$ to be found, the Schrödinger equation should be solved for a linear potential.

2.4.2 Solution of Schrödinger equation for a linear potential

The Schrodinger equation of a free particle in a linear potential is given by

$$\hat{H}'_g(p)u_E(p) = Eu_E(p), \tag{2.16}$$

where the Hamiltonian in dimensionless units is $\hat{H}'_g = \hat{p}^2/2 - (\eta/\tau)\hat{x}$. Using

$$\hat{x} = i\hbar\partial/\partial p, \tag{2.17}$$

and

$$\int_{-\infty}^{\infty} u_E(p)u^*_{E'}(p)dp = \delta(E - E'), \tag{2.18}$$

Eq. (2.16) can be solved for $u_E(p)$. The solutions are given by

$$u_E(p) = \left(\frac{\tau}{2\pi\eta}\right)^{1/2} e^{i(\tau/\eta)(Ep - p^3/6)}. \tag{2.19}$$

Using these states, the matrix elements of the evolution operator during the time between pulses can be calculated.

2.4.3 Matrix elements of the evolution operator

To understand the time evolution of a given initial state under the time dependent Hamiltonian $\mathcal{H}$ of Eq. (2.5), the matrix elements of the evolution operator $\hat{U}$ need to be evaluated. The matrix elements of $\hat{U}$ can be calculated by evaluating the matrix elements of $\hat{F}$ and $\hat{K}$. The matrix elements of $\hat{F}$ are given by

$$\begin{aligned}
\langle p'|\hat{F}|p''\rangle &= \int dE \int dE' \langle p'|E\rangle\langle E|\hat{F}|E'\rangle\langle E'|p''\rangle \\
&= \int dE e^{-iE\tau} u_E(p')u^*_E(p'') \\
&= \delta(p' - p'' - \eta)e^{-i(\tau/2)(p'-\eta/2)^2} e^{-i(\tau\eta^2/24)}.
\end{aligned} \tag{2.20}$$

The matrix elements of the kick operator $\hat{K}$ are given by

$$\begin{aligned}\langle p|K|p'\rangle &= \int dx \int dx' \langle p|x\rangle\langle x|e^{-i\phi_d\cos(x)}|x'\rangle\langle x'|p'\rangle \\ &= \sum_{l=-\infty}^{\infty}(-i)^l J_l(\phi_d)\delta(p-p'-l),\end{aligned} \tag{2.21}$$

where $J_l(\phi_d)$ is the Bessel function of order l and argument ϕ_d. Thus the matrix elements of the evolution operator can be calculated:

$$\begin{aligned}(U\psi)(p) &= \langle p|U\psi\rangle \\ &= \int dp\langle p|U|p'\rangle\langle p'|\psi\rangle \\ &= \sum_{l=-\infty}^{\infty}(-i)^l J_l(\phi_d)e^{-i(\tau/2)(p-l-\eta/2)^2}\psi(p-l-\eta),\end{aligned} \tag{2.22}$$

where the constant phase is ignored.

2.4.4 States of the kicked rotor and kicked particle

For the case of $\eta = 0$, the δ-kicked accelerator corresponds to the δ-kicked rotor. A kicked particle such as the one realized in the experiments moves in straight lines, where as the kicked rotor moves in circles. The link between the two can be found by exploiting the fact that the particle moves in a periodic potential. As the standing wave imparts momentum in integer multiples of $\hbar G$, the quasi momentum β (defined as p mod 1) is conserved. Thus the momentum variable p can be written as $p = n + \beta$, where n is the integer part of the momentum and β is the fractional part of the momentum. Since the potential is spatially periodic, x can be written as x mod $2\pi = \theta$. To construct the states of the kicked particle $|\psi\rangle$, the states $|\Psi_\beta\rangle$ of the kicked rotor (particle moving in circles) with quasi angular momentum β are first constructed. In momentum representation, the β-rotor states $\langle n|\Psi_\beta\rangle$ and the kicked particle states $\langle m|\psi\rangle$ are related through

$$\langle n|\Psi_\beta\rangle = \langle n+\beta|\psi\rangle \tag{2.23}$$

In θ representation, the two are related through

$$\langle\theta|\Psi_\beta\rangle = \frac{1}{\sqrt{2\pi}}\sum_n \langle n+\beta|\psi\rangle \ \mathrm{e}^{in\theta} \tag{2.24}$$

As the particle state $|\psi\rangle$ after n_p kicks evolves into $\hat{U}^{n_p}|\psi\rangle$, the β rotor state $|\Psi_\beta\rangle$ evolves into $\hat{U}_\beta^{n_p}|\Psi_\beta\rangle$, where U_β is given by

$$\hat{U}_\beta = \exp\left(-i\phi_d\cos(\hat{\theta})\right)\exp\left(-i\frac{\tau}{2}(\hat{N}+\beta)^2\right), \tag{2.25}$$

with the angular momentum operator $\hat{N} = -i\partial/\partial\theta$ in the θ-representation.

2.4.5 Dynamics in Freely Falling Frame (FFF)

For the case of $\eta \neq 0$, the quasimomentum is not conserved since the potential is not periodic. The dynamics of the kicked particle can be simplified by going over to the FFF. The states in the FFF after n_p kicks are given by

$$\psi_{n_p}(p) = \langle p+\eta n_p|\hat{U}^{n_p}|\psi\rangle. \tag{2.26}$$

Using Eq. (2.22), the state after n_p+1 kicks, is given by

$$\psi_{n_p+1}(p) = \sum_{l=-\infty}^{\infty}(-i)^l J_l(\phi_d)e^{-\frac{\tau}{2}(p-l+\eta n_p+\eta/2)^2}\psi_{n_p}(p-l) \tag{2.27}$$

Writing Eq. (2.27) in the form $\hat{U}_f(n_p)\psi_{n_p}(p)$, the evolution operator in the FFF $\hat{U}_f(n_p)$ is given by

$$\hat{U}_f(n_p) = \exp\left(-i\phi_d\cos(\hat{x})\right)\exp\left(-i\frac{\tau}{2}(\hat{p}+n_p\eta+\eta/2)^2\right) \tag{2.28}$$

This evolution operator can be obtained from the time evolution of a Hamiltonian

$$H_f(t') = \frac{1}{2}\left(p+\frac{\eta}{\tau}t\right)^2 + \phi_d\cos(\hat{x})\sum_{n_p=-\infty}^{\infty}\delta(t-n_p\tau). \tag{2.29}$$

It may be noted that this Hamiltonian results from a gauge transformation of the Hamiltonian of the δ-kicked accelerator. Equation (2.28) is identical to that of the

kicked rotor except for the constant shift of momentum during the evolution between the kicks. Thus quasimomentum conservation is restored in the FFF, enabling the application of rotor dynamics. The matrix elements of the evolution operators $\hat{\mathcal{K}}$ (evolution during δ-kicking) and $\hat{\mathcal{R}}_\beta$ (evolution during the time between kicks) between the n_p-th kick and $n_p + 1$-th kick are

$$\langle n|\hat{\mathcal{K}}|m\rangle = (-i)^{n-m} J_{n-m}(\phi_d) \tag{2.30}$$

$$\langle n|\hat{\mathcal{R}}_\beta|m\rangle = \delta_{nm} e^{-i(\tau/2)(n+\beta+n_p\eta+\eta/2)^2} \tag{2.31}$$

and the evolution operator between n_p and $n_p + 1$ kicks is given by

$$\hat{U}_\beta(n_p) = e^{-i\phi_d \cos(\hat{\theta})} e^{-i(\tau/2)(\hat{N}+\beta+\eta n_p+\eta/2)^2}. \tag{2.32}$$

From Eq. (2.30), it can be seen that a kick "diffracts" atoms into various momentum states with the population in each state proportional to the absolute square of a Bessel function with the argument of the Bessel function nothing more than the strength of the kicking. The evolution between the kicks merely introduces a phase proportional to the kinetic energy of each momentum state.

2.5 Rephasing model

From Eq. (2.31), it can be seen that a momentum state $|m\rangle$ during the time between kicks acquires a phase Φ_m given by

$$\Phi_m = \frac{\tau}{2}(m + \beta + \eta n_p + \eta/2)^2. \tag{2.33}$$

A state $|m-1\rangle$ during the same time acquires a phase of

$$\Phi_{m-1} = \frac{\tau}{2}(m - 1 + \beta + \eta n_p + \eta/2)^2. \tag{2.34}$$

The phase difference between the two states $|m\rangle$ and $|m-1\rangle$ during the free evolution between the n_p and $n_p + 1$ kicks is given by

$$\Phi_m - \Phi_{m-1} = \tau(m + \eta n_p) + \tau(\beta + \eta/2 - 1/2). \tag{2.35}$$

In Eq. (2.35), the term $\tau(m+\eta n_p)$ changes as the number of kicks changes. The second term $\tau(\beta+\eta/2-1/2)$ is a constant for a given kicking period. Thus the two terms evolve independently. For the orders that participate in a QAM, the phase evolution between the states $|m\rangle$ and $|m-1\rangle$ should be an integer multiple of 2π so that the state $|m-1\rangle$ after n_p kicks can couple to the state $|m\rangle$ when the n_p+1 kick is applied. Thus setting the phase difference to an integer multiples of 2π independently, one obtains

$$\tau(m_{\rm QAM}+\eta n_p) = 2\pi m_{\rm QAM} L, \tag{2.36}$$

$$\tau(\beta_{\rm QAM}+\eta/2-1/2) = 2\pi L', \tag{2.37}$$

where L and L' are integers and $m_{\rm QAM}$ is the momentum order that participates in a QAM. Equation (2.37) can be solved for the momentum of a QAM, $m_{\rm QAM}$ while Eq. (2.37) allows the initial momentum at which a QAM appears, $\beta_{\rm QAM}$, to be determined. Hence,

$$m_{\rm QAM} = -\frac{\eta n_p \tau}{\tau - 2\pi L} \tag{2.38}$$

$$\beta_{\rm QAM} = \frac{2\pi L'}{\tau} - \frac{\eta}{2} + \frac{1}{2} \tag{2.39}$$

The denominator of Eq. (2.38) is called ϵ and used in the development of the ϵ-classical theory. The above rephasing theory was developed in Oxford [45] and successfully applied to predict the behavior of the QAM.

2.6 The ϵ-classical theory

The QAM acquires observable momentum in the neighborhood of a resonance period. Thus a parameter ϵ is defined as $\epsilon = \tau - 2\pi L = 2\pi(T/T_{1/2} - L)$, which represents the closeness of the kicking period to a resonance time. With this definition, Eq. (2.31) can be re written in terms of ϵ as,

$$\langle n|R_\beta|m\rangle = \delta_{nm} e^{-i\pi L n^2 - i(\epsilon/2)n^2 - in\tau(\beta+\eta n_p+\eta/2) - i\tau(\beta+\eta n_p+\eta/2)}, \tag{2.40}$$

Ignoring the constant phase factor (the last term in the exponent) and using the identity $e^{-i\pi Ln^2} = e^{-i\pi Ln}$, Eq. (2.40) becomes

$$\langle n|R_\beta|m\rangle = \delta_{nm} e^{-i\frac{\epsilon}{2}n^2 - in[\pi L + \tau(\beta+\eta n_p+\eta/2)]}. \tag{2.41}$$

The evolution operator $U_\beta(n_p)$ can thus be written as

$$\hat{U}_\beta(n_p) = e^{-i(\tilde{k}/|\epsilon|)\cos(\hat{\theta})} e^{-i/|\epsilon|\left(\frac{1}{2}\frac{\epsilon}{|\epsilon|}\hat{I}^2 + \hat{I}(\pi L + \tau\beta + \tau\eta n_p + \eta\tau/2)\right)} \tag{2.42}$$

where $\hat{I} = |\epsilon|\hat{N} = -i|\epsilon|\partial/\partial\theta$ represents the angular momentum operator and $\tilde{k} = |\epsilon|\phi_d$ represents the kicking strength.

2.6.1 Classical description of the quantum system

If $|\epsilon|$ plays the role of Planck's constant, in the limit $|\epsilon| \to 0$, an effective Hamiltonian can be obtained from Eq. (2.42) which can be used to solve Hamilton's equations of motion as described in section 2.3. The solutions thus obtained are given by a map

$$\begin{aligned} I_{n_p+1} &= I_{n_p} + \tilde{k}\sin\left(\theta_{n_p+1}\right) \\ \theta_{n_p+1} &= \theta_{n_p} + \left(\frac{\epsilon}{|\epsilon|}\right) I_{n_p} + \pi L + \tau(\beta + \eta n_p + \eta/2). \end{aligned} \tag{2.43}$$

Defining

$$J_{n_p} = I_{n_p} + (\epsilon/|\epsilon|)\left[\pi L + \tau(\beta + n_p\eta + \eta/2)\right], \tag{2.44}$$

removes the explicit time dependence of the map resulting in

$$J_{n_p+1} = J_{n_p} + \tilde{k}\sin(\theta_{n_p+1}) + \left(\frac{\epsilon}{|\epsilon|}\right)\tau\eta \tag{2.45}$$

$$\theta_{n_p+1} = \theta_{n_p} + \left(\frac{\epsilon}{|\epsilon|}\right) J_{n_p} \tag{2.46}$$

This mapping is similar to the result of Eq. (2.14) obtained by solving the classical equations of motion of a δ-kicked accelerator. The difference between the two mapping equations is that here $|\epsilon|$ plays the role of Planck's constant.

In the phase space of J and θ, if both J and θ are mod 2π, and if the trajectory cycles back after p iterations for certain initial values of J_0 and θ_0, then the map of Eq. (2.46) becomes

$$J_{\mathsf{p}} = J_0 + 2\pi\mathsf{j} \tag{2.47}$$

$$\theta_{\mathsf{p}} = \theta_0 + 2\pi l \tag{2.48}$$

where j and l are integers. Thus on average, in n_p iterations the periodic orbits of Eq. (2.47) acquire momentum J_{n_p} given by

$$J_{n_p} \simeq J_0 + 2\pi\frac{\mathsf{j}}{\mathsf{p}}n_p. \tag{2.49}$$

Using the definition of J_{n_p} from Eq. (2.44), Eq. (2.49) becomes,

$$I_{n_p} + \frac{\epsilon}{|\epsilon|}\eta\tau n_p \simeq I_0 + 2\pi\frac{\mathsf{j}}{\mathsf{p}}n_p. \tag{2.50}$$

Taking $I = |\epsilon|n$, Eq. (2.50) becomes

$$|\epsilon|\left(n_{n_p} - n_0\right) \simeq -\frac{\epsilon}{|\epsilon|}\eta\tau n_p + 2\pi\frac{\mathsf{j}}{\mathsf{p}}n_p. \tag{2.51}$$

Thus the momentum of these periodic orbits after n_p iterations is given by

$$n_{n_p} \simeq n_0 - \frac{\eta\tau n_p}{\epsilon} + 2\pi\frac{\mathsf{j}}{\mathsf{p}}\frac{n_p}{|\epsilon|}, \tag{2.52}$$

Such orbits are called the accelerator orbits since the average momentum gain is linear in pulse number. These accelerator orbits correspond to quantum accelerator modes in the dynamics of the QDKA. The parameter j is called the *jumping index* and is related to the number of units of momentum acquired per cycle, while the parameter p is the *order* of the fixed point and represents the number of kicks required before cycling back to the initial point in phase space. The mode (p, j)= $(1, 0)$ is referred to as the period 1 fixed point and shows prominently in an experiment. The island corresponding to (1,0) mode is shown in Fig. 2.5. This figure was generated for a kicking period of $T = 61$ μs which is near the Talbot time of Rb-87 atoms (Note that

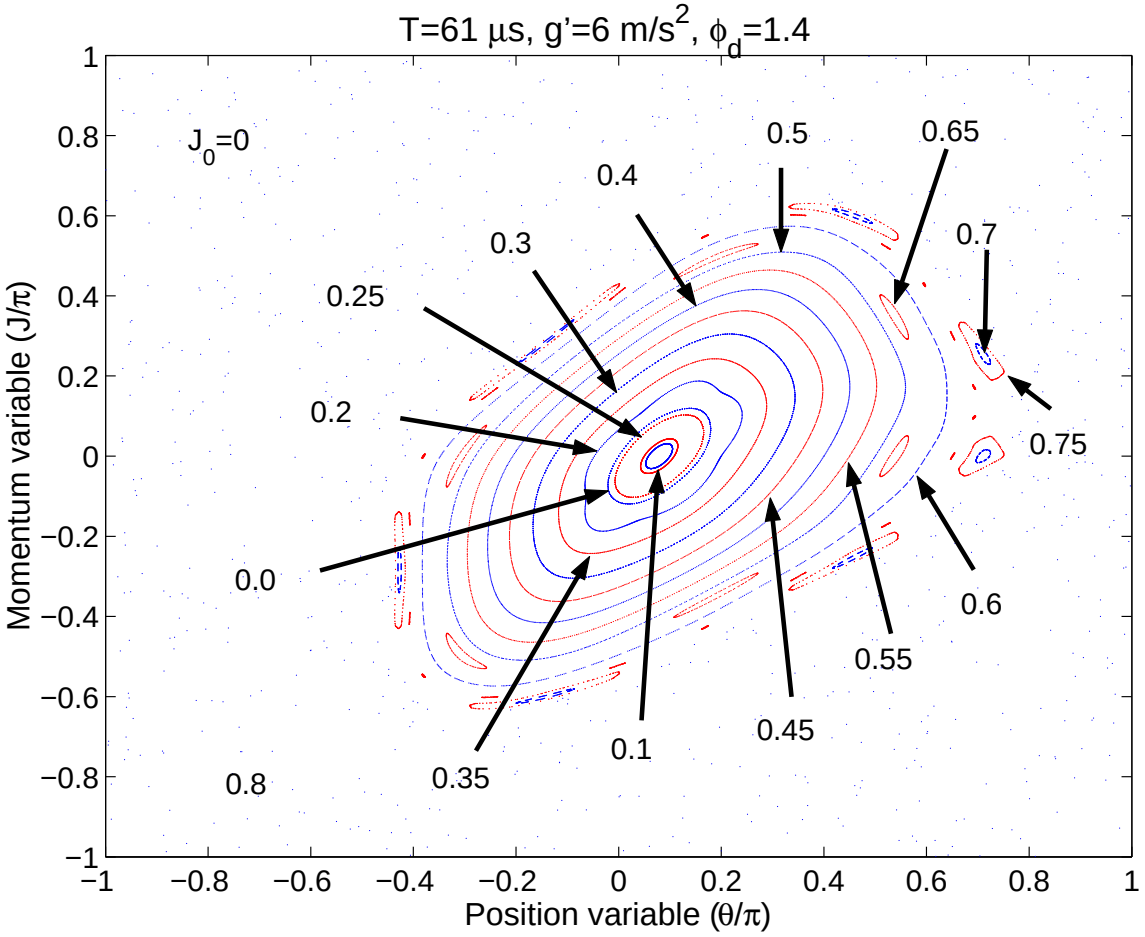

Figure 2.5: Accelerator orbits corresponding to various initial conditions constituting an island in the phase-space. The map is generated for a kicking period of 61 μs (near Talbot time which is 66.4 μs for Rb-87 atoms), $g' = 6$ ms^{-2}, $\phi_d = 1.4$, and $J_0 = 0$. The periodic orbits corresponding to the value of $\theta_0 = 0$ to 0.75π in steps of 0.05π. For $\theta_0 = 0.8\pi$, the ϵ-classical evolution becomes chaotic.

the half-Talbot time of Rb-87 is 33.2 μ s). This figure shows that for $J_0 = 0$, periodic orbits exist only for $\theta_0 < 0.75\pi$. For values of $\theta_0 \geq 0.75\pi$, the dynamics is dominated by chaos.

2.6.2 Higher order modes

The modes corresponding to $\mathsf{j} \neq 0$ are referred to as higher order modes. Observable higher order modes occur for periods close to the main resonance times and are very sensitive to the parameters used in an experiment [78, 79]. These higher order modes can be observed over a certain range of values of g', τ, η and $\tilde{k}$. To understand the dependence of the higher order modes on these values, a parameter

$$\Omega_p = \frac{\eta\tau}{2\pi} \tag{2.53}$$

can be defined. Equation (2.45) can be written in terms of Ω_p as

$$J_{n_p+1} = J_{n_p} + \tilde{k}\sin(\theta_{n_p+1}) + \left(\frac{\epsilon}{|\epsilon|}\right) 2\pi\Omega_p \tag{2.54}$$

It can be seen that for $\tilde{k} = 0$ and if Ω_p is a rational fraction j/p, then after p iterations, a given trajectory returns to its initial point in the phase space of J and θ. For non zero $\tilde{k}$, and for values of Ω_p near j/p, periodic orbits can still exist. A region in the *phase space* of $\tilde{k}$ and Ω where a stable periodic orbit of a given j and p exists is referred to as an Arnol'd tongue [80]. These tongues specify the range of parameters on g', τ, η and $\tilde{k}$ in which a given (p,j) mode can be observed. The phase space plots for $\mathsf{j} = 1$ and $\mathsf{p} = 1$ to 9 are shown in Fig. 2.6. The order p can be inferred from these plots by counting the number of islands in the momentum direction.

The higher order modes have been observed successfully by the Oxford group [81] after their existence was predicted by S. Fishman and coworkers [76, 77]. The experiment was very similar to the ones used for observing the primary accelerator modes. However, the modes were observed for pulse periods much closer to the resonance times. A large number of the higher order modes were observed for kicking periods

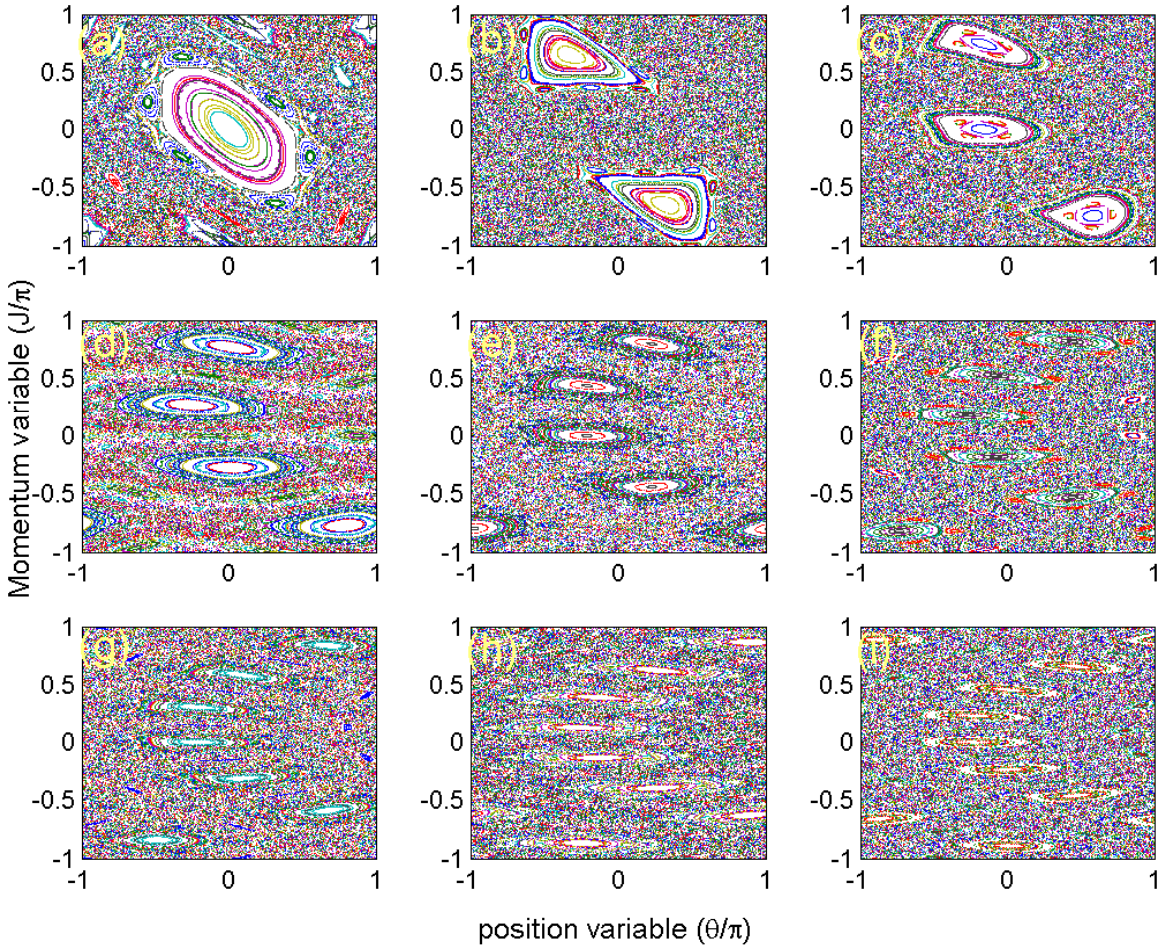

Figure 2.6: Phase space maps of higher order modes. The modes (p,j) are (a) (1,1), (b) (2,1), (c) (3,1), (d) (4,1), (e) (5,1), (f) (6,1), (g) (7,1) (h) (8,1) and (i) (9,1). The order index p is equal to the number of islands observed in the momentum direction.

near $T_{1/2}$, $2T_{1/2}$ and $3T_{1/2}$. The presence of multiple (p,j) modes for certain parameters (the overlap of the tongues) can possibly be used as a multi path beam splitter in matter wave interferometry. Other applications of the higher order modes include the study of the random walks, as proposed by K. Burnett and co-workers [82].

CHAPTER 3

Quantum Accelerator Modes using a Rb Magneto-Optic Trap

3.1 Introduction

Quantum resonances studied by Mark Raizen and coworkers [13] using the atom optics version of the kicked rotor were realized using a magneo-optic trap of sodium atoms. Quantum accelerator modes (QAMs) were first observed in a cold Cesium magneto-optic trap. After laser cooling these atomic samples can reach micro-Kelvin temperatures making them a versatile tool for atom optics experiments [88]. Magneto-optic traps (MOTs) have been a starting point for many of the most important atom optics experiments. In this chapter, the details of Rb 87 MOT set up used for the successful observation of Quantum Accelerator Modes (QAMs) is discussed. In section 3.2 the MOT and repump transitions used in Rubidium are discussed. In section 3.3, the experimental configuration is discussed. Many of the details of the set up can be found in Timmons thesis [83]. The sub Doppler cooling scheme using the Sisyphus effect is explained in section 3.4. The time of flight used for imaging the MOT and the data collection is discussed in section 3.5. In section 3.6, the realization of QAMs using a MOT is demonstrated. In section 3.7, the numerical simulations that were performed to guide and understand the experiments are detailed. In section 3.8, experiments in which two independent sets of kicking pulses were applied are discussed. Finally the conclusions of the chapter is presented in section 3.9.

3.2 Rubidium D2 transition

Rubidium can be cooled with inexpensive laser diodes. Figure 3.1 shows the D2 level structure of Rb 87. The two levels considered for the MOT transition are $F = 2$ of $5^2S_{1/2}$ ground state and $F = 3$ of $5^2P_{3/2}$ excited state. The laser used for generating the MOT light is referred to as master laser and was locked to the transition between $F = 2$ of the ground $5^2S_{1/2}$ state and the cross over line of $F = 2$ and $F = 3$ of the excited $5^2P_{3/2}$ state. Thus the master laser was detuned by 133.3 MHz to the red of the transition (see Fig. 3.1). The excited state of $F = 3$, due to power broadening, can also populate the ground $F = 1$ state. There was a second laser tuned to $F = 1$ of ground $5^2S_{1/2}$ state to $F = 2$ of the excited $5^2P_{3/2}$ state. This laser is called repump laser. The repump laser was locked to the $F = 0$ ground state and the cross over line between $F = 2$ and $F = 3$ of the excited $5^2P_{3/2}$ state. An AOM is used to tune the repump light on resonance.

3.3 Experimental configuration

The apparatus used was similar to the one used to realize the quantum δ-kicked accelerator by the Oxford group [44]. The experiment was designed such that the laser sources were isolated from the vacuum chamber. The lasers were placed on an optical table referred to as laser optical table and the experiments were performed on a separate optical table referred to as the MOT optical table. The light was transported to MOT table using optical fibers.

3.3.1 Laser optical table

The laser beams for the MOT came from a slave laser which was injection locked to a master laser. The master laser was a grating stabilized Toptica laser. This laser was a 70 mW cw laser in a temperature controlled housing. The slave laser, also placed on

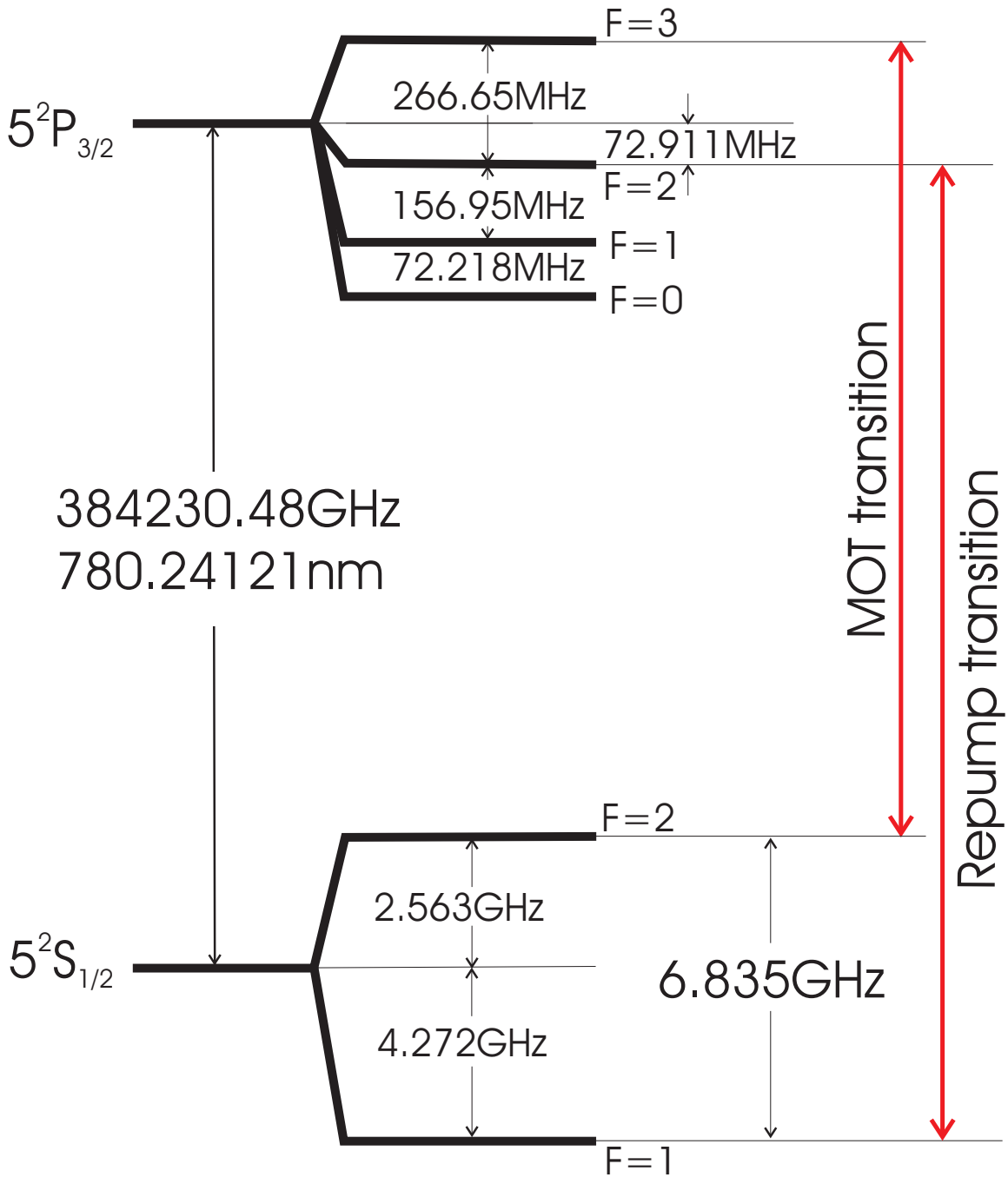

Figure 3.1: Rubidium-87 D2 level structure[84] (not to scale). The MOT and repump transitions are shown.

a temperature controlled housing, was a 120 mw cw laser. Figure 3.2 shows the path of the slave laser beam which was used for producing the MOT on lasers optical table. The collimated output beam from the laser was elliptical. An anamorphic prism pair changed the beam shape from elliptical to circular. A half-wave plate placed next to the anamorphic prism pair changed the polarization of the incident beam to 45^{O} to vertical. A polarized beam splitter cube was placed at 45^{O} after the half wave plate so that it allowed all the beam to go through it. This cube reflected away any light coming back into the laser as shown in Fig. 3.2. The Faraday rotator placed after the cube rotated the plane of polarization of the light incident from left by 45^{O} clockwise making it horizontally polarized. Any reflected horizontally polarized light incident from right on the Faraday rotator, the rotator reflected the plane of polarization counter clockwise making it 135^{O} from vertical, which would be eliminated by the polarized beam splitter cube placed at 45^{O} before the Faraday rotator. The polarized beam splitter cube placed after the Faraday rotator allowed the light from the master laser to get injected into the slave laser. About 4 mW of master light was injected into the slave. When injected, the slave laser follows the master laser. The following of the slave was monitored by taking $\sim$ 50 μW of light using a partially reflecting mirror, sending it through the Rb cell, and monitoring the beam's absorption on a photo diode. If the slave was properly following an absorption dip was observed on the scope. The slave light exiting the polarizing beam splitter cube was then made to propagate through an acousto-optic modulator (AOM) referred to as the MOT AOM. The first order of the AOM was sent into a fiber referred to as Fiber1 in Fig. 3.2. Repump light from repump laser was combined with the slave beam and sent to the same fiber. On the MOT table, 40 mW of slave light and 1 mW of repump light exited the fiber. About 700 μW of the slave light was taken into a separate fiber referred to as Fiber2 in Fig. 3.2 and used to image the atoms (see later section).

During kicking, all the light except the kicking beams was extinguished. The

MOT beams were turned off by switching off the MOT AOM. The MOT light then propagated through an AOM called the kicking AOM. This AOM was used to control the pulses of kicking light. The first order of the AOM was collected into the kicking fiber.

The master laser was detuned by 133.3 MHz to the red of the MOT transition. The light from the master laser was first injected into the first slave. The light from this slave was then double passed through an AOM which was used as a control to change the detuning of the MOT light. The first order on the second pass from the AOM was injected into the MOT laser. The path of the light from this MOT laser is shown in Fig. 3.2. The MOT AOM was driven at an acoustic frequency of 80 MHz. The negative order was sent into the fiber. Thus the required detuning of the MOT light δ_{MOT} was achieved using the equation

$$\delta_{\mathrm{MOT}} = -133.3\ \mathrm{MHz} - 80\ \mathrm{MHz} + 2f_{dp} = -213.3\ \mathrm{MHz} + 2f_{dp}, \tag{3.1}$$

where f_{dp} is the acoustic frequency with which the double pass AOM was driven [83, 85]. A MOT was achieved with a detuning of -15 MHz. This required that the double pass AOM be driven at a frequency of 99.15 MHz. For further cooling the atoms in MOT, a detuning of -70 MHz was used which corresponds to driving the double pass AOM at 71.65 MHz. During the imaging of the atoms, on resonant light was required, which was achieved by driving the double pass AOM at 106.65 MHz.

3.3.2 MOT optical table

The output of fiber1 was split into three equal beams as shown in Fig. 3.3 and then propagated through the chamber as shown in Fig. 3.4. The MOT light propagated through a polarizing beam splitter cube as shown in Fig. 3.3. This cube reflected all the repump light and allowed all the MOT light to go through it. The reflected repump beam then passed through another polarizing beam splitter cube, which reflected the repump light again. The MOT light was also allowed to propogate through the cube.

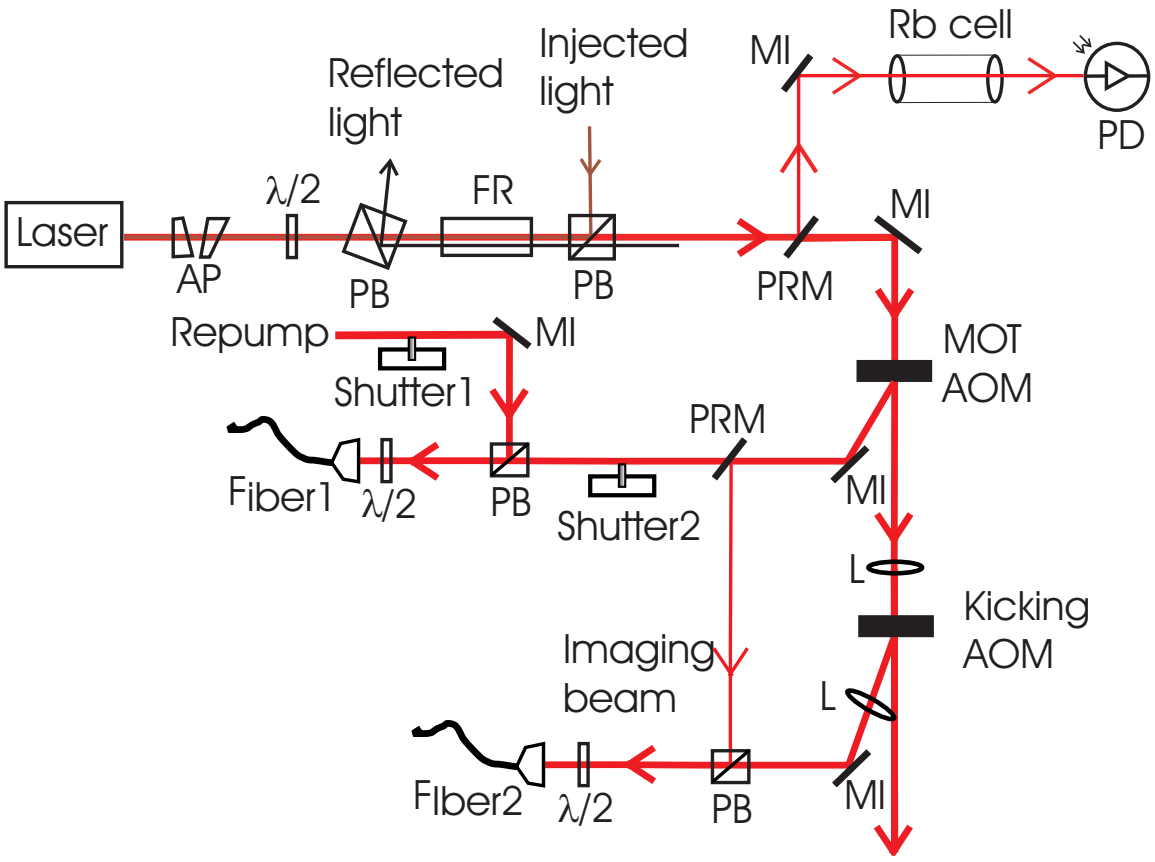

Figure 3.2: Path of MOT beams on the laser optical table. The optics shown are AP-Anamorphic prism pair, $\lambda/2$-Half wave plate, PB-Polarizing beam splitter cube, FR-Faraday rotator, PRM-Partially reflecting mirror, PD-Photo diode, MI-Mirror, AOM-Acousto-optic modulator, and L-Lens. The fibers were employed to take light from the laser optical table to MOT optical table

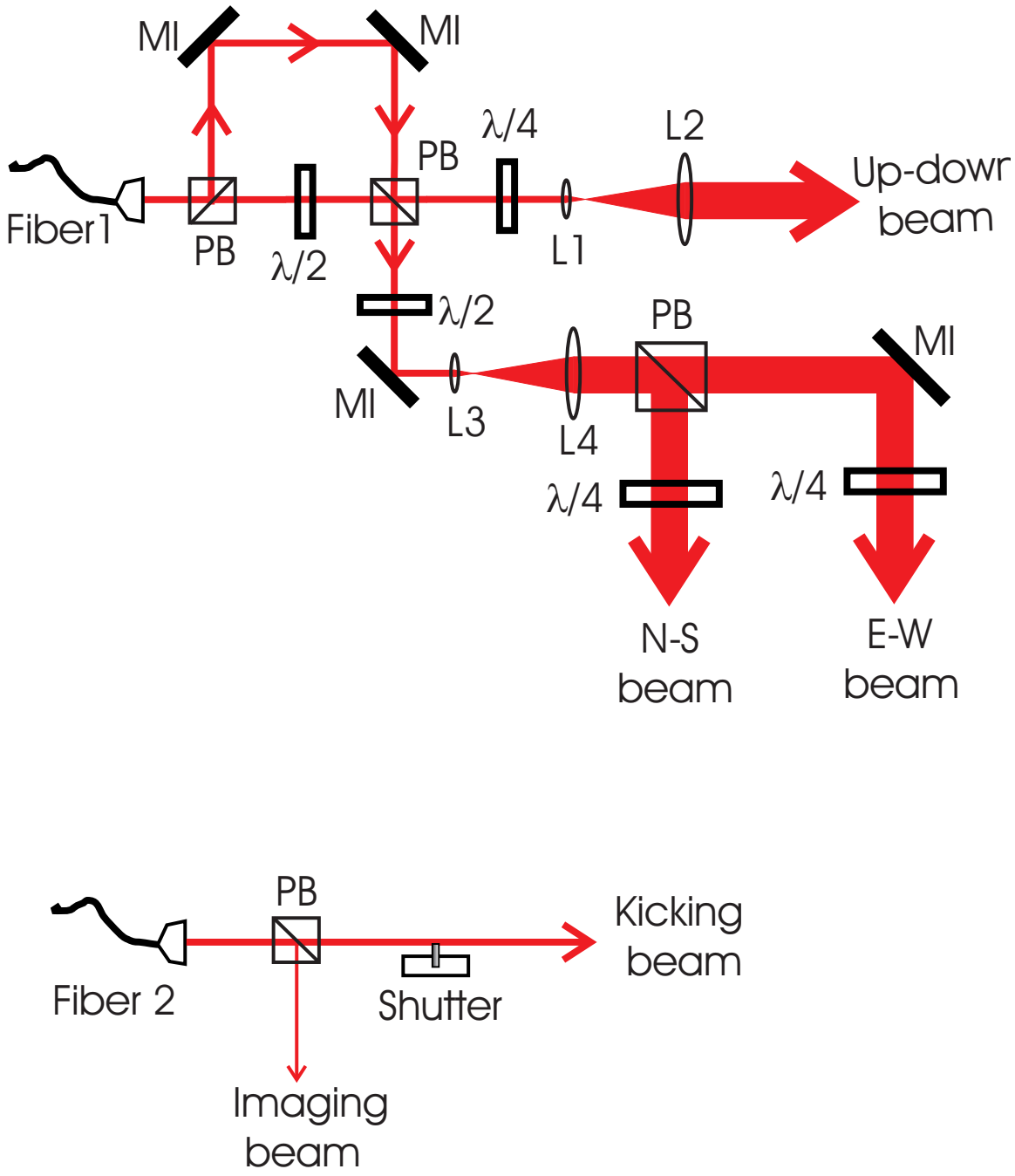

Figure 3.3: Laser beams on the MOT table. The MOT beams were first expanded to 0.5 inch and then propagated into the MOT chamber. Also shown is the output of fiber2 which are the imaging and kicking beams.

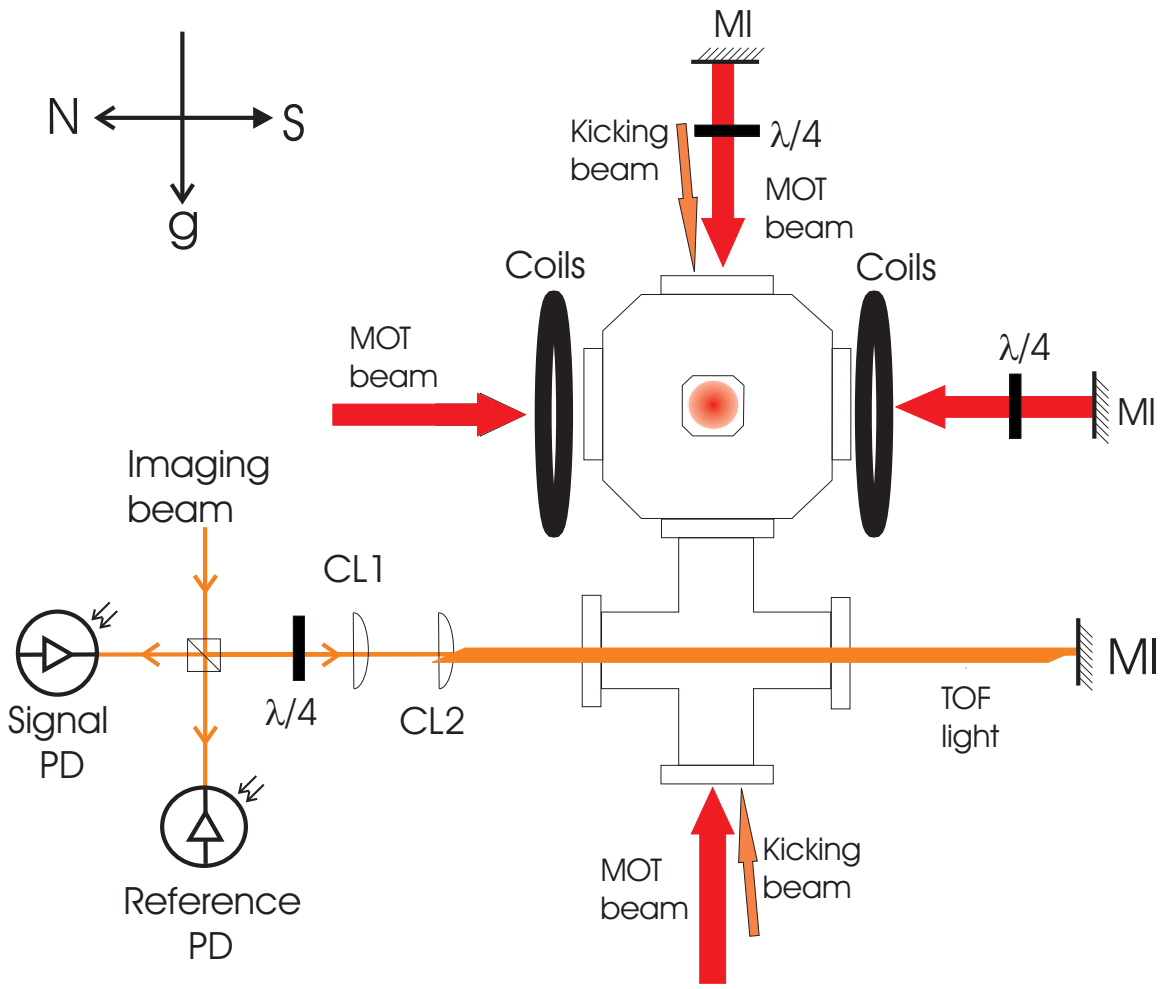

Figure 3.4: Vacuum chamber used for kicking MOT. Four MOT beams are shown. The two other beams propagate into and out of the plane of the paper. The kicking beam was slightly angled with respect to the vertical. Also shown is the path of the imaging beam.

A half-wave plate placed before this cube allowed the control on the amount of light in the reflected and transmitted paths. The half-wave plate was rotated to allow one third of the MOT light (13 mW) to go through the cube. This cube also combined the MOT and repump beams. The reflected and transmitted beams from this cube were separately propagated through two lenses to expand the beams. The reflected beam made the up-down beam in the chamber. A quarter-wave plate placed in the path of this beam circularly polarized the up-down beam. The lenses L1 and L2 placed along this beam were 3" and 20". This combination expanded a 2 mm diameter beam to 0.5" diameter. The second beam that had 2/3 of the power (27 mW) was also expanded using a combination of lenses L3 and L4 respectively are 1.2" and 6.5" to 0.5" diameter. This beam was divided equally into two beams which made the east-west and north-south beams. All three beams were aligned to go through the center of the viewports of the vacuum chamber. These beams were reflected back with opposite circular polarization. When a spatially varying magnetic field is applied using a pair of coils in anti Helmholtz configuration, a MOT was formed at the intersection of all the six beams.

The kicking and imaging beams leaving fiber 2 were separated using a polarizing beam splitter cube. Kicking beam was expanded using a combination of 6" and 8" lenses. This beam was aligned very close to vertical as shown in Fig. 3.4. Imaging beam was circularly polarized and 50 μW of the imaging beam was sent to the reference photodiode. The remaining beam was expanded into a sheet of beam which was 2 mm thick and 1/4 inch wide using a pair of cylindrical lenses. This beam was aligned 4 inches below the MOT. The imaging beam was retro-reflected back on the same path through the cylindrical lenses to the signal photodiode. The signal from the signal photodiode was subtracted from the reference photodiode to get the absorption signal of the cold atoms which appeared as a peak on the scope as shown in Fig. 3.5. The data was collected through an analog input channel of the PCI card

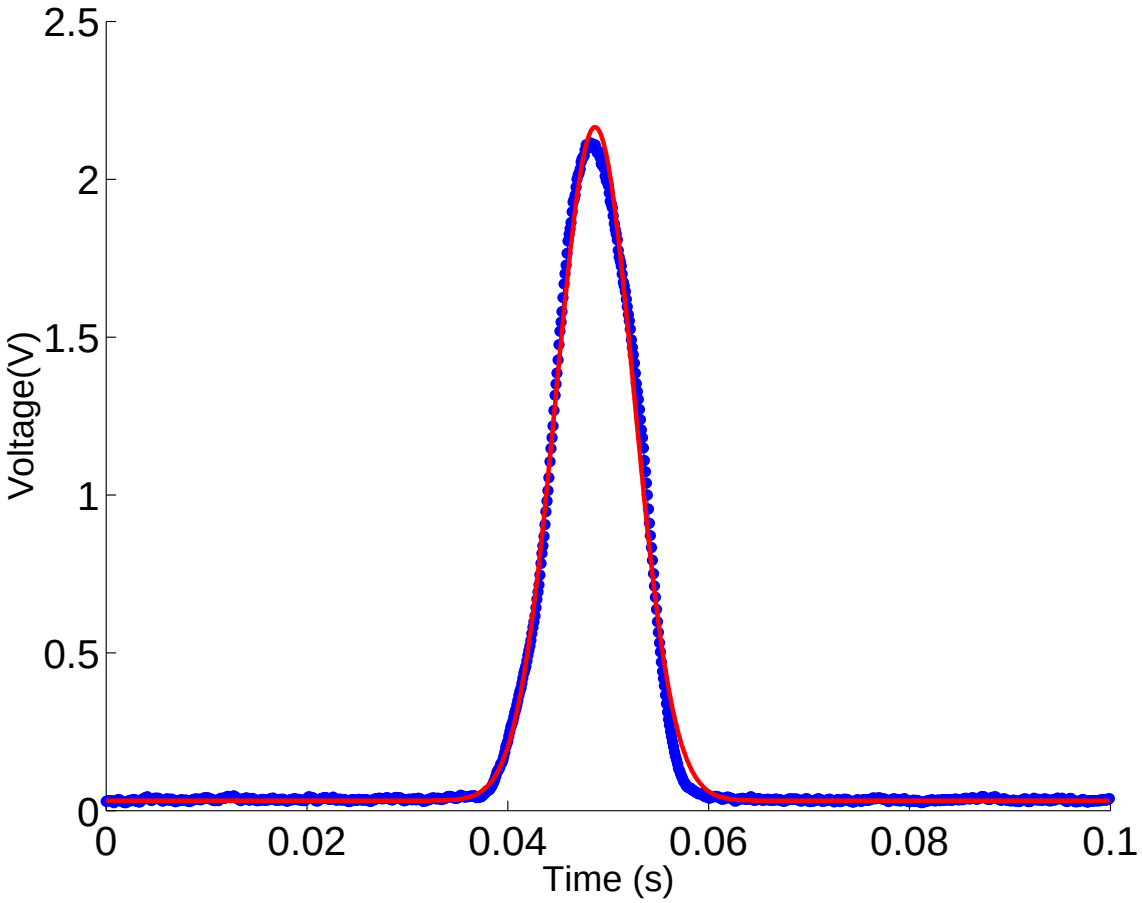

Figure 3.5: TOF signal of MOT. Blue dots are the voltage values after the voltage from reference PD was subtracted from the voltage from signal PD and amplified using a lockin amplifier. The red curve is a gaussian fit to the experimental data.

and saved to the computer.

To produce a MOT, a pair of anti-Helmholtz coils shown in Fig. 3.4 were used to create a magnetic field gradient of 10 G/cm, which provide a trapping potential. The vacuum chamber was maintained at a vacuum of 10^{-8} Torr using an 8 liter per second ion pump. This vacuum was sufficient for the kicking experiments performed to produce QAMs. Not shown in the figures are the nulling coils which were used to control the position of the MOT. With this configuration, about 10 million atoms were collected at the intersection of all the six beams in 6 seconds. It was found that the loading of MOT is optimum when the MOT beams have a detuning of -15 MHz. The temperature of the MOT is about 100 μK. This was brought down to 15 μK using Sisyphus cooling.

3.4 Sub Doppler Cooling

The sub Doppler cooling was first observed by William Phillips when the temperature of the cold atoms was measured using time of flight. Temperatures much lower than expected from Doppler limit were observed [72]. A detailed discussion of the discovery of Sisyphus cooling can be found in the Nobel lecture of W. Phillips [86]. W. Phillips and co-workers anticipated that the multiple levels that were not considered in the simple two level treatment were playing a role in cooling the atoms further [87]. The theory of this cooling was then developed by Cohen Tanoudji [73]. This is also known as the polarization gradient cooling since the origin of the cooling is the gradient in polarization.

The Doppler limit is a limit in temperature resulting from the two competing processes of Doppler cooling and recoil heating and is given by [88]

$$T_D = \frac{\hbar\Gamma}{2k_B}, \tag{3.2}$$

where T_D is called the Doppler temperature and is the lowest temperature that was

believed to be achieved in an optical molasses, Γ is the transition line width and k_B is the Boltzmann's constant. The Doppler limit for Rubidium 87 atoms is 1 mK. The subdoppler cooling can go down in principle to as low as the recoil temperature which for Rubidim 87 is 360 nK. A detailed discussion of the cooling method, is given in the theses of Timmons [83] and Ahmadi [85]. To cool the atoms well below doppler limit and for efficient imaging, the following procedure was implemented. First the MOT coils were switched off and the cooling detuning was set to -70 MHz. After waiting for 1 ms at this detuning, the MOT light was ramped down in 4 ms to about 1mW total in all the three beams and then the repump shutter was closed. The ramping down of the MOT power was achieved by misaligning the MOT light using the deflection of the first order of the MOT AOM before it entered the fiber on the laser optical table. The MOT shutter was switched on after the ramp down of the MOT beams was complete. The MOT shutter took 15 ms to totally shut off the beams. However 4 ms after reaching 1 mW of power, the MOT beams were extinguished by switching off the rf power to the MOT AOM. All the MOT light at this stage was available for kicking when the kicking experiments were to be performed. This procedure allowed the cloud to cool down to a temperature of 15 μK.

3.5 Time of Flight

After the atoms were cooled down to 15 μK temperature, the atoms were allowed to fall freely under gravity when the MOT beams were extinguished. After falling a distance of 4 inches, the atoms passed through a sheet of on-resonant light which comprised the imaging beam. Data was collected by connecting the output of a photodiode (which measured the absorption of the beam) to an analog input on the controlling computer. The temperature was estimated by fitting the data to a Gaussian and obtaining the Full Width at Half Maximum (FWHM) of the peak. The FWHM is related to the standard deviation σ_t via FWHM $= 2(\sqrt{2\ln 2})\sigma_t$ and the

temperature can be found from the equation

$$T = \frac{mg^2\sigma_t^2}{k_B}, \tag{3.3}$$

where m is the mass of the Rubidium 87 atom and $g = 9.81$ ms^{-2} is acceleration due to gravity. It was observed that the nulling coil currents played a major role in the imaging of the atoms. If the currents in the coils were not correctly set to cancel the field, the atoms would move away from the sheet of the imaging beam. The cooling depended critically on the steps of ramping down of the MOT light. By trial and error, all these parameters were optimized to get the lowest temperature possible as measured by the TOF.

3.6 Kicked MOT

The kicking experiments were performed by exposing the cooled atoms to a series of laser pulses generated by the kicking AOM. The atoms were cooled, released and allowed to fall under gravity for around 2 ms before they were kicked. Before kicking, the atoms were transferred to the $F = 1$ level of the $5^2S_{1/2}$ state by switching off the repump light before switching off the MOT beams. Atoms in the $F = 1$ level see the MOT light with a detuning of -6.8 GHz (see Fig. 3.1). This detuning corresponds to the separation of the two hyper fine levels of the ground state $5^2S_{1/2}$. This avoided the need for additional laser such as a Ti-sapphire or Nd-YAG. The original proposal of using a Nd-YAG laser was ruled out since the coherence length is very short (~ 1 inch). To pulse the kicking light, the kicking AOM was driven using a HP8770A arbitrary waveform synthesizer. The output of the synthesizer was amplified and fed to the kicking AOM. Once the kicking was complete, the MOT AOM was switched back on to derive the imaging beam. The HP8770A function generator was programmed to control the pulse period, kick pulse duration, number of kicks, and the wait-time before kicking. The kicking beam was expanded to a diameter of 1.25 mm and

contained 40 mW of power. The size of the MOT was 1 mm. With these parameters, a phase modulation depth ϕ_d in Eq. 7.5 of π was achieved. This was sufficient to produce efficient quantum accelerator modes. The momentum distribution of the kicked atoms was measured by allowing atoms to fall freely for $T_{TOF} = 140$ ms before falling through the resonant beam. The momentum of the atoms with respect to the center of the cloud is given by

$$p = \frac{mg\Delta t}{2}\left(\frac{2T_{TOF} + g\Delta t}{T_{TOF} + \Delta t}\right), \tag{3.4}$$

where Δt is the difference in time for atoms imaged at $T_{TOF} + \Delta t$ and the atoms imaged at T_{TOF}. The center of the cloud was chosen to have zero momentum.

Quantum Accelerator Modes (QAMs) can be observed for kicking periods close to a resonance period. Thus a preliminary step to observe the QAMs is to perform a scan of kicking period across a resonance in order to identify it. Figure 3.6 shows the experimental results and the theoretical fit to Eq. (2.52) for a scan across the half Talbot time 33.2 μs. Figure 3.6 was generated by stacking TOF images after 60 kicks for the kicking period given on the x-axis. The numerical simulation was done based on the diffraction picture and is shown in Fig. 3.7. As evidenced from the figures, a very good agreement is found between the theory and the experiments. Scans of the kicking period for the identical conditions at the half-Talbot time for circularly polarized and elliptically polarized kicking beams are displayed in Fig. 3.8. For Cs-133 atoms used by Oxford group, the QAMs appear only for the linearly polarized kicking light [45]. The fact that the quantum accelerator modes are observed for polarizations other than linear polarization makes Rb 87 a versatile system for producing quantum accelerator modes.

The theory predicts that a scan of kick number produces a linear increase in momentum for a QAM. This is displayed in Fig. 3.9. This data was generated for a kicking period of $T = 29.5$ μs. The fit shows that there is a very good agreement between the theory of Eq. (2.52) and experiments.

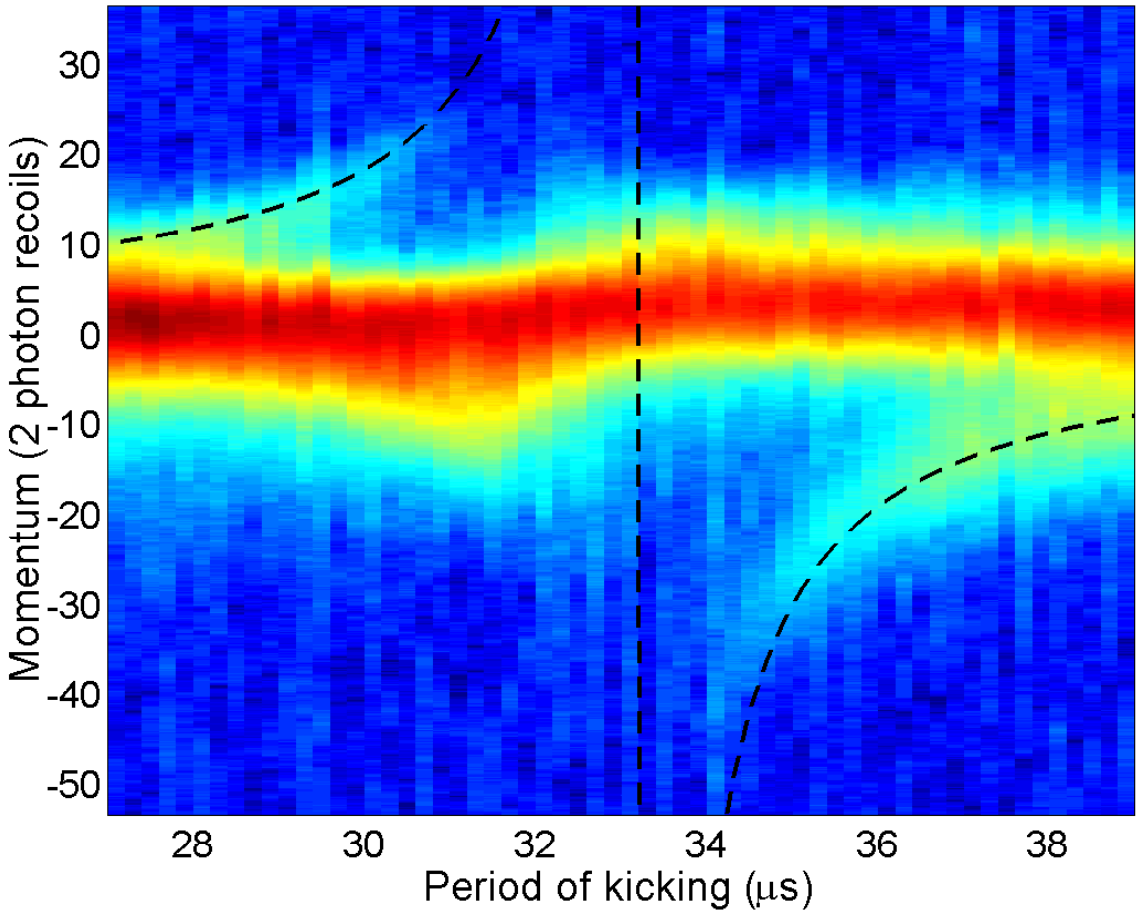

Figure 3.6: Final momentum distribution for the scan of kicking period across the half-Talbot time (33.2 μs) after 60 kicks. The curve is the fit to Eq. (2.52) which is a result of both the rephasing model and the ϵ-classical model.

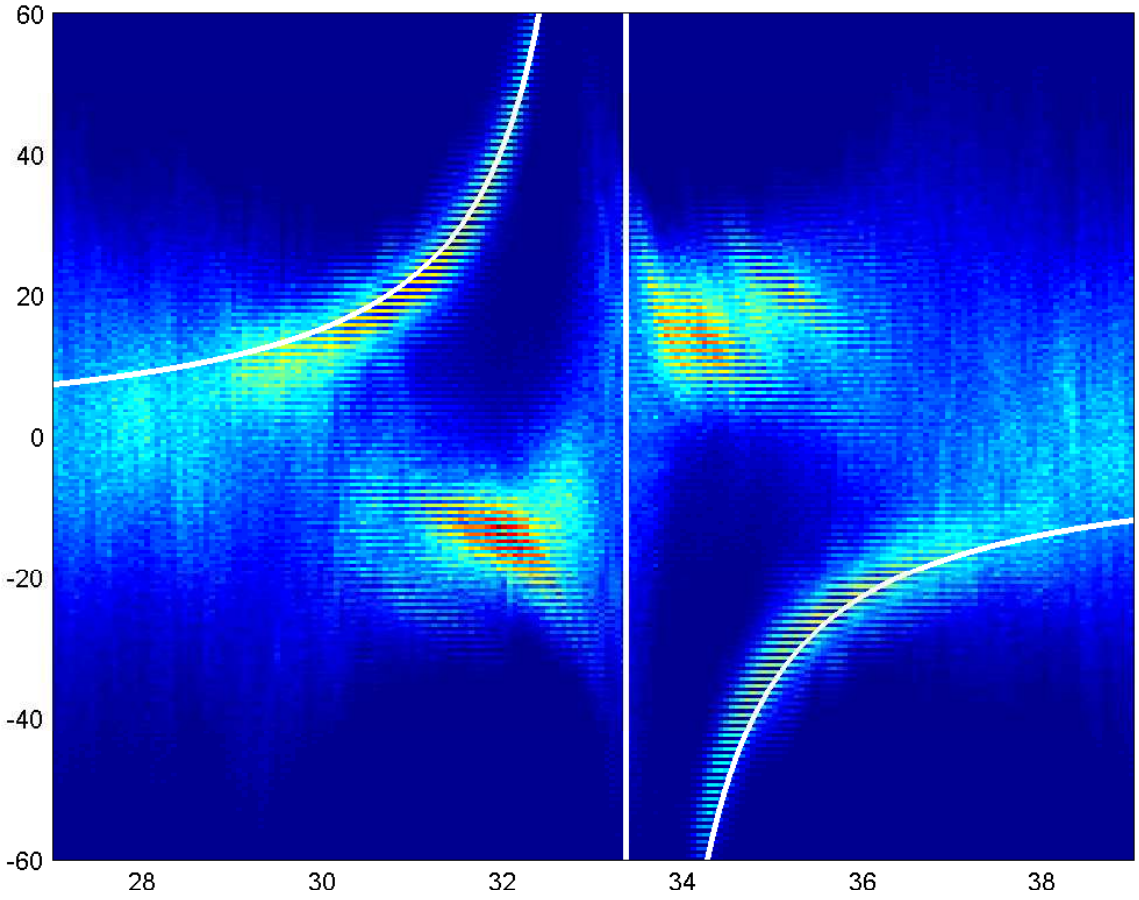

Figure 3.7: Numerical simulations for a scan across half-Talbot time (33.2 μs) for the same parameters used to generate Fig. 3.6 and the solid line shows the fit to Eq. (2.52).

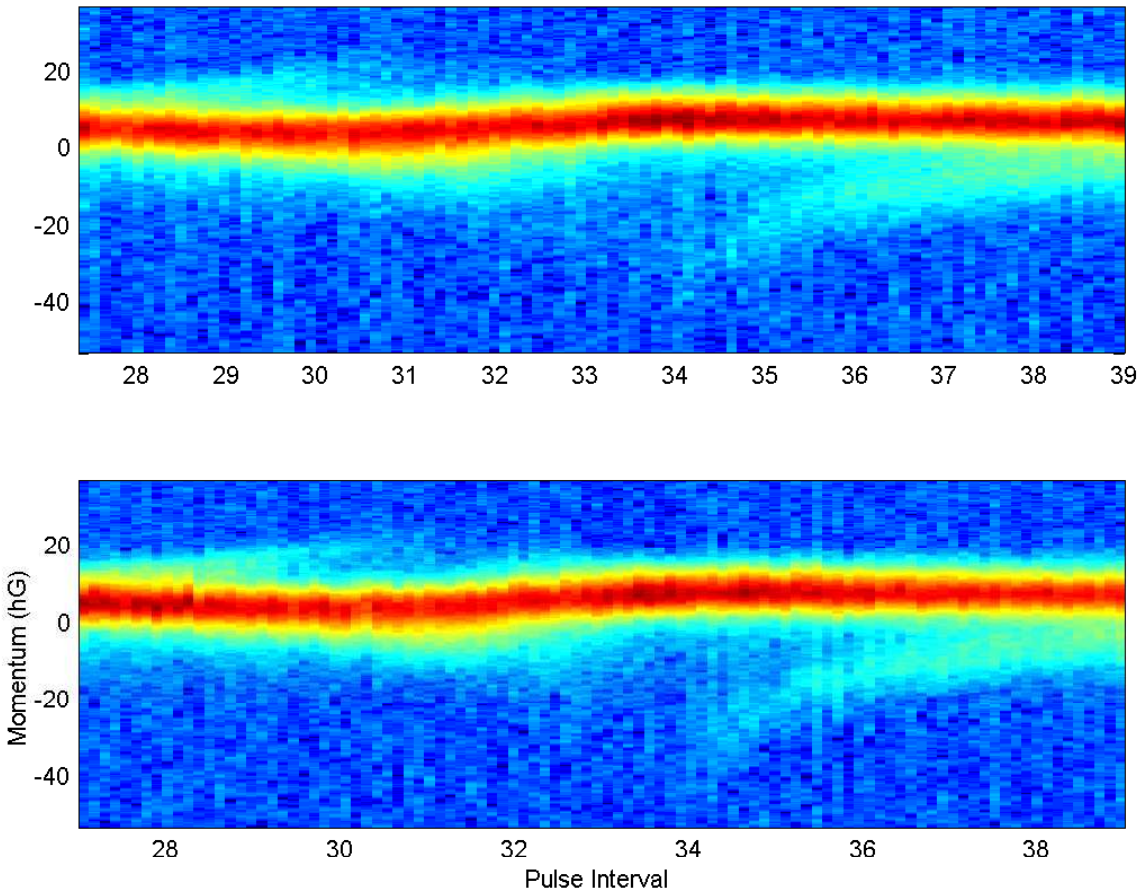

Figure 3.8: Experimental momentum distribution for the scan across the half Talbot time (33.2 μs) after 60 kicks for (a) circularly polarized kicking light and (b) elliptically polarized kicking light. The fact that the QAM can be observed in both cases makes Rb 87 a versatile system

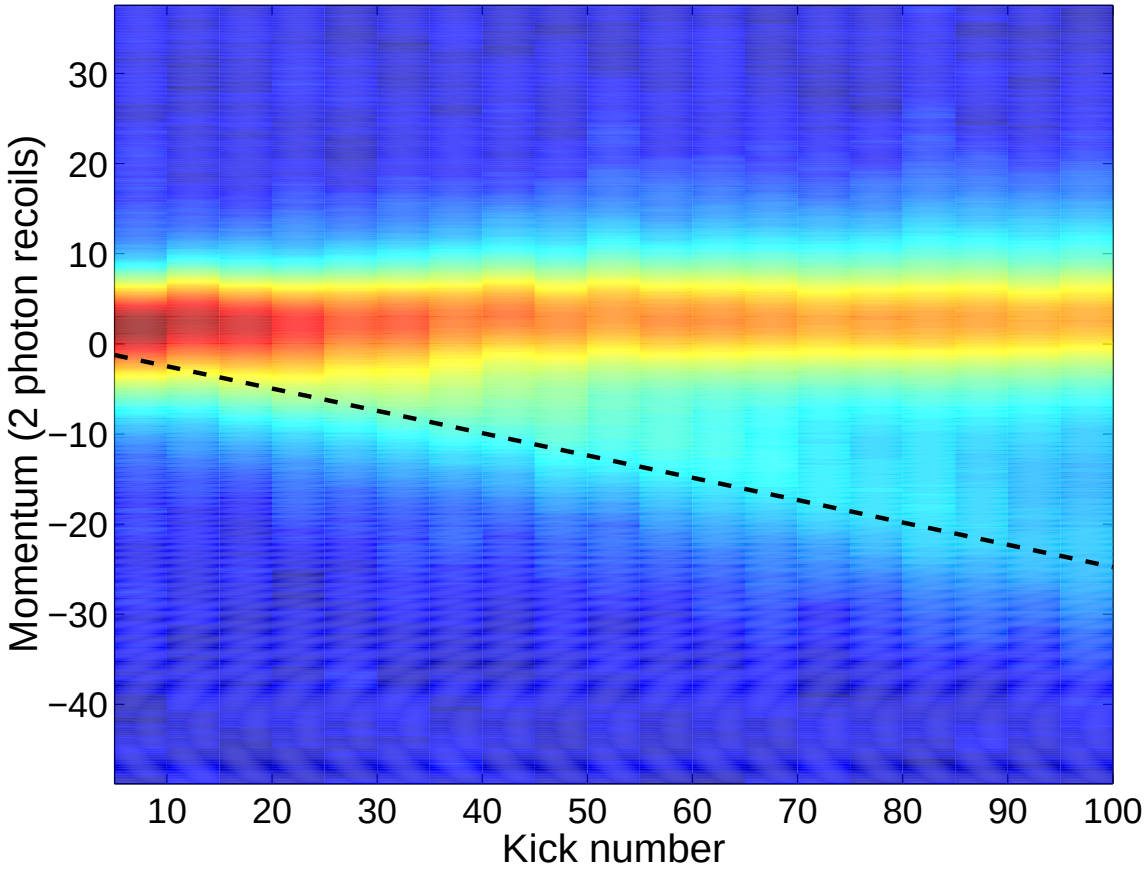

Figure 3.9: Final momentum distribution for a scan of kick number near the half-Talbot time $T = 37.2$ μs. The dotted line shows the fit to QAM of Eq. (2.52).

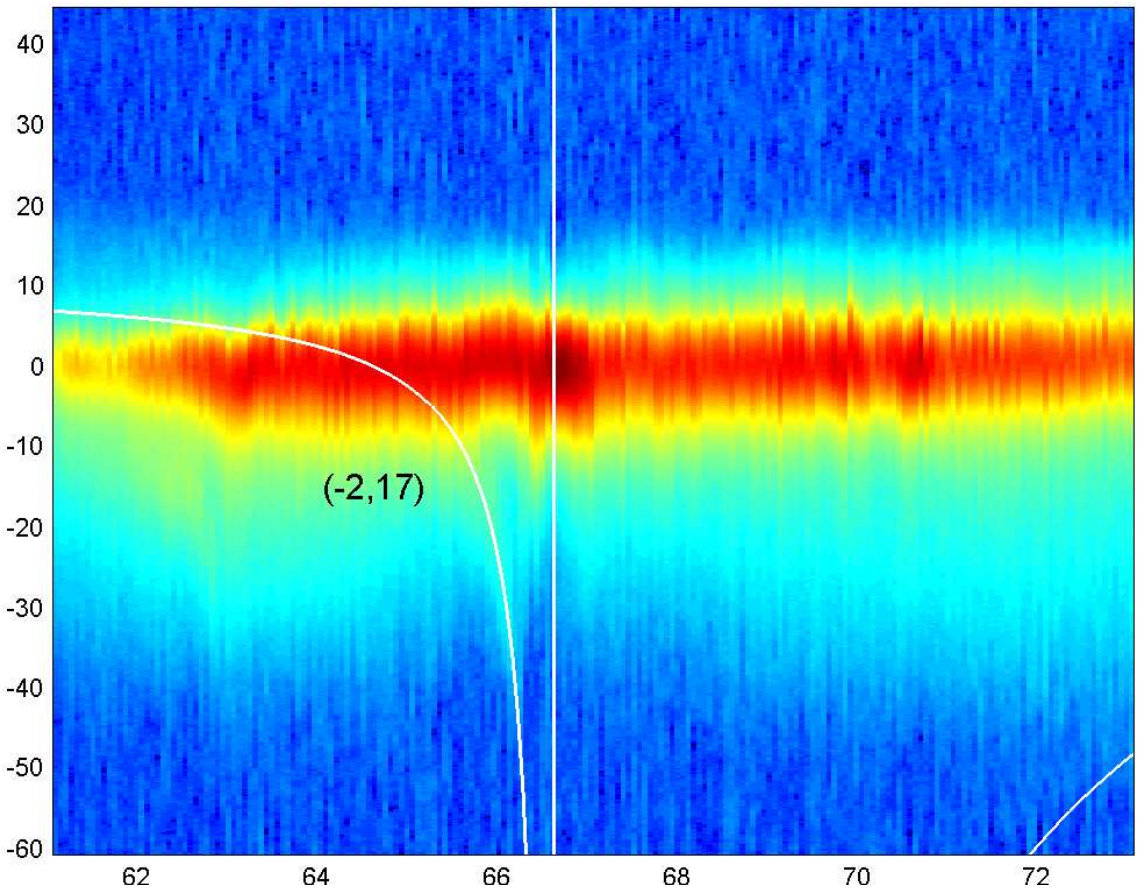

Figure 3.10: Momentum distribution for a scan at the Talbot time (66.6 μs) for 100 pulses with theoretical curves identified the higher order mode with $\mathsf{j} = -2$ and $\mathsf{p} = 17$. An unknown high order resonance emerges at 63 μs. These high order resonances were eventually observed and are detailed in Chapter 6 of the thesis.

According to the FGR theory, a scan across the Talbot time produces higher order accelerator modes as shown in Fig. 3.10. From Fig. 3.10, a higher order mode with $\mathsf{p} = 17$ and $\mathsf{j} = -2$ was observed in our experiment by fitting Eq. (2.52) to the observable mode in the experimental data. Also in Fig. 3.10 there is an un identified QAM around a high order resonance between 62 μs and 64 μs. This motivated the study of the high order resonances which is the subject matter of Chapter 6.

3.7 Numerical simulation results

To understand the experiments better, numerical simulations were performed. The code for the simulations was developed in Oxford [89] and is based on Eq. (2.32). The code was subsequently modified to apply to the experiments presented here. The kick and free evolution matrices of Eq. (2.32) were first constructed, then for a given initial state and parameters, the matrices were stacked in appropriate order with a column matrix of initial state at the right most of the sequence. Each of these orders in the initial state were convoluted with a Gaussian momentum distribution of certain width to mimic the experimental situation. The product of these matrices gives the final state from which the momentum distribution can be obtained. The results of the numerical simulations performed for the parameters used in obtaining Fig. 3.6 is displayed in Fig. 3.7. The theory curve of Eq. (2.52) is plotted on the same figure. The strength of the numerical simulations can be seen in Figs. 3.11, 3.12. Figure 3.11 shows a scan of kicking period across the first three primary resonances $T_{1/2}$, $2T_{1/2}$ and $3T_{1/2}$. Besides showing the primary resonances, these numerical simulations also display the clear indication of the presence of the higher order resonances such as $(3/2)T_{1/2}$, $(7/4)T_{1/2}$ and $(5/2)T_{1/2}$ which are clearly evident in the the mean momentum plot of Fig. (3.12). These simulations later guided the experiments to the observation of some of these modes which are detailed in chapter 6.

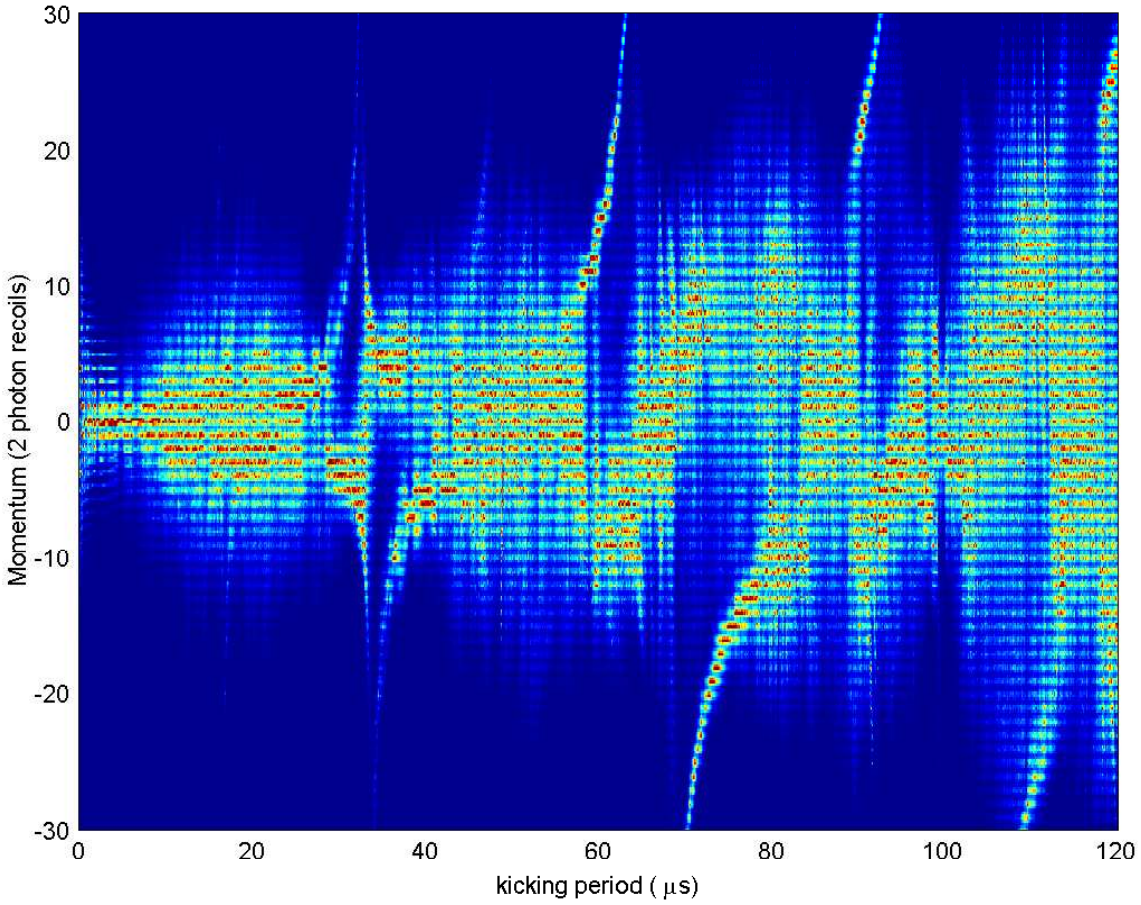

Figure 3.11: Numerical simulation of a scan of time between pulses after 30 pulses. The numerical simulations have been used to guide the experiments. Note the presence of the primary resonances at $\sim$ 33, 66, 99 μs. Also visible are high order resonances such as the one at 17 μs.

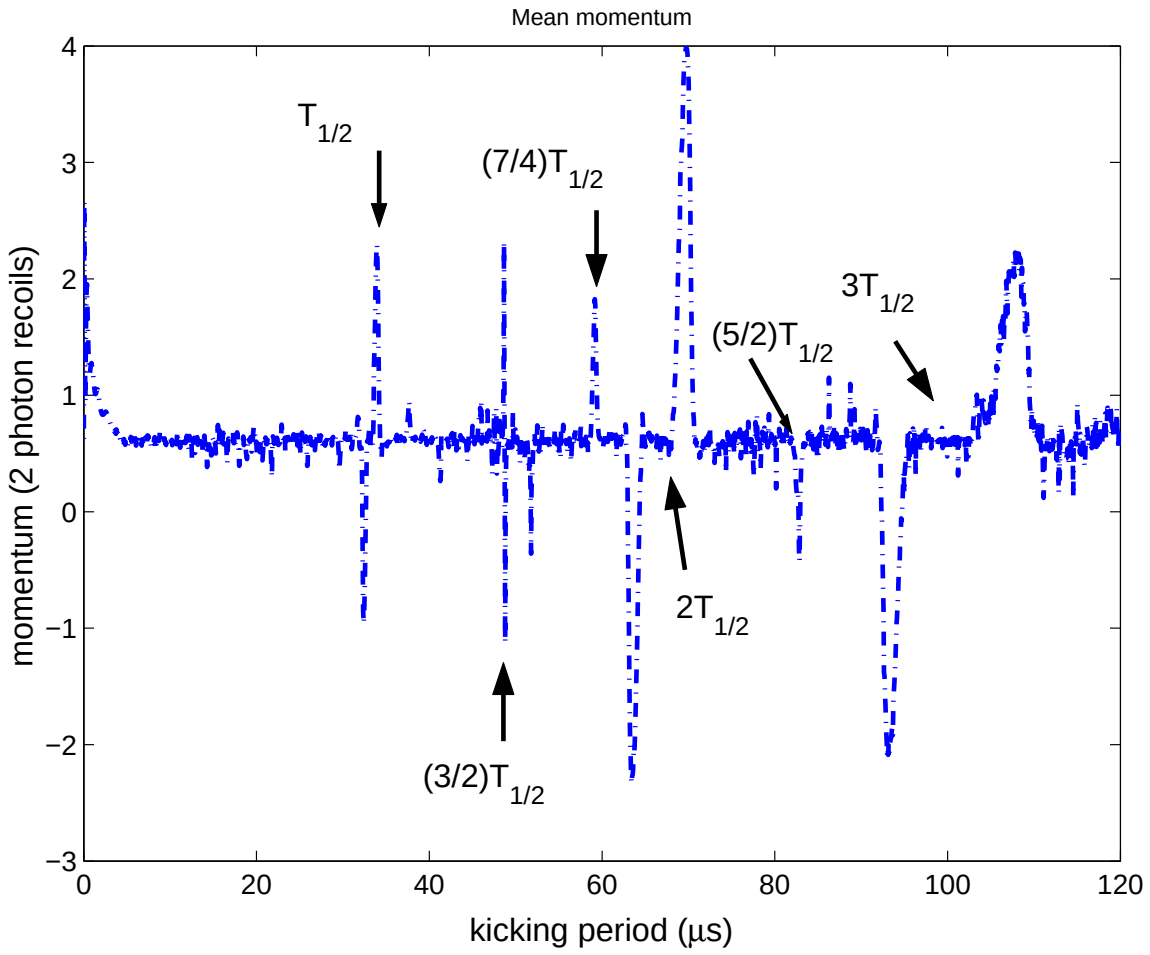

Figure 3.12: Mean momentum for a numerical simulation data as a function of kicking period. The high order resonance $(3/2)T_{1/2}$ and several others can be clearly seen.

3.8 Double kicking

To understand the behavior of the QAM (and motivated by the double-kicked rotor [90, 91], and the kicked accelerator [48] experiments to study the dependence of a QAM on the initial conditions), a series of experiments were performed where a QAM was first produced and then the atoms were kicked with second set of pulses with a different kicking period. The experimental results are displayed in Figs. 3.13 and 3.14. A series of unidentified modes have been populated which need to be accounted for theoretically. The numerical simulations have been used to confirm the experimental findings and are displayed in Figs. 3.15 and 3.16. For Fig. 3.13, a set of 30 kicks were produced at 27 μs to populate a QAM with momentum 6 $\hbar G$ and then a second set of 30 kicks were used to kick the kicked and leftover atoms. A scan of the kicking period of second set of kicks from 27 μs to 39 μs (which spans the range of QAM at half Talbot time) was performed. For fig. 3.14, the first set of kicks was at 35 μs which populated a QAM with momentum -17 $\hbar G$. A second set of kicks was produced similar to the experiment that was used to generate Fig. 3.14. The numerical simulation results of Figs. 3.15 and 3.16 were generated for the same parameters as in Figs. 3.13 and 3.14 respectively

3.9 Conclusions

Thus an experimental design to produce the QAMs was successfully constructed using a MOT as a source of atoms. The behavior of the QAMs as a function of kicking period, number of kicks and polarization of the kicking light was studied. The numerical simulations were used to understand the experimental data. With this understanding, the BEC was kicked to produce the QAM which is discussed in chapter 5.

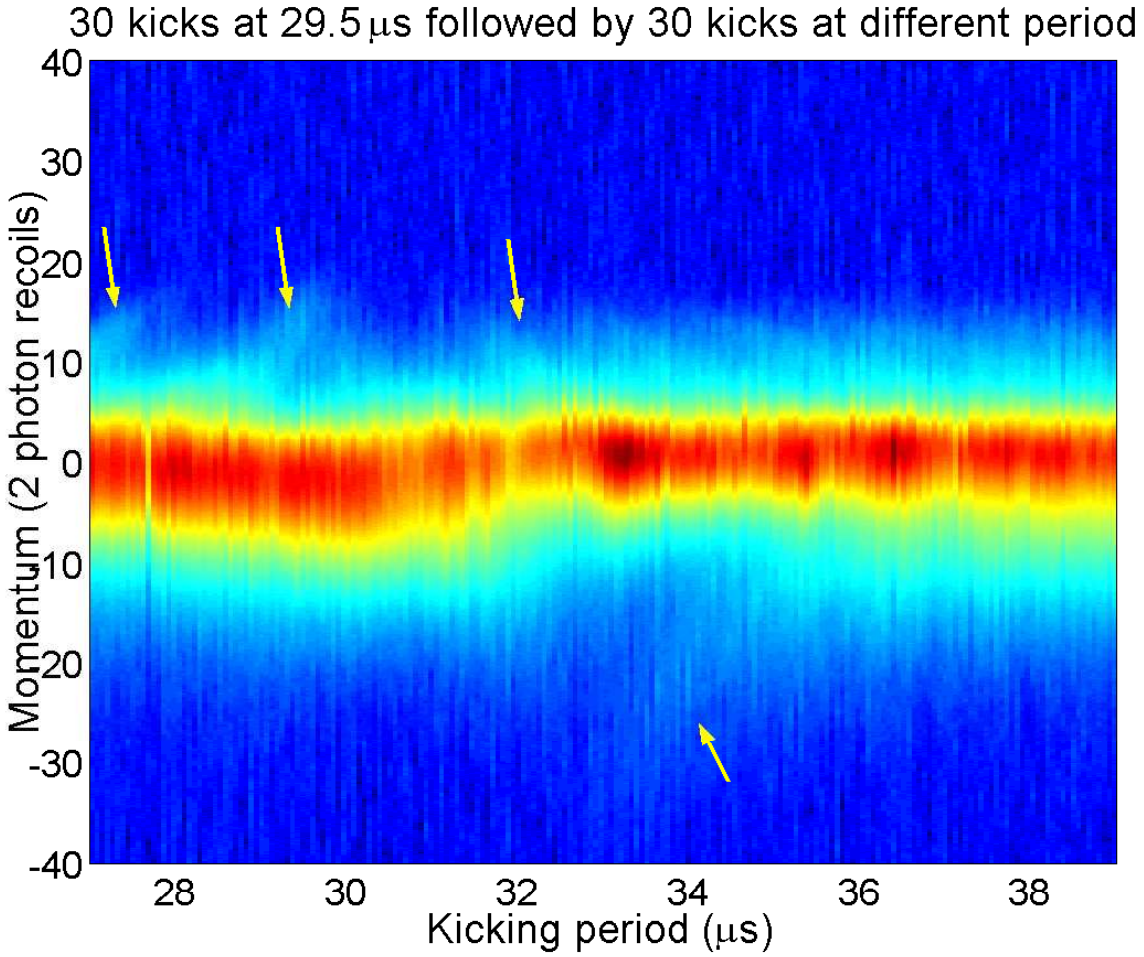

Figure 3.13: Two sets of kicks for MOT: A set of 30 kicks at $T = 29.5$ μs populate a QAM and a second set of 30 kicks at $T = 27$ μs to 39 μs produce various QAMs (identified by arrows).

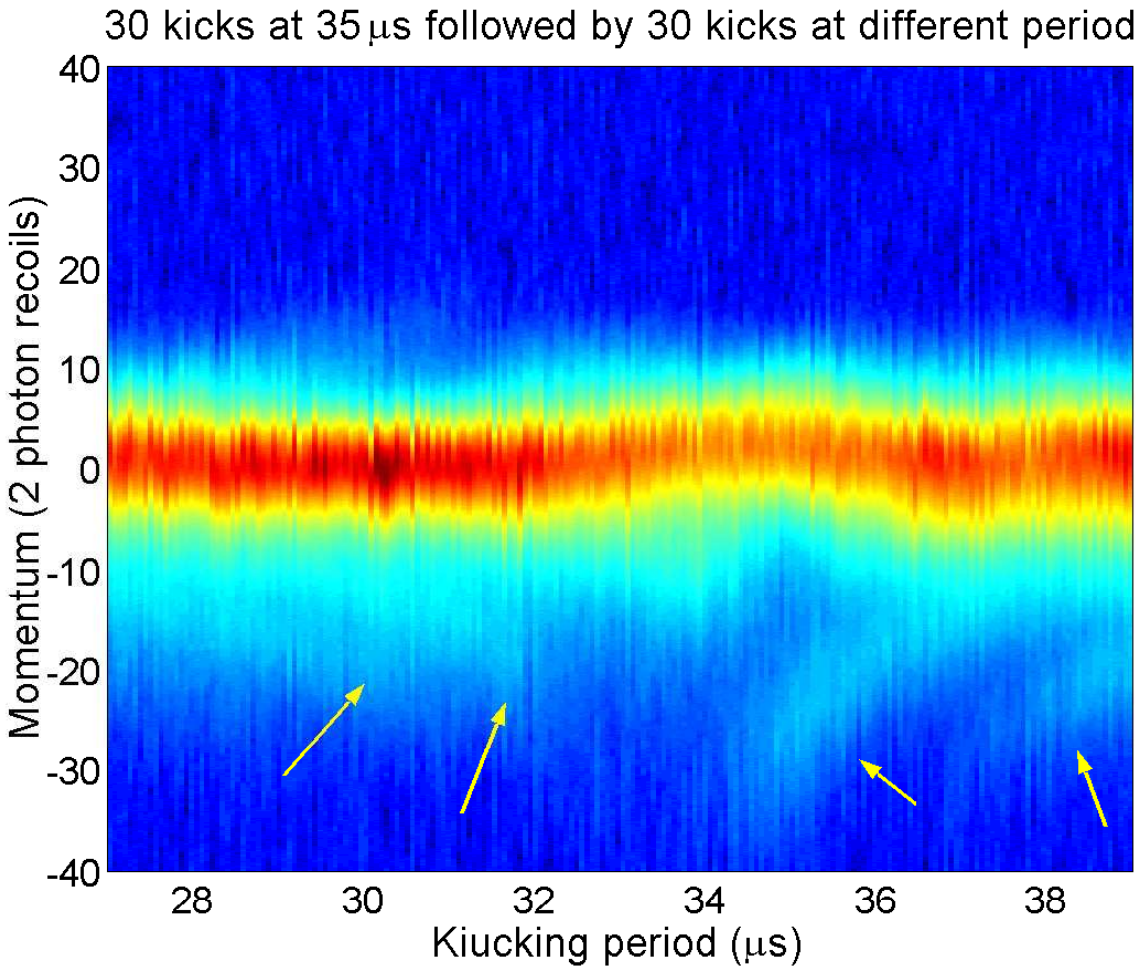

Figure 3.14: Two sets of kcks: A set of 30 kicks at $T = 35$ μs and a second set of 30 kicks at $T = 27$ μs to 39 μs. Arrows identify the QAM formed by the second set of kicks

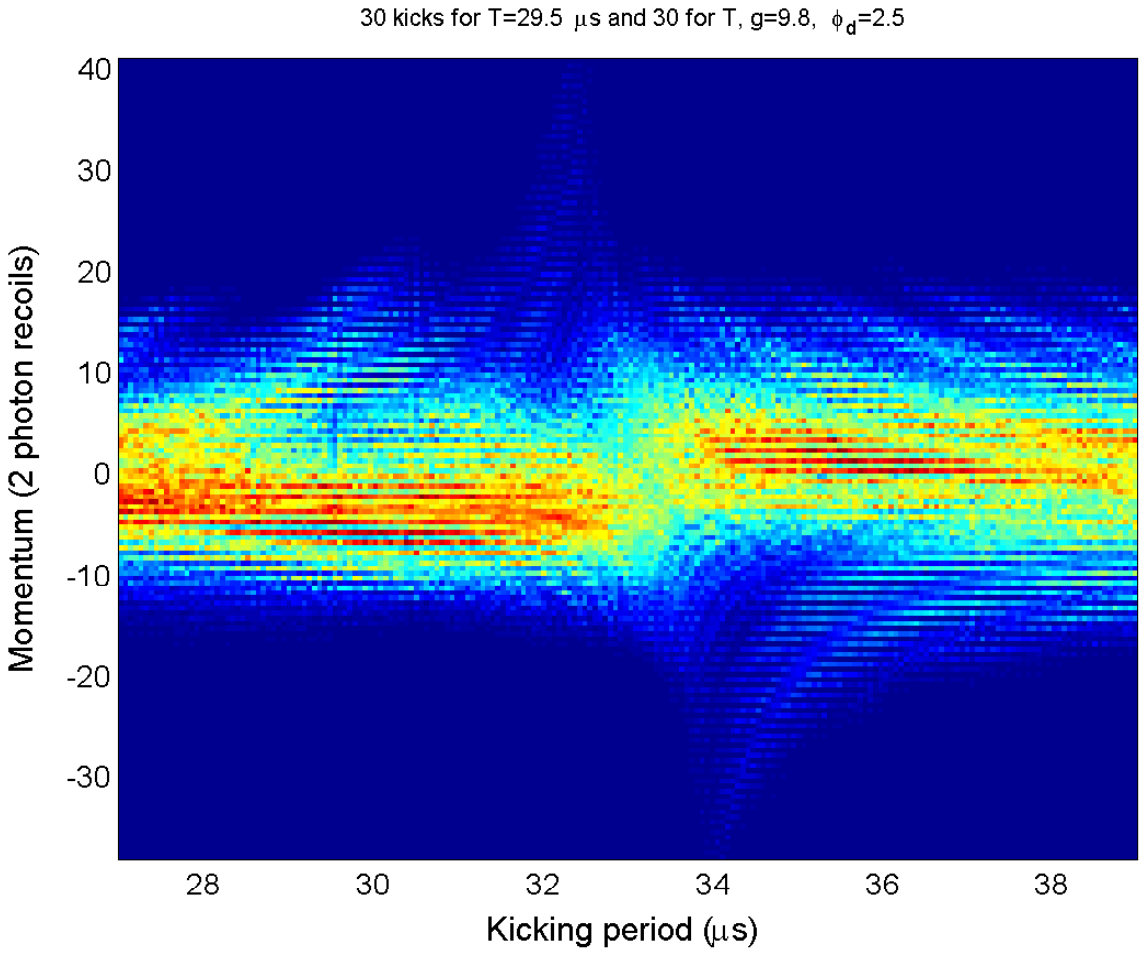

Figure 3.15: Numerical simulations of first set of 30 kicks at $T = 29.5$ μs and a second set of 30 kicks at $T = 27$ μs to 39 μs (same parameters as in Fig. 3.13)

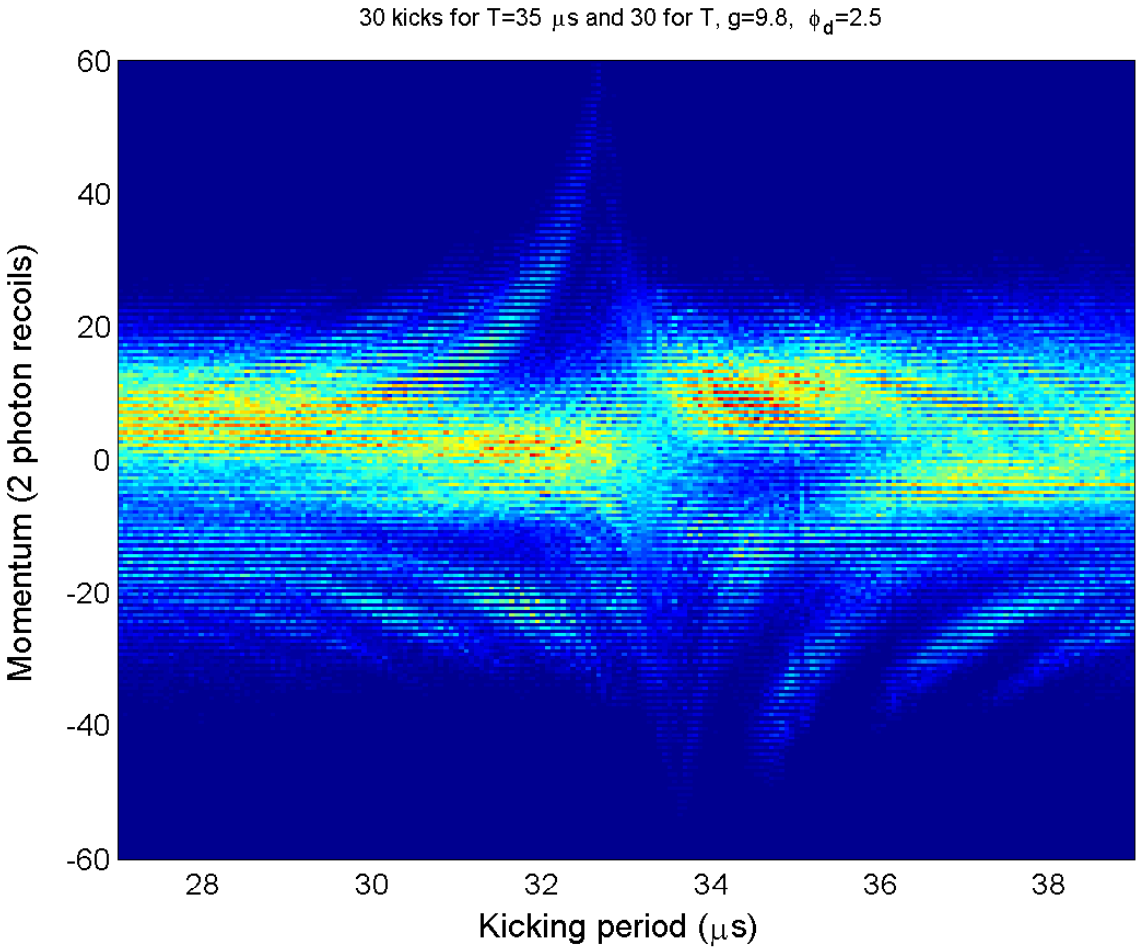

Figure 3.16: Numerical simulation results for a set of 30 kicks at $T = 35$ μs followed by a second set of 30 kicks at $T = 27$ μs to 39 μs (same parameters as in Fig. 3.14)

CHAPTER 4

Bose-Einstein Condensation

4.1 Introduction

Bose-Einstein Condensation (BEC) was first predicted by Albert Einstein in 1925 [55, 56, 57] followed by the findings of Satyendra Nath Bose [54]. However it was not until 1995 that the BEC was realized using magnetic trapping by Eric Cornell, Carl Wiemann [60] and later by Wolfgang Ketterle [61]. In this chapter a technique of utilizing the aberration to successfully produce the multiple microtraps is reported. The successful realization of the all optical BEC using a single focused high power laser is also reported.

All optical trapping was pioneered by M. Chapman at Georgia Institute of Technology. Chapman *et al.* [92, 93] used a QUasi Electro Static Trap (QUEST) to observe the BEC using an all optical technique. A similar method of using a lens placed on a motorized translational stage to achieve all optical BEC was reported by a group led by David S. Weiss at Pennsylvania State University [94]. This chapter details the all-optical method of trapping and the realization of BEC using a single high power focused laser beam. One of the possible consequences of producing tightly focused beams is spherical aberration which is also discussed. Such aberrations can be used to produce multiple micro optical traps. Other details can be found in the paper in the *New Journal of Physics* [95].

When far-off resonant light is incident on atoms, the electric field of the electromagnetic radiation induces a dipole moment which then interacts with the electric field of the radiation. The interaction potential of atoms with such an external elec-

tromagnetic field of which is given by

$$U = -\frac{1}{2}\alpha_g E_z^2, \tag{4.1}$$

where α_g is the ground state polarizability. The electric field E_z is assumed to be in the z direction. Since the interaction is effectively electrostatic, the trap is known as QUasi Electro Static Trap (QUEST). These traps are also referred as Far-Off-Resonant Traps (FORTs). These FORTs (or QUESTS) have been employed in the realization of all optical BEC [92]. Consider now a focused Gaussian beam, the electric field is given by,

$$E_z(\mathbf{r}) = E_0 \frac{\exp\left[-r^2/w(z)^2\right]}{\sqrt{1+z^2/z_R^2}}, \tag{4.2}$$

where E_0 is the amplitude of the electric field, r and z are the cylindrical radial and axial coordinates, and $w(z)$ is the beam size at an axial position z. It is given in terms of the focused waist size w_0 by, $w(z) = w_0\sqrt{1+z^2/z_R^2}$. The Raleigh range $z_R = \pi w_0^2/\lambda$ gives the axial extent of the trap where λ is the wavelength of the light. The trapping potential is thus proportional to the absolute square of the electric filed amplitude, which can be related to the intensity through $I = (1/2)\epsilon_0 c E_0^2$. Thus in a focused laser beam, the potential is minimum (large negative) at focus. Close to the focus, the trapping potential can be approximated to be a harmonic potential

$$U = -\frac{1}{2}\alpha_g E_0^2\left(1 - \frac{2x^2}{w_0^2} - \frac{2y^2}{w_0^2} - \frac{z^2}{z_R^2}\right) = -U_c + \frac{1}{2}\left(K_x x^2 + K_y y^2 + K_z z^2\right). \tag{4.3}$$

where x and y are coordinates in the direction perpendicular to the propagation of the laser beam, $\omega_x = \omega_y = \sqrt{2\alpha_g E_0^2/(M w_0^2)} = \sqrt{(4\alpha_g/c\epsilon_0 M)(I_{int}/w_0^2)}$ and $\omega_z = \sqrt{\alpha_g E_0^2/(M z_R^2)} = \sqrt{(2\alpha_g/C\epsilon_0 M)(I_{int}/z_R^2)}$ are trapping frequencies, where I_{int} is the intensity of the light. Thus more tightly focused laser beams (with small w_0 and Z_R) produce deeper traps. The trapping frequencies depend on the intensity and focus of the laser beam. To get a tight focus, a lens of small focal length should be used. If the lens is not corrected for aberrations, they can produce an observable effect on

the trap. One such effect has been observed in the experiments described in this chapter. The lens was not corrected for spherical aberration and it produced the multiple traps. Thus in Sec 4.2 the theory of the spherical aberration is discussed. In Sec 4.3 the experimental configuration is discussed. The experimental results are presented in Sec 4.4. Finally the lens was replaced with one corrected for spherical aberration and an all-optical BEC was realized (Sec 4.5).

4.2 Spherical aberration

When the first observation of BEC was reported by the Colorado group in 1995 [60], The group led by Randall G Hulet at Rice university also published an article in Physical Review Letters interpreting their results as the observation of BEC [96]. Later they found that the number of atoms had a big uncertainty [97]. Their imaging lens was not corrected for spherical aberration [98], however, the signature of observation of BEC in the original experiment was clear but with less atoms than originally quoted in the article [96].

Spherical aberration arises from the fact that rays traveling far away from the optical axis (non-paraxial rays) are focused closer to a lens than the focus of the paraxial rays. An extensive discussion of the diffraction theory of spherical aberration is given in Born and Wolf [99]. The theory has been extensively developed by Youshida and Asakura [100] and Pu and Zhang [101]. Taking all the wavelets on a lens as point sources and integrating the contribution from the whole lens, the diffraction pattern at the focus of the lens is given by

$$I(u,v) = \frac{1}{w_L^2}\left|\int_0^1 \rho \mathrm{d}\rho \exp\left[-\frac{\rho^2}{(w_L/a)^2}\right]\exp\left[-i\left(\frac{u\rho^2}{2}+k\beta\rho^4\right)\right]J_0(v\rho)\right|^2, \qquad (4.4)$$

where w_L is the diameter of the beam on the lens, a is the diameter of the lens, and $k = 2\pi/\lambda$. The integration variable ρ is the radial coordinate on the lens, normalized

to the size of the lens a. The variables

$$\begin{aligned} u &= \frac{2\pi}{\lambda}\left(\frac{a}{R}\right)^2 z, \\ v &= \frac{2\pi}{\lambda}\left(\frac{a}{R}\right) r, \end{aligned} \tag{4.5}$$

represent the scaled axial and radial coordinates respectively, where R is the radius of the Gaussian reference sphere. The spherical aberration coefficient β_{sph} represents the amount of spherical aberration present in the configutaion and is usually specified in terms of a number of wavelengths. This parameter is given for a lens of focal length f by [102]

$$\beta_{sph} = \frac{w_L^4}{32f^3}\left[\left(\frac{4}{n-1}\right)^2 + \frac{n+2}{n(n-1)^2}\left(B + \frac{2(n^2-1)}{n+2}C\right)^2 - \frac{n}{n+2}C^2\right], \tag{4.6}$$

where n is the refractive index of the lens, $B = (c_1 + c_2)/(c_1 - c_2)$ is known as the shape variable, $c_i = 1/r_i$, $i = 1, 2$; r_i are the radii of curvature of the two surfaces of the lens. $C = (u_1 + u_2)/(u_1 - u_2)$ is known as the conjugate variable, where u_1 and u_2 are the divergence angles of the Gaussian beam before and after passing through the lens. These angles are given by $u_i = \lambda/\pi w_{0i}$, $i = 1, 2$, where w_{01} and w_{02} are the minimum beam waists of the beam before and after the lens. It should be noted that, according to the usual sign convention, if the lens produces a converging beam, then u_2 is negative so that the denominator in the definition of C is not zero.

4.3 Experimental configuration

The aberration theory was initially developed to explain the surprising experimental observation of multiple micro traps. The experimental configuration is as shown in Fig. 4.1. A CO_2 laser beam was first propagated through two lenses in telescope configuration. The telescope consisted of a pair of 12.7 cm focal length plano convex lenses. The second lens of the telescope was placed on a translational stage. A third lens (a meniscus lens) was placed approximately 2 m from the telescope. This lens

was positioned inside the chamber and was not corrected for spherical aberration. It had a focal length of 3.8 mm. The beam size on this lens was controlled by varying the separation of the lenses in the telescope. The FORT light propagated at an angle of 45^{O} with respect to the vertical as shown in Fig. 4.1. The FORT (CO_2) light was focused on the MOT and was switched on when the MOT was turned on. After the turn off of the MOT, about 1.5 million atoms were loaded into the FORT. The trap was imaged after expanding for 3 ms after the FORT was switched off.

4.4 Experimental results

The experimental results are as shown in Fig. 4.2. These three images were chosen to illustrate the effect of the aberration (and the agreement with the theory) for three different values of the aberrations. A spherical aberration coefficient β_{sph} of less than a wavelength was used in Fig. 4.2(a) and 4.2(b). The value of β_{sph} in panels (c) and (d) of Fig. 4.2 was 12.6 wavelengths and in panels of (e) and (f), a value of β_{sph} of 18.2 wavelengths was used. Experimental results are displayed in panels (a), (c), and (e) while numerical simulations are presented in panels (b), (d) and (f).

When the telescope separation was varied in steps of 0.9 mm, the appearance and disappearance of multiple peaks was visible as shown in Fig. 4.3. This figure displays the emergence and disappearence of a trap adjacent to the main trap. The spatial extent of the traps over which the MOT could populate the subtraps was approximately three traps at the most, even though the aberration theory predicts that there can be more traps than just three. A bigger MOT may be able to populate additional traps.

It can thus be seen that spherical aberration which would normally be avoided in a given experimental situation can be used to good effect to produce multiple traps whose separation can be varied. These sub-traps may be useful in atom interferometry and quantum information applications.

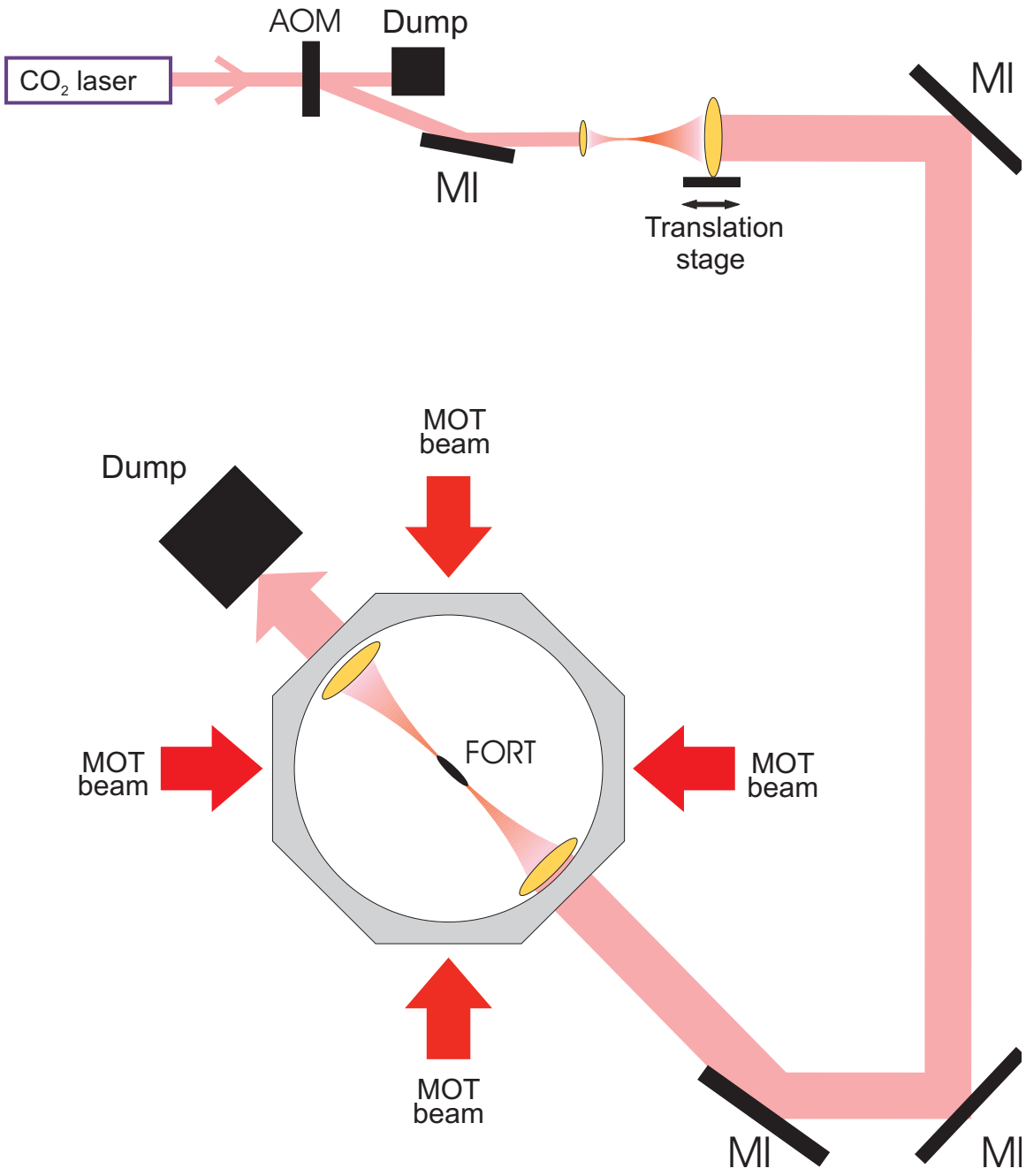

Figure 4.1: Experimental configuration for producing multiple traps using spherical aberration

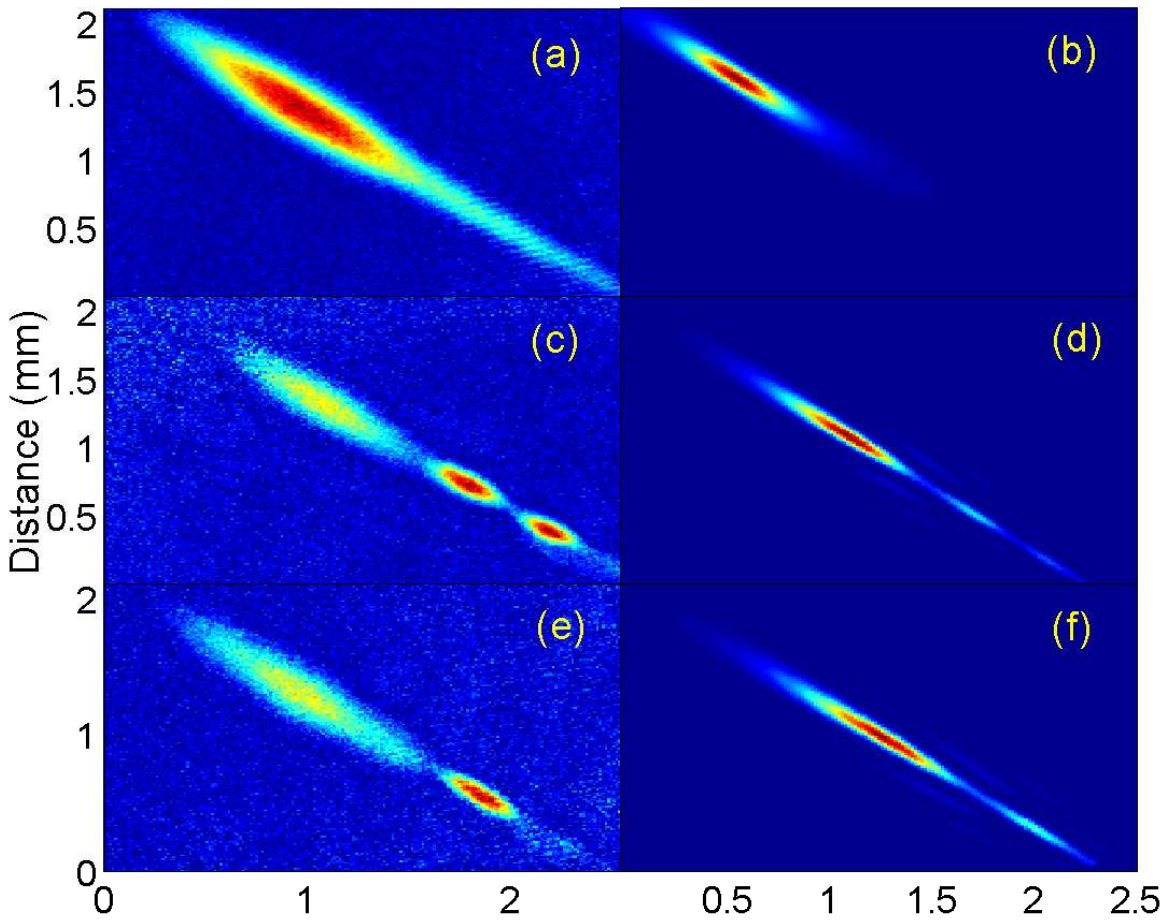

Figure 4.2: Multiple traps resulting from spherical aberration. The abscissa and ordinate are distances in millimeters in each image. (a) The spherical aberration β_{sph} is less than a wavelength because of the small size of the CO_2 laser beam on the primary lens. (c) β_{sph} is 12.6 wavelengths. (e) a strong spherical aberration β_{sph} of 18.2 wavelengths. Figures (b), (d) and (f) are the theoretical potentials corresponding to the cases (a), (b) and (c), respectively. The atoms were imaged after 3.5 ms before the image was taken. The CO_2 laser beam propagates from lower right to the upper left in the images.

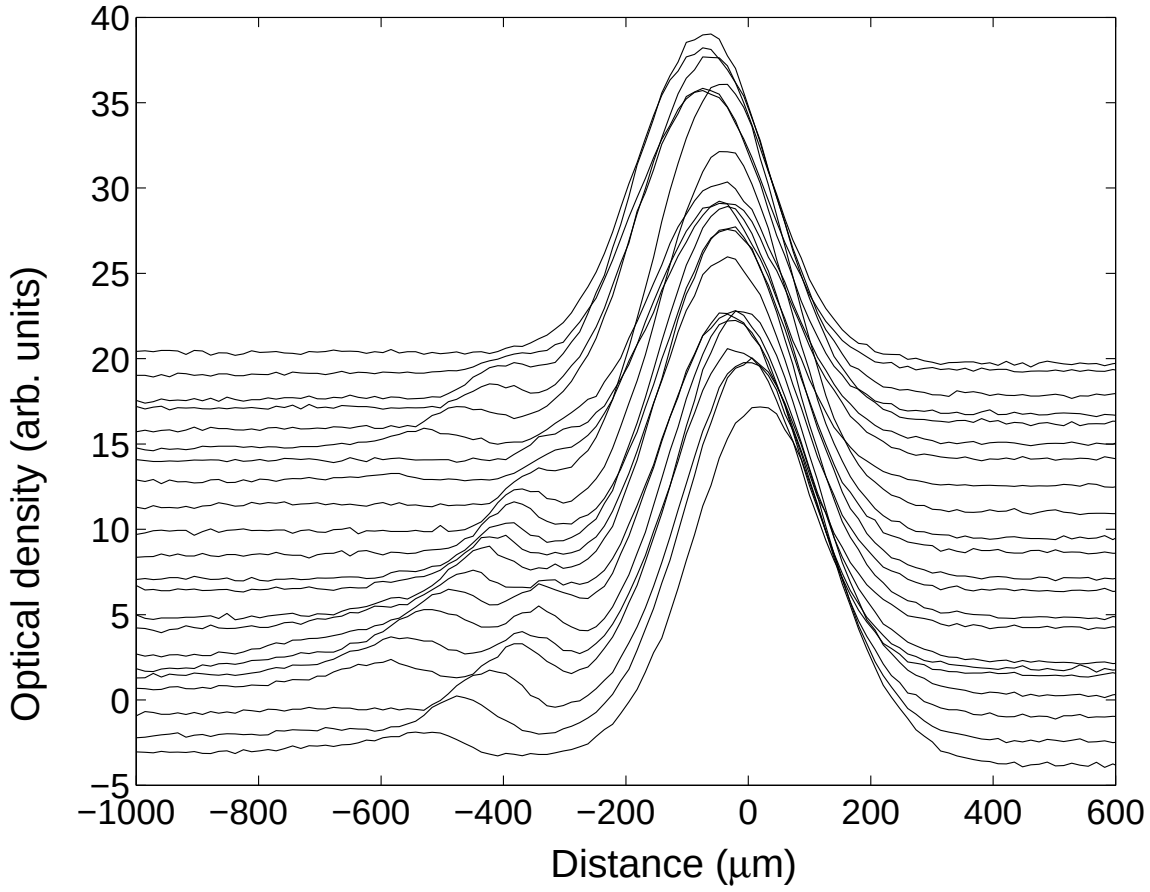

Figure 4.3: The emergence and disappearance of micro traps as the telescope separation was varied.

4.5 Bose-Einstein Condensation

The laser cooled atoms were at a temperature of 100 μK. To cool further and achieve BEC, the second stage of cooling, evaporative cooling, was required. It was found that the loading of the FORT was efficient for a bigger FORT size, while the evaporative cooling worked better for a tighter trap [103]. It was thus proposed to position the second lens of the telescope on a motorized translational stage. The first lens of the telescope was replaced by a 38.1 mm focal length lens and the third focusing lens was replaced with an aberration free 38.1 mm focal length lens. The separation of the two telescope lenses was initially set to 173.7 mm. These parameters gave a beam waist after the third lens at the site of MOT of 120 μm as shown in Fig. 4.4. This configuration loaded about 4 million atoms at the focus of the CO_2 laser beam. The MOT light was extinguished after the FORT was loaded. The FORT was then compressed by moving the second lens of the telescope 20 mm closer to the first lens of the telescope. This brought the waist size to 8 μm. During the process, the beam size on the third lens was monitored to ensure that it did not exceed the size of the lens. This is shown in Fig. 4.4c. Figure (4.4a) shows the position of the focus relative to the focal plane of the third lens. This plot shows that the focus can be moved over a range of 5.5 mm. About 2 million atoms were observed in the FORT after moving the telescope lens. As the FORT was compressed, the evaporative cooling was initiated. The laser power was ramped down exponentially from 35 W to 1 W in 6 s. The power was further ramped down for another 2.5 s, almost linearly, to a final value of 100 mW. At the end of this process, a BEC with 30,000 atoms was formed. The trap was turned off after waiting for another 0.5 s. Typically after 8 ms expansion, the BEC was imaged. Figure 4.5 shows an absorption image of the BEC and the the 1D distribution of the atoms in the BEC. The cloud was imaged by pulsing an on resonant light for a duration of 100 ns. A signal image was subtracted from the reference image to obtain the distribution of atoms in the BEC.

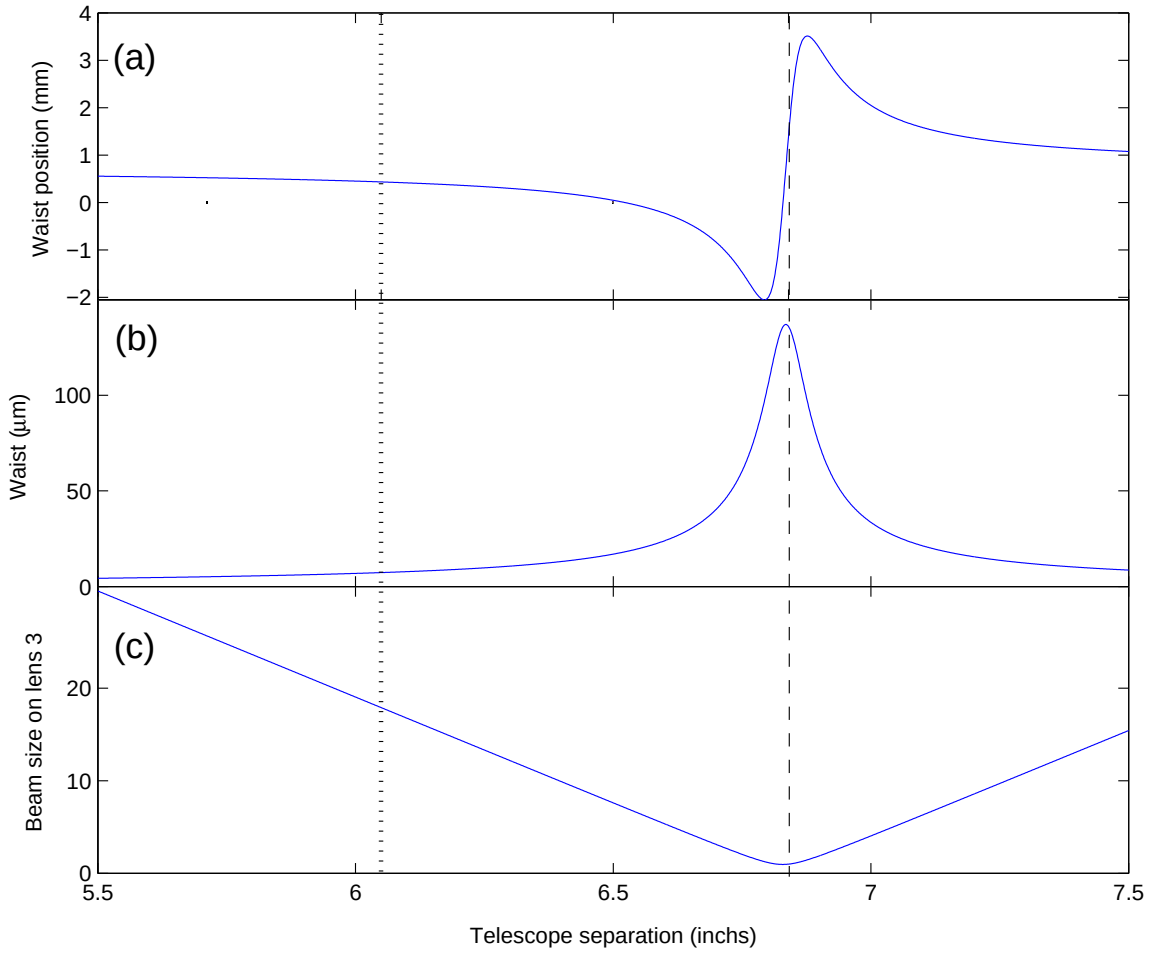

Figure 4.4: Plots showing the waist and position of CO_2 laser beam at various positions as a function of the telescope separation. (a) Plot of the position of the CO_2 beam waist relative to the focus of the third focusing lens, (b) plot of the waist size and (c) The beam size on the third focusing lens as a function of the telescope separation. The dashed line shows the starting position for loading atoms and the dotted line shows the end position corresponding to tighter trap for evaporation and the position of the BEC.

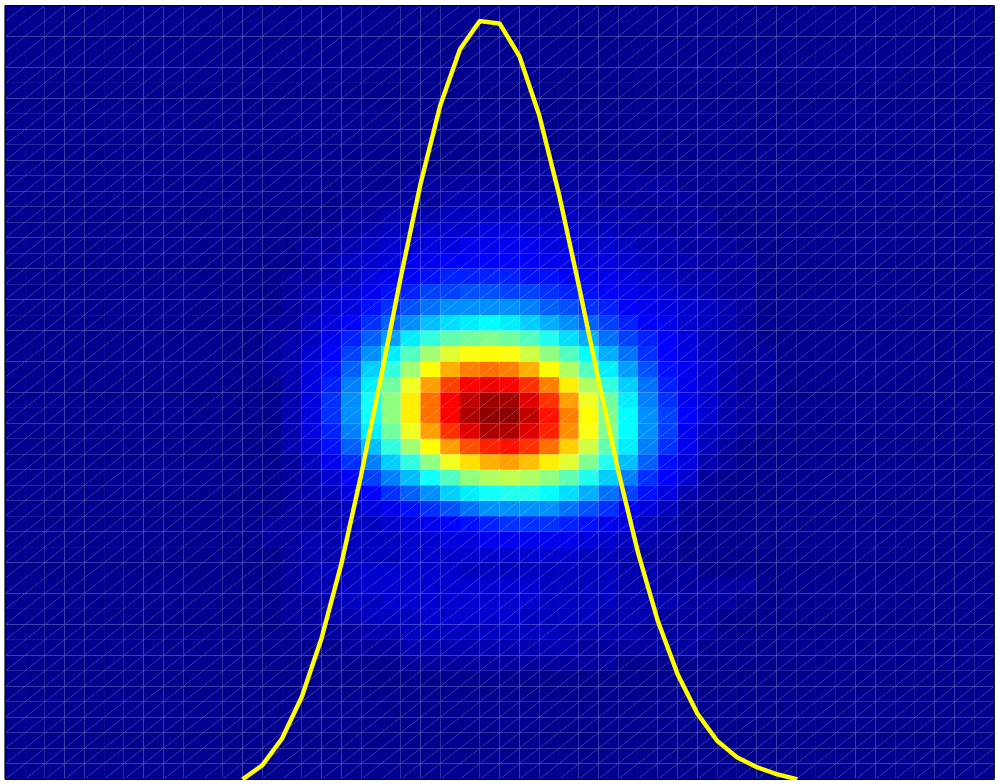

Figure 4.5: TOF image of BEC after 8 ms of expansion. Also shown is the plot of a 1 D integrated profile of the BEC.

Thus a BEC of 30,000 atoms was routinely produced and imaged. Once the BEC was successfully produced, the experiments of kicking the BEC were started. This is detailed in the following chapter.

CHAPTER 5

The Quantum δ-kicked accelerator in a BEC

5.1 Introduction

Quantum Accelerator Modes (QAMs) were observed using atoms from a MOT as detailed in Chapter 3. However, a sample of Rb atoms at a temperature of 15 μK has a momentum spread of 4 photon recoils which can mask many effects when a kicking potential is applied. A BEC has a much narrow distribution (less than a photon recoil) making it the ideal candidate for experiments on kicked atom waves. In this chapter the narrow distribution of momentum is utilized to explore a kicked system [104]. QAMs are observed for rational fraction of the Talbot time. In this chapter the QAMs at primary times (multiples of half-Talbot time) are considered. The QAMs appearing at other times are called high-order resonances and will be discussed later. Higher order *modes* should not be confused with higher order *resonances*.

5.2 Theory recap

The theory was discussed in chapter 2. The final results are summarized for completeness in this section. The momentum transferred to a (p, j) QAM is given by Eq. (2.52) as

$$p_{\mathrm{QAM}} = -\frac{\eta\tau n_p}{\epsilon} + \frac{2\pi n_p}{|\epsilon|}\frac{\mathsf{j}}{\mathsf{p}}, \tag{5.1}$$

The initial momentum at which a QAM appears is given by Eq. (2.39)

$$\beta_{\mathrm{QAM}} = \frac{2\pi L'}{\tau} + \frac{1}{2} - \frac{\eta}{2}. \tag{5.2}$$

The ϵ-classical theory makes use of the fact that for kicking periods close to a resonance time, the system can be described by the classical mapping of Eqs. (2.46)

$$\begin{aligned} J_{n_p+1} &= J_{n_p} + \tilde{k}\sin(\theta_{n_p+1}) + \left(\frac{\epsilon}{|\epsilon|}\right)\tau\eta \\ \theta_{n_p+1} &= \theta_{n_p} + \left(\frac{\epsilon}{|\epsilon|}\right) J_{n_p} \end{aligned} \tag{5.3}$$

As discussed previously the appearance of a stable island in the poincarè plot is attributed to the presence of a QAM.

According to Eq. (5.2), at $T = T_{1/2}$, (i.e., $\tau = 2\pi$), a QAM can occur when β is close to 0.5. Thus the unit cell in phase space has a width in momentum of 1 $\hbar G$. For a sample of cold atoms, the momentum width of the atomic distribution is much larger than the $1\hbar G$ width of this phase-space. Thus if using cold atoms, the features within the phase space, such as the island structure, can not be explored. Since the OSUBEC has a width of 0.056 $\hbar G$ [105], it can be used to explore the phase space of the quantum δ kicked accelerator which produced a quantum chaotic system.

5.3 Experimental configuration

The experimental set up is as shown in Fig. 5.1. The BEC was produced as discussed in Section 4.5 using a single focused CO_2 laser beam. The kicking light exiting the fiber was aligned with the BEC and was retroreflected to create the standing wave. The kicking light was aligned at 41^{O} to the vertical giving $g' = 6$ ms^{-2}. In the experimental sequence, a BEC of 30000 atoms was produced. The trap was turned off and after waiting a variable amount of time for the BEC to acquire the initial momentum β, a variable number of kicks was applied to the atoms at a kicking period which could be varied. After the sequence of kicking was complete, the resulting cloud was typically allowed to fall for 10 ms and imaged to measure the momentum distribution using time-of-flight method. Figure 5.2 shows the typical result of an experiment.

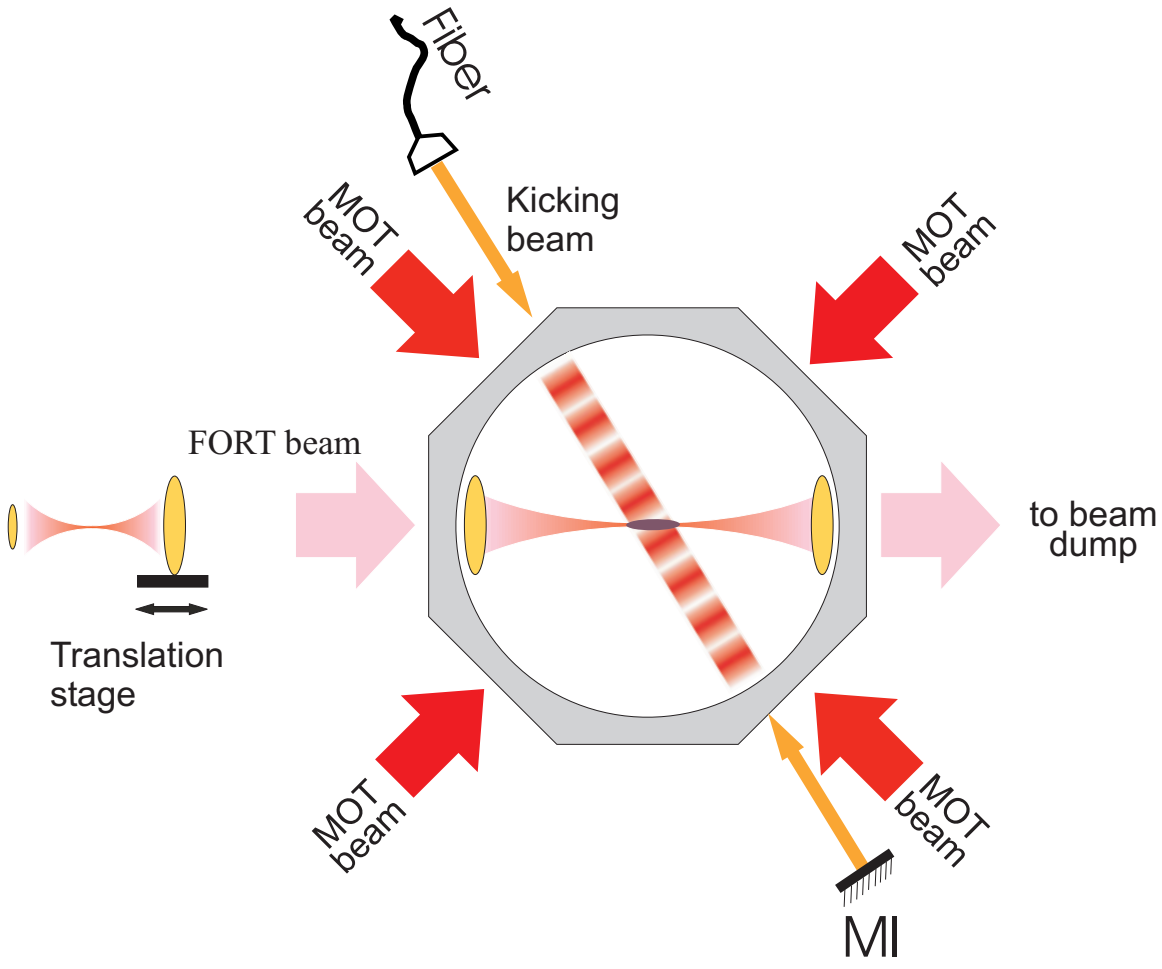

Figure 5.1: Experimental configuration for the quantum δ-kicked accelerator. The kicking beam exiting the fiber was aligned with the BEC.

5.4 Data analysis

The experimental data was often noisy, necessitating the implementation of a Fourier technique for its analysis. This was accomplished using Matlab. The Fourier transform technique involves the elimination of unwanted spatial frequencies which contain most of the noise. The unwanted frequencies in the data for the experiments described in this thesis include both high and low frequency components. Figure 5.2 shows a three dimensional plot of the raw data that we typically obtain in experiments described in this thesis, while Fig. 5.3 showing the same data after Fourier analysis. It is clear that removing the unwanted frequencies in the acquired data enables the detection of much weaker signals in the experimental data. This Fourier analysis technique was also useful in the observation of the high order resonances described in Chapter 6.

5.5 BEC subject to 1 kick

When a plane wave $|m\rangle$ is subjected to a sinusoidal δ potential (in the temporal domain), the sinusoidal potential acts like a thin phase grating and diffracts the atoms into various momentum states given by

$$e^{-i\phi_d \cos(\theta)}|m\rangle = \sum_{i=-\infty}^{\infty} (-i)^l J_l(\phi_d)|m+l\rangle. \tag{5.4}$$

Hence the population of the momentum states are given by the absolute square of Bessel functions. In the experiments, the value of ϕ_d was estimated by comparing the populations of the orders to the Bessel function values. Figure 5.4 shows a comparison between the experimental results and a fit to the Bessel functions. For all the experiments described in this thesis, the value of ϕ_d was estimated using this method. Recently this same method was used by another group to estimate the value of ϕ_d [106].

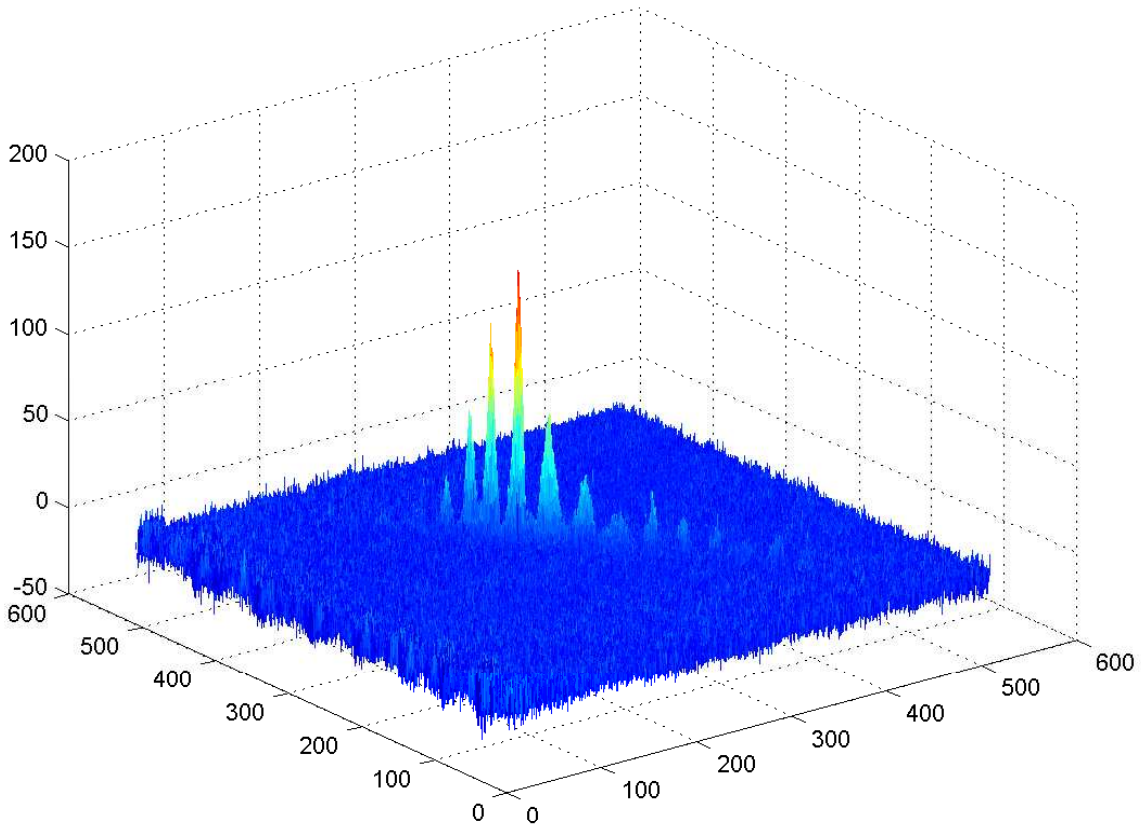

Figure 5.2: Momentum distribution before Fourier analysis. The signal of the weaker momentum states is about the same size as the noise.

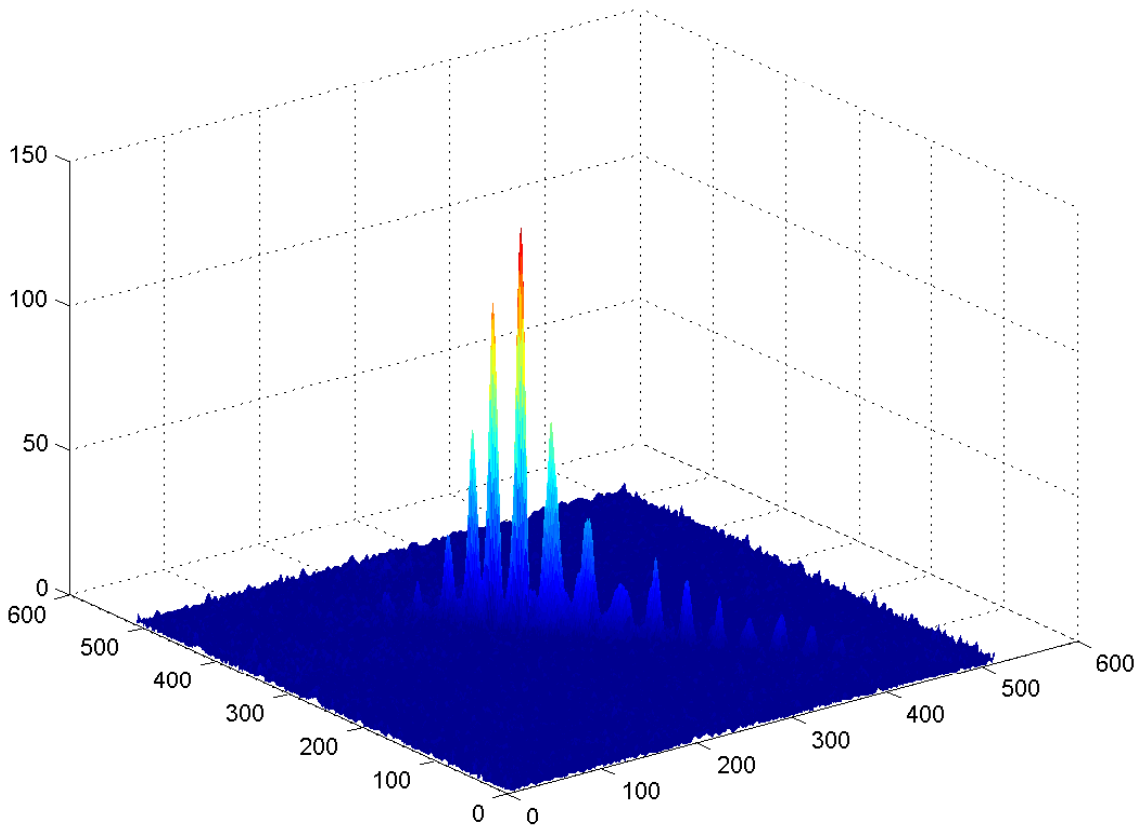

Figure 5.3: Momentum distribution after analyzing and filtering the noise using a Fourier transform. The momentum peaks which were the size of the noise remain while the noise in Fig. 5.2 is greatly reduced.

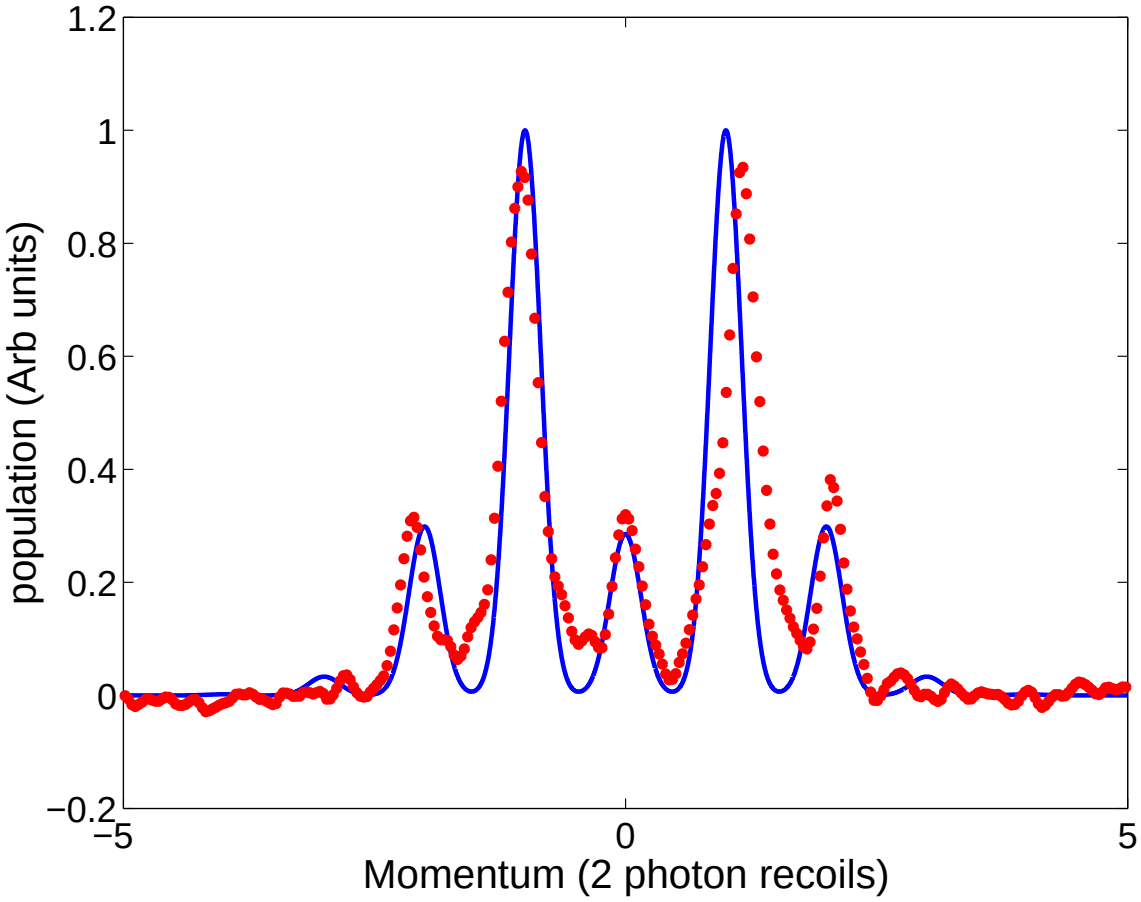

Figure 5.4: Experimental and theory curves for diffraction of BEC when the BEC was subjected to 1 kick. A value of $\phi_d = 1.85$ was used. Red points correspond to the experimental data.

5.6 Behavior of QAM as a function of kicks

A QAM can be identified as a linear increase of momentum to some atoms as more kicks are applied near a resonance time. Figure 5.5 shows the behavior of a QAM as a function of kicks n_p. The figure was generated by stacking a series final momentum distributions. Figure 5.5 shows that a QAM primarily consists of four orders. However, it was observed that, depending on the value of the ϕ_d, more orders could be populated. The inset in the figure shows a plot of the momentum distribution after $n_p = 21$ kicks and gives a better idea of the population of atoms in a QAM. The value of ϕ_d for this experiment was 1.6. It has been observed that more than 60% of the atoms could be coupled into a QAM using a BEC,whereas using cold atoms, a maximum of 20% populated a QAM [45]. The mean energy was calculated for the case of the δ-kicked accelerator and plotted in Fig. 5.6. This can give a good signature for the presence of a resonance where the mean energy is expected to rapidly increase. The mean energy of Fig. 5.6 was generated from the data of Fig. 5.5.

5.7 Acceleration dependence, g', of the δ-kicked accelerator

The momentum of atoms participating in a QAM varies linearly with acceleration g'. For a kicked rotor ($g' = 0$ ms^{-2}) atoms move out from the zero momentum state symmetrically. For the accelerator, $g' \neq 0$, the symmetry is broken, and QAM appear on only one side. The theory predicts that the momentum of a QAM is linear in g'. To test this idea a scan of g' at a kicking period of 36.2 μs was performed and is displayed in Fig. 5.7. This figure was generated by stacking the images vertically each taken for a value of g' which was varied in steps of 1 ms^{-2}. The images were generated after 25 kicks.

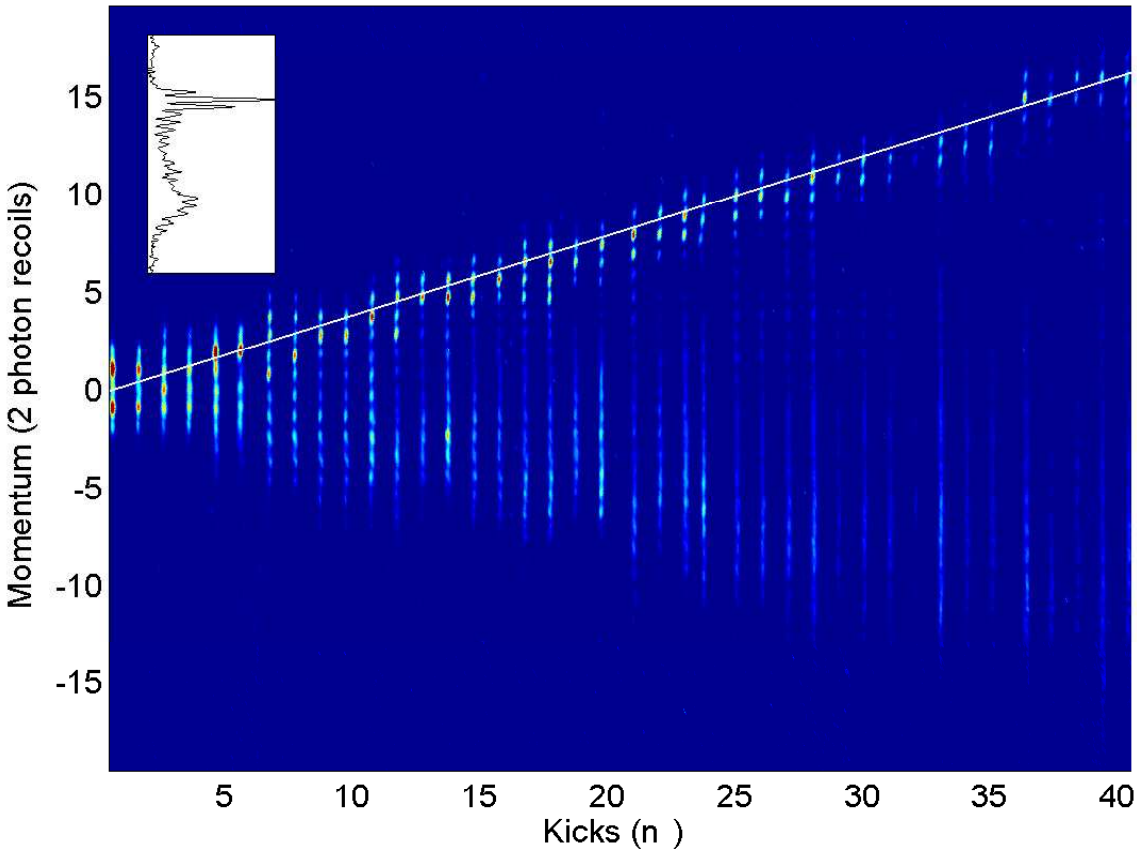

Figure 5.5: QAM as a function of kicks. Atoms participating in a QAM have the momentum increasing linearly with number of pulses. The solid line is from Eq. (5.1). The inset shows the momentum distribution for $n_p = 21$. The values of $T = 61$ μs and $\phi_d = 1.4$ were used

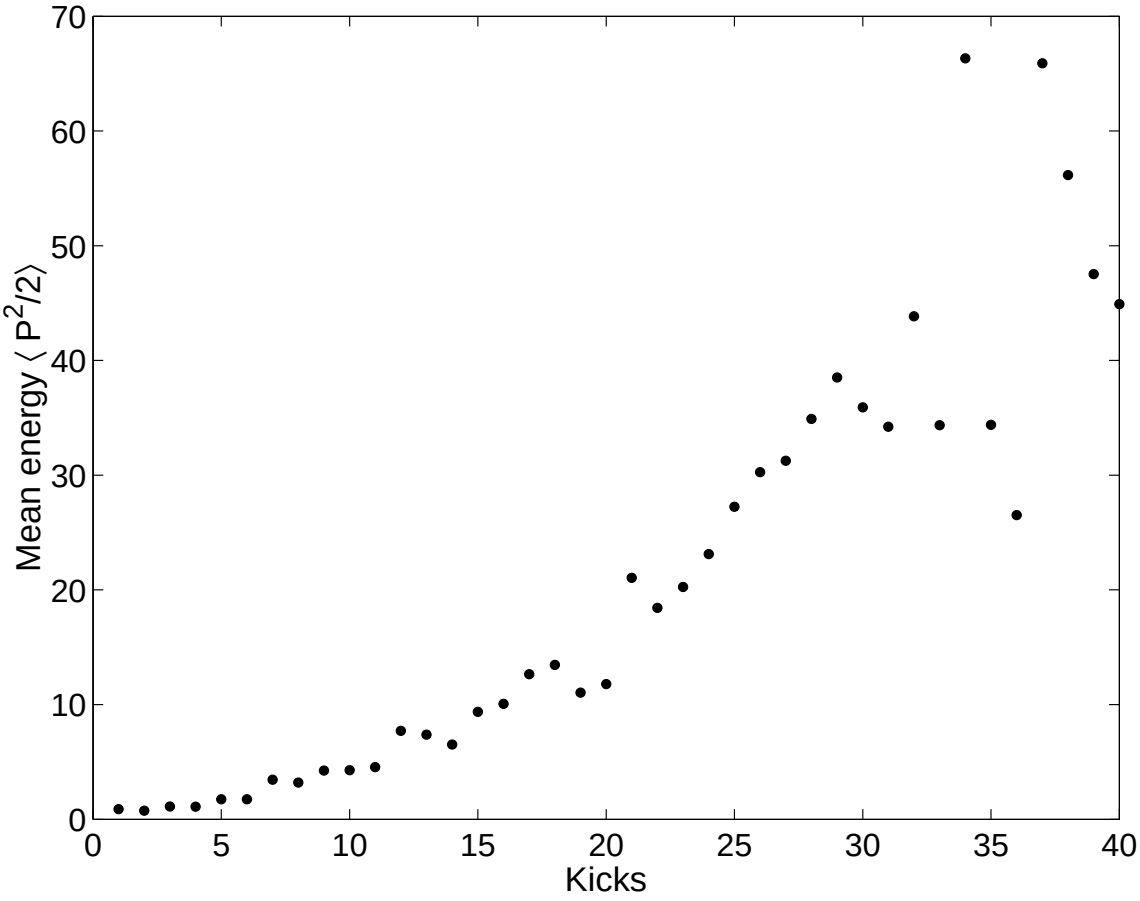

Figure 5.6: Variation of mean energy as a function of kick number for the same data presented in Fig. 5.5. This plot shows that the mean energy varies approximately quadratically with kicks which is expected for the case of kicked rotor near a resonance.

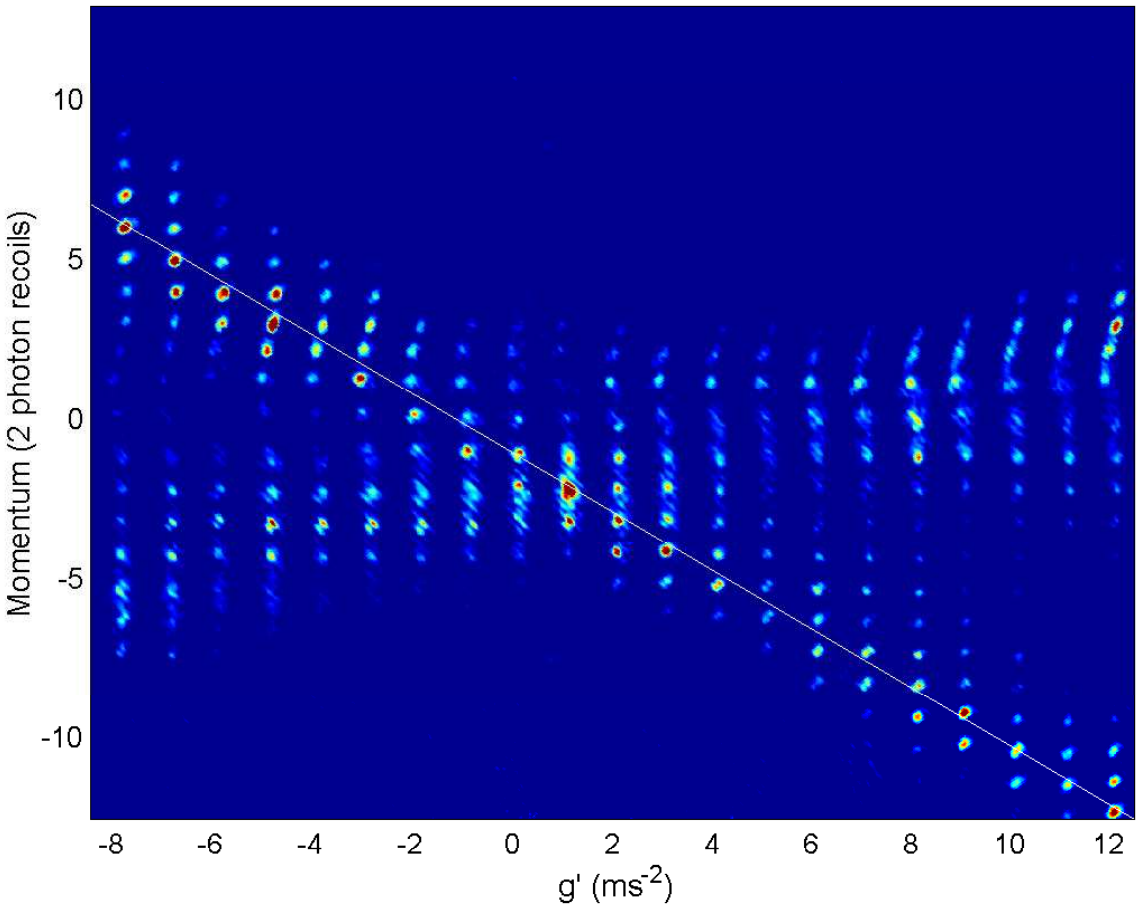

Figure 5.7: A scan of applied gravity g' after 25 kicks at a kicking period of 36.2 μs. The line is a plot of Eq. (5.1).

5.8 Scanning the kicking period across a resonance

The signature of a resonance in the QDKA is the nearby presence of a QAM, with the momentum transferred to atoms participating in a QAM diverging to infinity as the period approaches the resonance time. Figures 5.8 and 5.9 show scans of the kicking period across the Talbot time ($2T_{1/2}$) after 10 kicks. A value of $g' = 6$ ms^{-2} and $\phi_d = 1.4$ was used in both of these period scans. This value was chosen since one kick at this ϕ_d diffracted atoms into momentum orders $l = -1,\ 0$, and 1 equally. An initial momentum of $1.5\hbar G$ was used in Fig. 5.8. This figure shows that only the QAM with positive momentum is populated. This is because the initial momentum used in the experiments to generate Fig. 5.8 efficiently populated only the mode with positive momentum. For an initial momentum of $1.3\hbar G$ used in Fig. 5.9, a QAM with negative momentum was efficiently populated. This behavior motivated further study on the dependence of the QAM on the initial momentum β.

5.9 Dependence of QAM on the initial momentum β

The narrow momentum distribution of the BEC can be exploited to study the dependence of the QAM on initial momentum as shown in the Fig. 5.10. The initial momentum in the experiment was varied by allowing the BEC to expand variable amounts of time before kicking. However, the expansion time after kicking was fixed to ensure that the momentum orders were separated by the same amount for each initial momentum. Thus the whole distribution shifted downwards as the scan proceeded which can be seen in Fig. 5.10. Two different kicking periods were chosen (on either side of the Talbot time). For Fig. 5.10(a) the kicking period was 61 μs and for 5.10(b) it was 72.2 μs. The experiments were performed using 10 kicks at $\phi_d = 1.4$. The period of appearance of the QAM in initial momentum is $\sim 0.5\ \hbar G$ as expected from Eq. (5.2). This shows that a QAM appears for initial momenta separated by

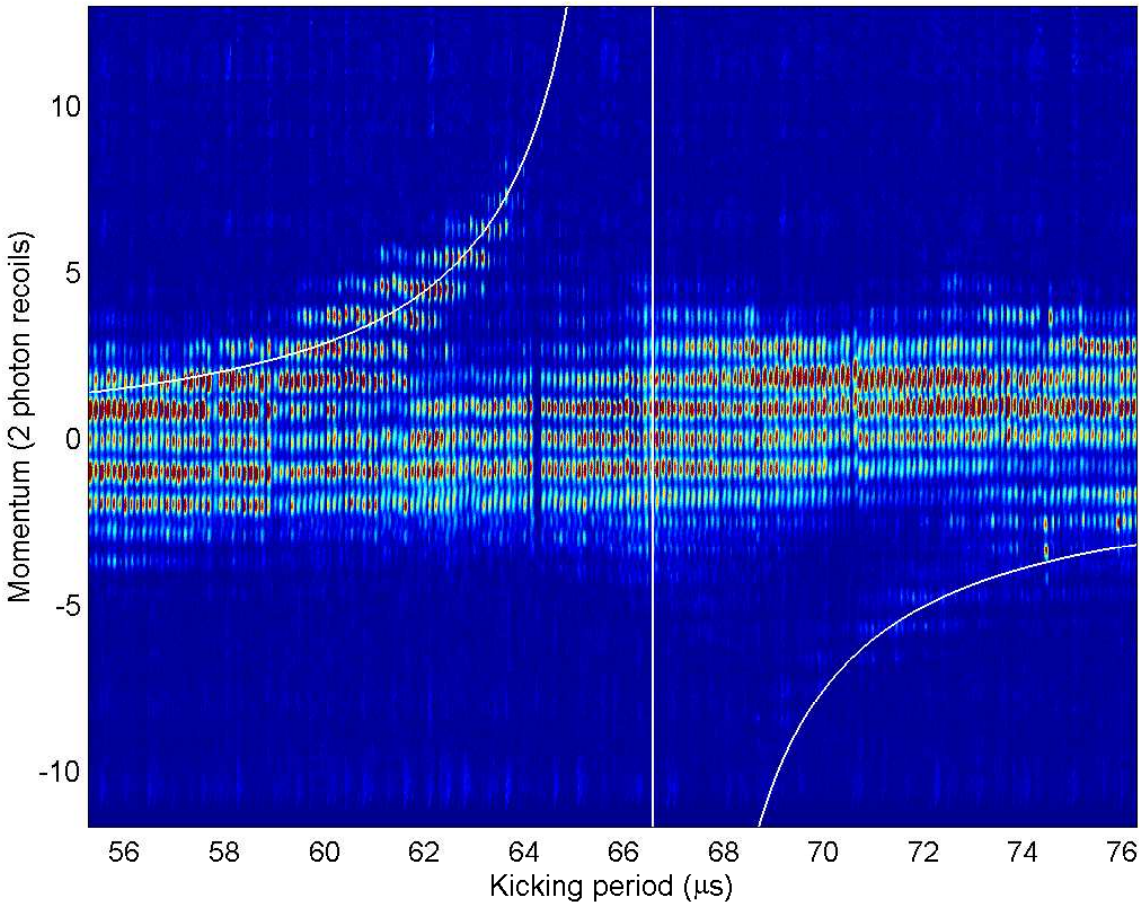

Figure 5.8: A QAM as a function of kicking period for an initial momentum of 1.5 $\hbar G$. The QAM with positive momentum is populated significantly. The parameters used are $\phi_d = 1.4$ and $n_p = 10$. The solid line is a plot of Eq. (5.1).

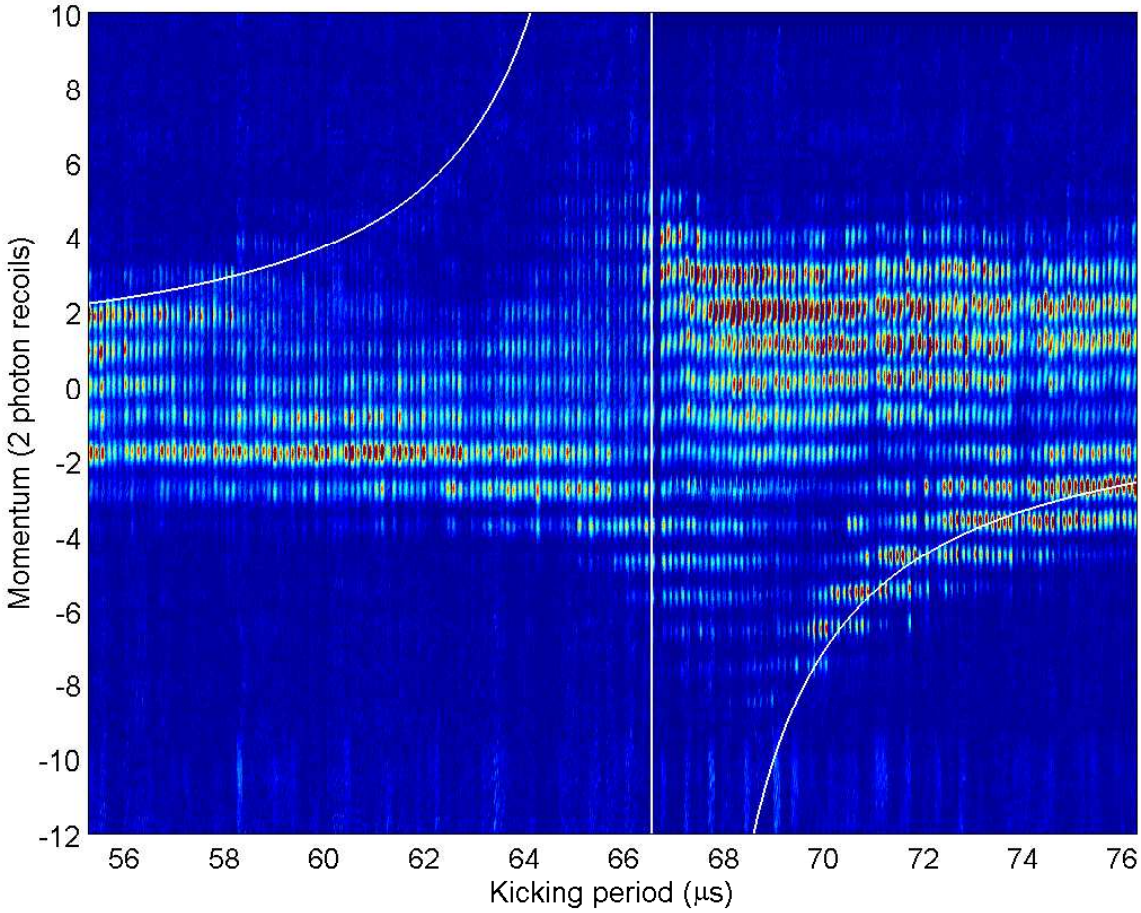

Figure 5.9: A QAM as a function of kicking period for an initial momentum of 1.3 $\hbar G$. The QAM with negative momentum was efficiently populated. The parameters used are the same as that in Fig. 5.8 except for the initial momentum. The solid line is a plot of Eq. (5.1).

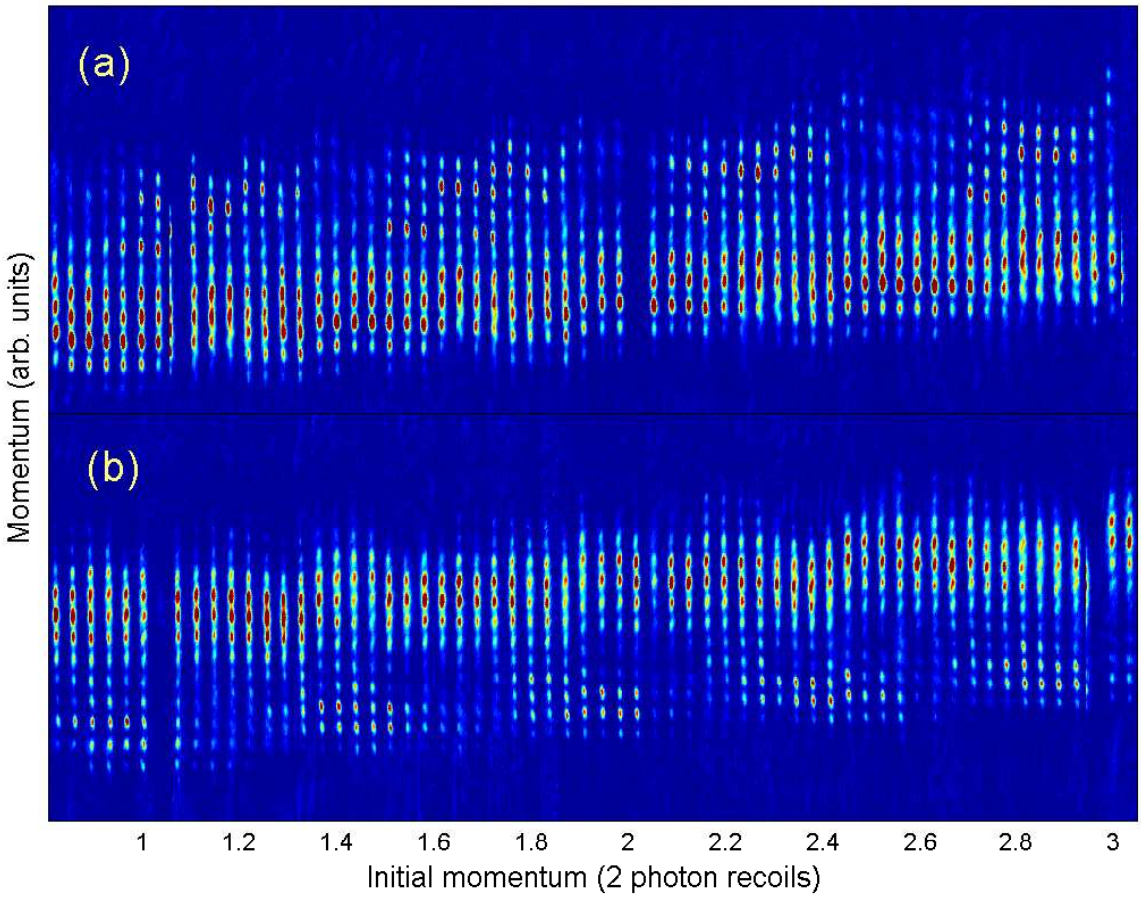

Figure 5.10: Dependence of QAM on the initial momentum showing that the QAM appears once every $\sim 0.5\ \hbar G$. In (a) a kicking period of 61 μs was used and in (b) 72.2 μs was used. The two periods were chosen symmetrically on either side of the resonance appearing at the Talbot time 66.4 μs.

$\Delta\beta_{QAM} = 2\pi/\tau$. Both panels in Fig. 5.10 show that a QAM is populated not only for the initial momenta separated by 0.5 $\hbar G$ but also for a range of initial momenta near these values. As will be seen shortly, this spread in initial momentum can be interpreted as evidence for the existence of stable island in phase space with a size in momentum given by the spread of the initial momenta for which the QAM appears.

5.10 Phase-space plots

The ϵ-classical description of the δ-kicked accelerator and the resulting map of Eq. (5.3) shows that the value of $\tilde{k}$ plays important role in the dynamics. For small $\tilde{k}$, the dynamics are regular and predictable. However, as $\tilde{k}$ increases, chaotic regions start to develop. For large $\tilde{k}$, the islands become elongated and higher period p fixed points start to appear as displayed in the phase space portraits of Figs. 5.11 and 5.12. When a wavepacket is trapped in an island, stable quantum accelerator modes are formed [76]. Thus the maps in Figs. 5.11 and 5.12 can be used to theoretically estimate the size of an island. Figure 5.10 where the initial momentum was scanned, was used to estimate the range in initial momentum over which a QAM appears. Several such initial momenta scans (for different values of $\tilde{k}$) were performed to estimate the size of the island experimentally. These results were plotted and are displayed in Fig. 5.13. The results indicate that there is a good agreement between the theory and experiments. The trend that the island gets elongated in the momentum direction is clearly visible in this figure. The experimental limitations did not allow the observation of higher p fixed points since there was not a good overlap of the BEC and the island for large $\tilde{k}$. For small $\tilde{k}$, the orders were not efficiently populated to observe the QAM. To vary $\tilde{k}$ in Fig. 5.13, both ϕ_d and the kicking period (and thus ϵ) were varied. The island size is quoted in units of ΔJ which is related to physical momentum in dimensionless units, β, according to the relation $\Delta\beta = \frac{\Delta J}{\tau}$.

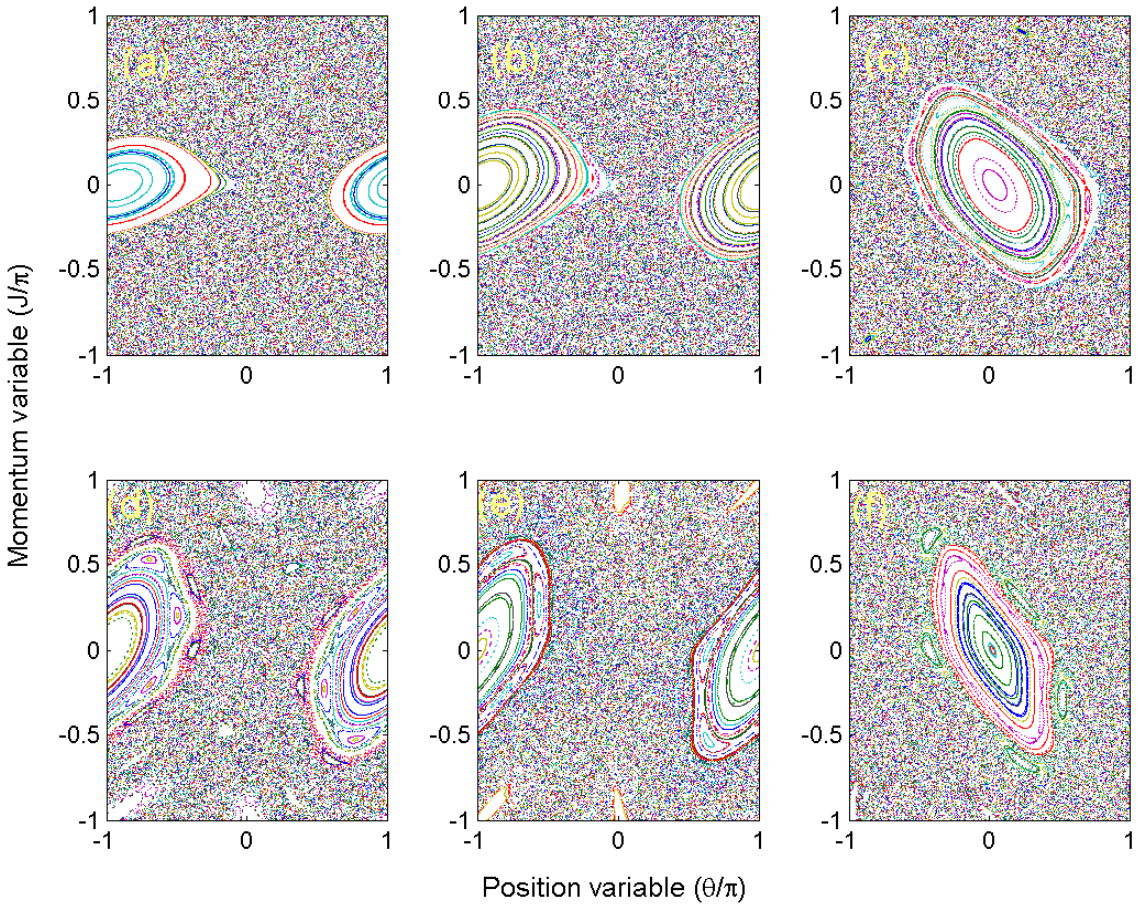

Figure 5.11: Phase-space plots of the quantum δ-kicked accelerator used for calculating the size of the island near the half-Talbot time. The value of $\tilde{k}$ used was (a) 0.36, (b) 0.6433, (c) 1.8047, (d) 1.3515, (e) 1.7764, (f) 1.975.

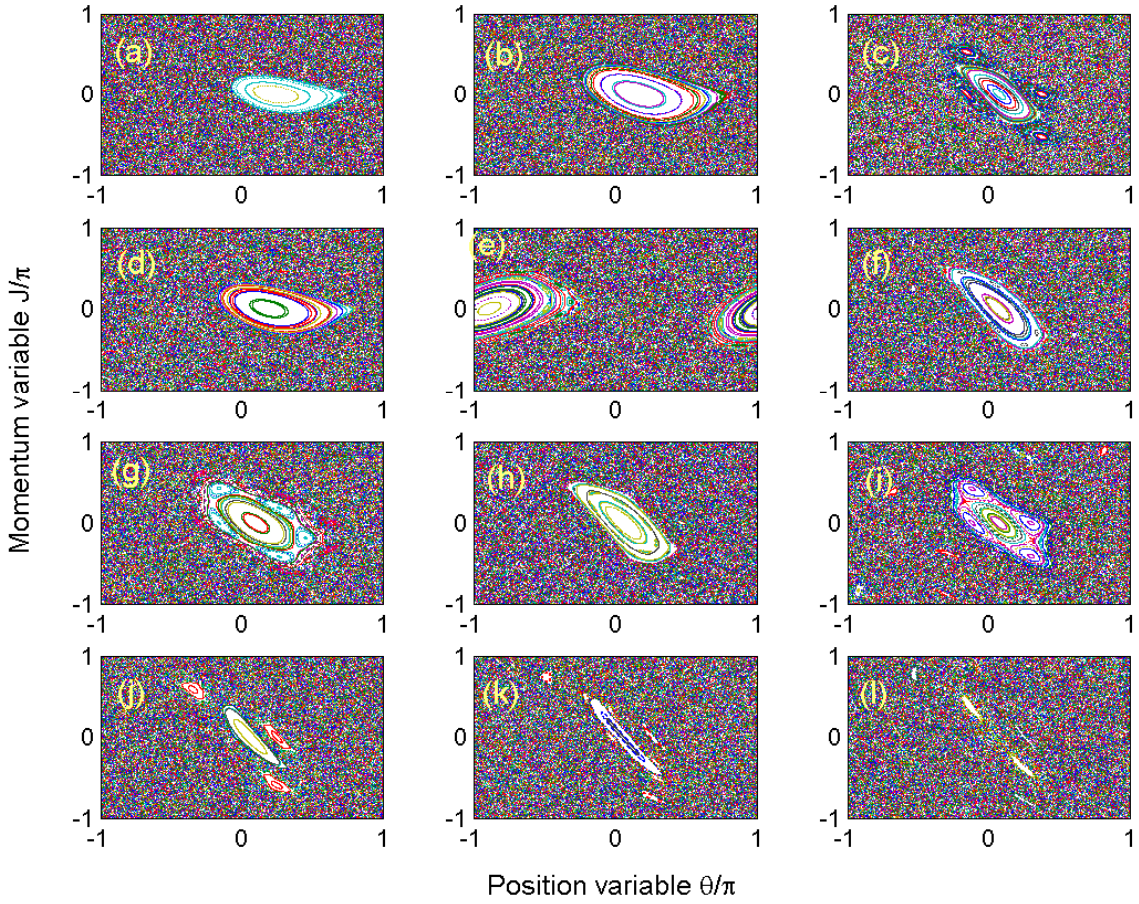

Figure 5.12: Phase-space plots of a quantum δ-kicked accelerator near the Talbot time. Panels (a) through (i) were used for calculating the size of the island. The overlap of BEC and the island was not appreciable for panels (j) to (l) and hence no QAM was observed experimentally for those conditions. The value of $\tilde{k}$ used was (a) 0.6963, (b) 0.9796, (c) 2.3960, (d) 0.8380, (e) 1.0466, (f) 2.7650, (g) 1.7075, (h) 2.6713, (i) 2.2439, (j) 3.5291, (k) 4.0665 and (l) 4.3207.

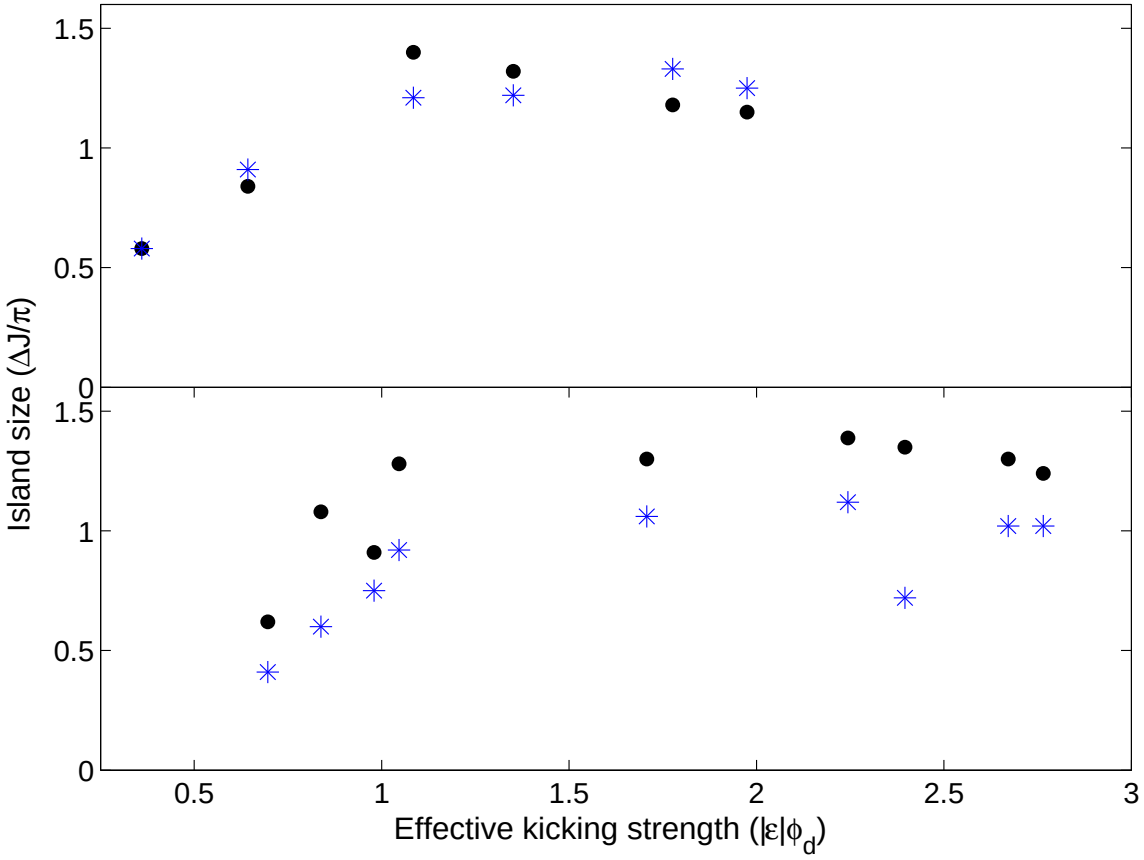

Figure 5.13: Plot of island size as a function of effective kicking strength $\tilde{k}$. The asterisks are inferred from the maps of Figs. 5.11 and 5.12. The filled circles are determined from the experiments.

5.11 Conclusions

The exploration of phase space was successfully achieved by taking advantage of the narrow momentum width of the BEC and the correspondence between classically chaotic system and its quantum version. The signature of resonance of a quantum δ-kicked accelerator, the QAM was observed using BEC and it was found that more than 60% of the atoms can be coupled into the QAM. (It was found that depending the value of ϕ_d, the number of orders populated into a QAM can be varied.) The dependence of the QAM on the kicking period, acceleration, kicks and initial momentum was studied. With this understanding of primary resonances, the experiments to observe the high-order resonances that occur at a rational fraction of the Talbot time was undertaken and these form the context of next chapter.

CHAPTER 6

High-order resonances of the Quantum δ-Kicked Accelerator

6.1 Introduction

The quantum resonances of a δ-kicked accelerator are formed for kicking periods at rational fractions of the half-Talbot time $T_{1/2}$. In chapters 2 through 5, only primary resonances appearing for kicking periods at integer multiples of the half-Talbot time $T_{1/2}$ have been discussed. Recently several of these higher order quantum resonances for the quantum δ-kicked rotor were observed using both BEC [26, 27] and a thermal sample of atoms [107]. Such resonances have also been investigated theoretically for a δ-kicked system within a harmonic potential (the δ-kicked harmonic oscillator) [108]. The numerical simulations suggested that several high order resonances of the quantum δ- kicked accelerator can be observed within the parameter ranges accessible to experiments. In this chapter the observation of these higher order resonances and their associated QAMs is reported and a generalized ϵ-classical theory of QAM is described. In addition, by treating the standing light wave as a diffraction (phase) grating and using a picture analogous to the fractional Talbot effect in optics [109, 110], the internal momentum state (diffraction order) structure of the QAMs can be explained using a rephasing model. Finally, by examining how the momentum states rephase with one another, it is possible to explain why only atoms with certain initial momenta can participate in a QAM [111].

6.2 Theory of high order resonances

The theory of the resonances occurring at kicking periods which are multiples of the half-Talbot time was discussed in chapter 2. The rephasing model developed in chapter 2 applies to the primary resonances. In this section, these theories are extended to incorporate higher-order resonances.

6.2.1 The ϵ-classical theory of high order resonances

In this section the theory discussed in detail in the article by I. Guarnari *et al.* [112] is reviewed. The evolution operator of a wave packet under the time dependent Hamiltonian of the δ-kicked accelerator in a frame falling with acceleration of g' is given by Eq. (2.32),

$$\hat{U}_{n_p} = e^{-i\phi_d \cos(\hat{\theta})} e^{-(i\tau/2)(\hat{N}+\beta+\eta n_p+\eta/2)^2}, \tag{6.1}$$

where ϕ_d represents the kicking strength, τ represents the kicking period and η represents the acceleration of the kicked accelerator. Higher order resonances are expected when T is a rational fraction (a/b) of $T_{1/2}$ [113, 26], where a and b are integers. For the quantum δ-kicked rotor (KR), $\eta = 0$, the resonances occur for

$$\tau_r = 2\pi(a/b) \tag{6.2}$$

$$\beta = \beta_r = \frac{L'}{a} + \frac{b}{2}, \tag{6.3}$$

where L' is an integer. The subscript r refers to resonant parameters in Eqs. (6.2) and (6.3). For the KR, using Poission's summation formula, the resonant evolution of the atomic wave function $\psi(\theta)$ is given by [112, 113]

$$\hat{U}_{res}\psi(\theta) = \mathrm{e}^{-i\phi_d \cos(\theta)} \sum_{s=0}^{b-1} A_s \psi(\theta - 2\pi s/b) \tag{6.4}$$

where

$$A_s = \frac{1}{b} \sum_{l=0}^{q-1} \mathrm{e}^{-i\pi a(l+\beta_r)^2/b} \mathrm{e}^{2\pi i s l/b}, \tag{6.5}$$

and $\hat{U}_{res}$ is the one kick resonant evolution operator of the kicked rotor

$$\hat{U}_{res} = \mathrm{e}^{-i\phi_d \cos\theta} \mathrm{e}^{-i(\tau/2)(\hat{N}+\beta_r)^2}. \tag{6.6}$$

Expressing Eq. (6.1) in terms of $\hat{U}_{res}$, and writing the parameters τ and β using,

$$\tau = 2\pi(a/b) + \epsilon \quad \text{and} \tag{6.7}$$

$$\beta = \beta_r + \delta\beta, \tag{6.8}$$

one obtains

$$\hat{U}_{n_p} = U_{res} \mathrm{e}^{-i(\epsilon/2)(\hat{N}+\beta_r)^2} \mathrm{e}^{-i\tau(\delta\beta+\eta/2+\eta n_p)\hat{N}}. \tag{6.9}$$

Using Eqs. (6.4) and (6.5), Eq. (6.9) can be written as

$$\langle\theta|U_{n_t}\psi\rangle = \mathrm{e}^{-i\phi_d\cos\theta} \sum_{s=0}^{b-1} A_s \tilde{\psi}(\theta - 2\pi s/b - \tau\delta\beta - \tau\eta/2 - \eta\tau n_p) \tag{6.10}$$

where

$$\tilde{\psi}(\theta) = \mathrm{e}^{-i(\epsilon/2)(\hat{N}+\beta_r)^2}\psi(\theta). \tag{6.11}$$

If ϵ plays the role of the Planck's constant, then for small $|\epsilon|$, Eq. (6.11) can be described using a map [112]

$$\begin{aligned} J_{n_p+1} &= J_{n_p} + \delta_{n_p} + \tau\eta + \tilde{k}\cos(\theta_{n_p+1}) \\ \theta_{n_p+1} &= \theta_{n_p} + J_{n_p}, \end{aligned} \tag{6.12}$$

where $J_{n_p} = I_{n_p} + \tau(\delta\beta + \eta n_p + \eta/2) + 2\pi s_{n_p}/b$, $\delta_{n_p} = 2\pi(s_{n_p+1} - s_{n_p})/b$, $I = \epsilon N$ and $\tilde{k} = \phi_d\epsilon$. The integers s_{n_p} take values from 1 to b and are arbitrary. Thus, there are b^{n_p} maps for a given set of experimental parameters and not just one map. For a periodic orbit with period p and jumping index j satisfying equation

$$J_{(l+\mathsf{p})T'} = J_{lT'} + 2\pi\mathsf{j}, \tag{6.13}$$

where T' is an integer satisfying the equation $\delta_{n_p+T'} = \delta_{n_p}$, the average momentum is given by

$$m = -\frac{\eta\tau n_p}{\epsilon} + \left(\frac{2\pi j}{\mathsf{p}T'} - \frac{\sum_{s=0}^{T'-1}\delta_s}{T'}\right) n_p. \tag{6.14}$$

For $s_{n_p} = 1$, δ_s=0 and the mapping is identical to that of the primary resonances and the momentum transferred to a QAM is also identical to that of primary resonances. Even though it is interesting to explore the rich structure of the ϵ-classical theory, the discussion is limited to $s_{n_p} = 1$ in this chapter. Experimentally only the primary resonances were observed at higher order times. Thus, the discussion is further limited to $\mathsf{j} = 0$.

6.2.2 Rephasing theory of the higher order resonances

The rephasing theory was generalized for the first time for the higher order resonances discussed in this chapter . The appearance of a resonance for the kicking periods at rational fraction of the half-Talbot time suggests that the orders separated by b $\hbar G$ rephase for a resonance occuring at the kicking period of $(a/b)T_{1/2}$. Thus the difference in the phase evolution during the time between kicks for states $|m\rangle$ and $|m-b\rangle$ is an integer multiple of 2π. The phase evolution of a state $|m\rangle$ during the time between kicks is given by Eq. (2.33)

$$\Phi_m = \frac{\tau}{2}(m + \beta + \eta n_p + \eta/2)^2. \tag{6.15}$$

A state $|m-b\rangle$ during the same time acquires a phase of

$$\Phi_{m-b} = \frac{\tau}{2}(m - b + \beta + \eta n_p + \eta/2)^2. \tag{6.16}$$

The phase evolution between the two states $|m\rangle$ and $|m-b\rangle$ during the free evolution between n_p and $n_p + 1$ kicks is given by

$$\Phi_m - \Phi_{m-b} = \tau b(m + \eta n_p) + \tau b(\beta + \eta/2 - b/2). \tag{6.17}$$

The first term $\tau b(m + \eta n_p)$ in Eq. (6.17) changes with pulse number and the second term $\tau b(\beta+\eta/2-b/2)$ is constant. Thus the phases corresponding to these two terms evolve independently. Also at a resonance a/b, the phase evolution of the first term

is proportional to a. Thus setting the phase evolution to multiples of $2\pi a$,

$$\tau b(m_{\mathrm{QAM}} + \eta n_p) = 2\pi a m_{\mathrm{QAM}}, \tag{6.18}$$

and setting the second term of Eq. (6.17) to an integer multiple of 2π

$$\tau b(\beta_{\mathrm{QAM}} + \eta/2 - b/2) = 2\pi L', \tag{6.19}$$

where L' is an integer. Solving Eq. (6.18) for the order that participates in a QAM, and Eq. (6.19) for the initial momentum at which a QAM appears, we obtain

$$m_{\mathrm{QAM}} = -\frac{\eta\tau n_p}{\tau - 2\pi(a/b)} = -\frac{\eta\tau n_p}{\epsilon}, \tag{6.20}$$

and

$$\beta_{\mathrm{QAM}} = \frac{2\pi L'}{\tau b} + \frac{b}{2} - \frac{\eta}{2}. \tag{6.21}$$

Thus Eqs. (6.20) and (6.21) are generalizations of Eqs. (2.38) and (2.39) which can be obtained by setting $a = l$ and $b = 1$ (corresponding to the primary resonances). For kicking periods $T = (a/b)T_{1/2}$, the denominator of the first term in Eq. (6.21), i.e. τb, is $2\pi a$, and Eq. (6.21) becomes $\beta_{\mathrm{QAM}} = L'/a + b/2 - \eta/2$. Thus the resonances in the initial momentum are spaced by $\Delta\beta_{\mathrm{QAM}} = 1/a$.

6.3 Experimental Configuration

To experimentally observe these quantum resonances, the BEC was subjected to pulses of standing wave light similar to the experiments described in chapter 5. As before, the BEC was created in an optical trap and consisted of approximately 30000 Rb-87 atoms in the $F = 1$, $5S_{1/2}$ level. After release from the trap, the BEC was kicked by 780 nm light which was 6.8 GHz detuned to the red of the atomic transition. For this detuning and $\phi_d \sim 2$ (the maximum used in the experiments) the spontaneous emissions per pulse for each atom was negligible at about 1.8×10^{-3}. One major difference with the previous experiments was that this light propagated through

two acousto-optic modulators (AOMs) to control the initial momentum and the acceleration of the atoms with respect to the standing wave. This was accomplished by driving the two AOMs with different frequencies (detailed design is discussed in chapter 7). The kicking beam was oriented at 52° to the vertical. In order to vary the kicking strength ϕ_d, the length of the kicking pulses was adjusted. Typically the pulse length was approximately 1.8 μs giving $\phi_d \approx 1.5$. Although for pulse durations of ~ 2 μs, atoms in diffraction order $m = 10$ move a significant fraction ($\sim$0.6) of the standing wave, such a system can still be considered as a δ-kicked rotor (i.e. the diffraction is in the Raman-Nath regime) but with a reduced ϕ_d [47]. This is one of the factors which makes it difficult to observe high order resonances since they require a large value of ϕ_d to become visible (see the following discussion). The value of ϕ_d was estimated by comparing the relative population of various diffraction orders after one kick as detailed in chapter 5. Note that the population in the l-th order is given in terms of Bessel functions via $|J_l(\phi_d)|^2$ [45]. The momentum distribution of the BEC was measured by taking an absorption image ~ 8 ms after the completion of the kicking sequence. Finally it should be noted that the mean field energy was weak enough that it could be ignored, making the Hamiltonian of the δ-kicked accelerator a valid approximation.

6.4 Scans of kicking period

The main resonance occurring at $T = 2T_{1/2}$ was discussed in chapter 5. The observation of several higher order resonances is discussed in this section. Figures 6.1, 6.2, 6.3 and 6.4 show experimental scans of the kicking period across different higher order resonances. These figures were generated by horizontally stacking the absorption images each with a different kick period. The curves are the QAM momenta predicted by the theory of Eq. (6.20). It can be seen that the theory provides a good description of the momentum transfer to the QAM.

6.4.1 Resonance at $T = (1/3)T_{1/2}$

This resonance occurs at $T = 11.1$ μs ($a = 1$ and $b = 3$). Figure. 6.1 shows a scan of kicking period across 1/3 of the half-Talbot time. To generate this data, $\phi_d = 1.8$ was used. It was observed that an efficient QAM at this resonance could be produced for an acceleration $g' = 4.5$ ms^{-2}. Furthermore, a large number of kicks (30 kicks) was needed to produce the QAM near 1/3 of the half-Talbot time. The requirement of high ϕ_d is in accordance with the rephasing model since at this resonance, orders separated by 3 $\hbar G$ rephase.

6.4.2 Resonance at $T = (2/3)T_{1/2}$

This resonance was predicted to occur at the kicking period $T = 22.1$ μs. Thus a scan of kicking period across this resonance was performed. In the experiments, the HP 8770A arbitrary waveform synthesizer used for generating the kicking sequence had a resolution of 0.064 μs. Figure 6.2 shows the results of the experiment. The initial momentum was chosen in order to populate the mode above the resonance most efficiently. A high $\phi_d = 2$ was required to populate this resonance. At this ϕ_d, the atoms not participating in a QAM get diffracted into a wide range of orders that it made it difficult to resolve the mode from the atoms not in the QAM, especially for kicking periods far away from resonance ($T \sim 23$ μs). The orders separated by 3 $\hbar G$ rephase for this resonance.

6.4.3 Resonance at $T = (1/2)T_{1/2}$

This resonance occurs at the kicking period of $T = (1/2)T_{1/2} = 16.6$ μ s. Figure 6.3 shows the QAM and the fit to the theory of Eq. (6.20) taking $a = 1$ and $b = 2$. A value of $\phi_d = 1.4$ was sufficient to observe the mode, since the value of $\phi_d = 1.4$ populates three orders ($l = 0, -1$ and $+1$) equally for a single kick. Diffraction orders separated by $2\hbar G$ rephase in the QAM around this resonance.

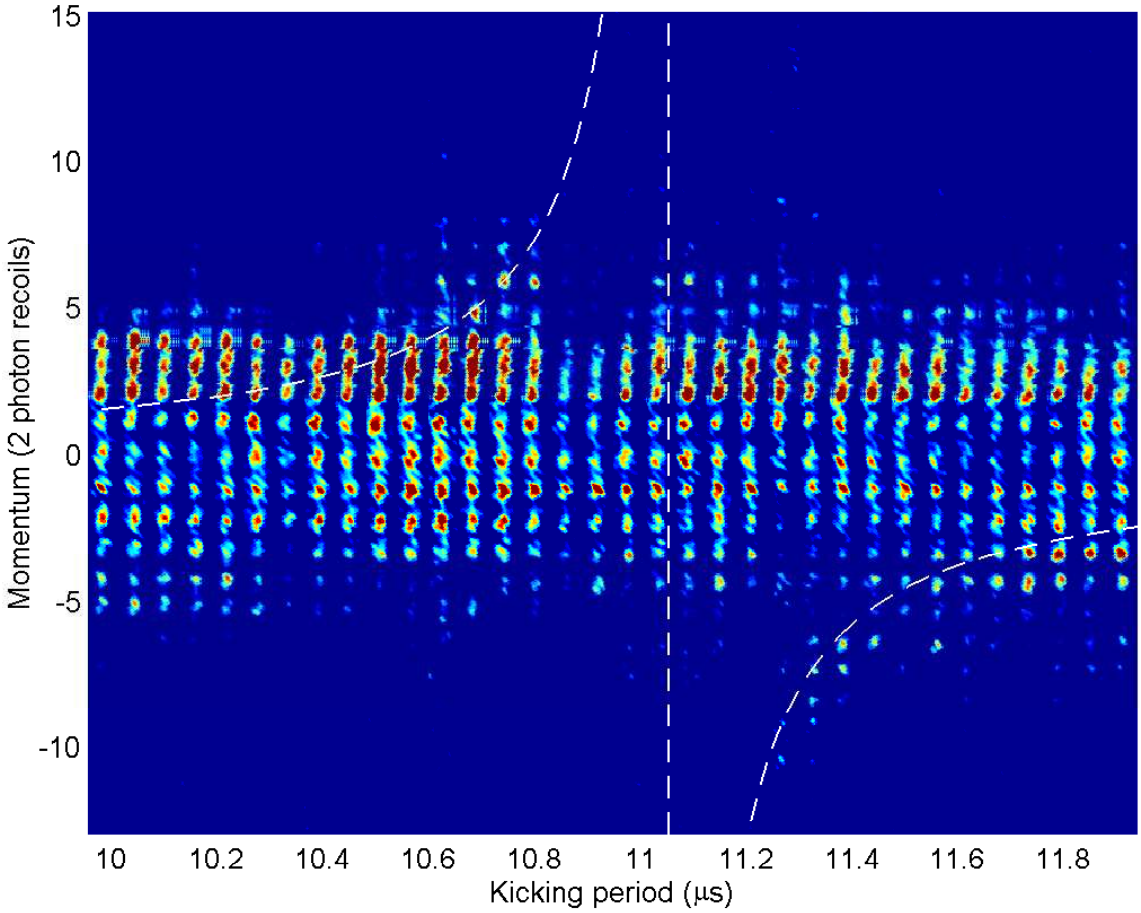

Figure 6.1: Horizontally stacked momentum distributions for different kicking periods for 30 kicks across $(1/3)T_{1/2}$ ($a = 1$ and $b = 3$), $g' = 4.5$ ms^{-2} and $\phi_d = 1.8$. The initial momentum was chosen such that the part of the mode above the resonance time is populated more strongly. The dashed curve is the theory in Eq. (6.20).

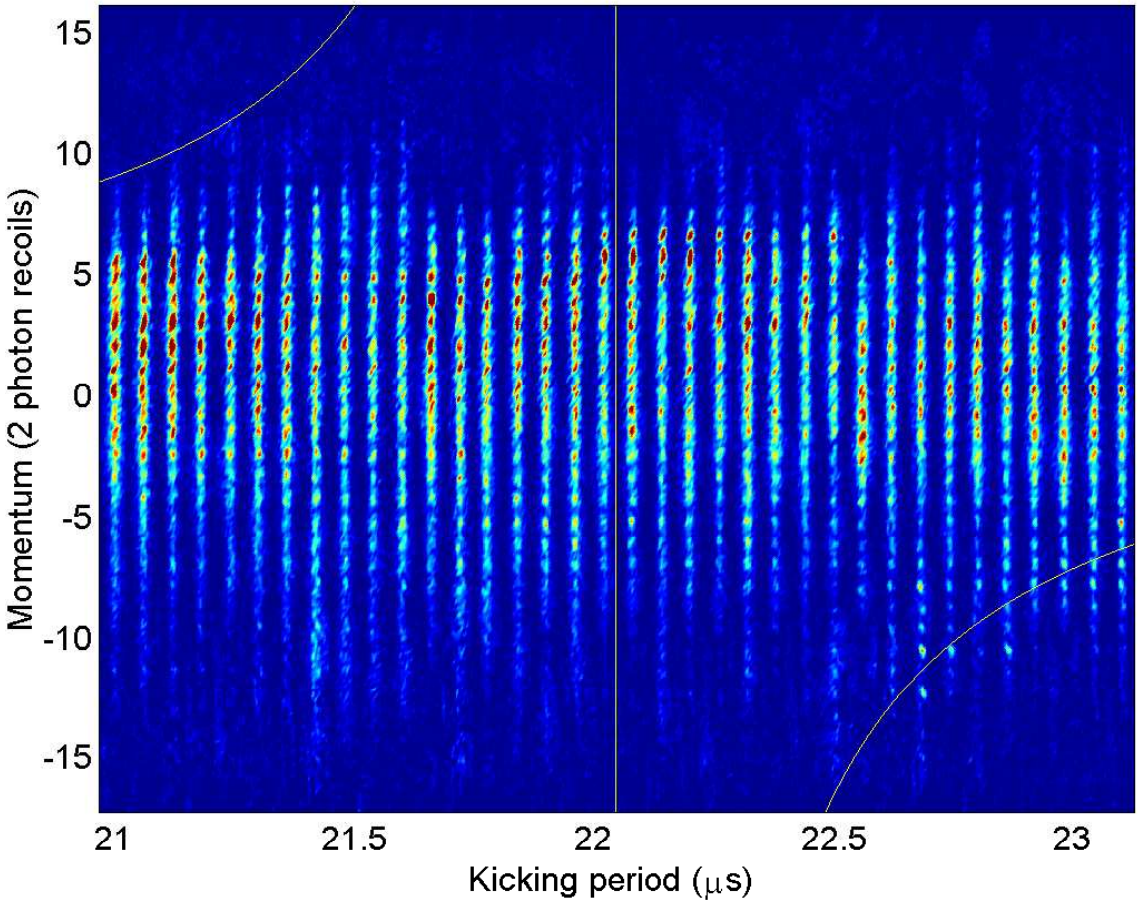

Figure 6.2: Horizontally stacked momentum distributions for kicking period across $T = (2/3)T_{1/2}$ ($a = 2$ and $b = 3$) for 30 kicks, effective acceleration of $g' = 6$ ms^{-2} and $\phi_d = 2$. The initial momentum was chosen such that the part of the mode above the resonance time was more strongly populated. The solid curve is that of the theory in Eq. (6.20).

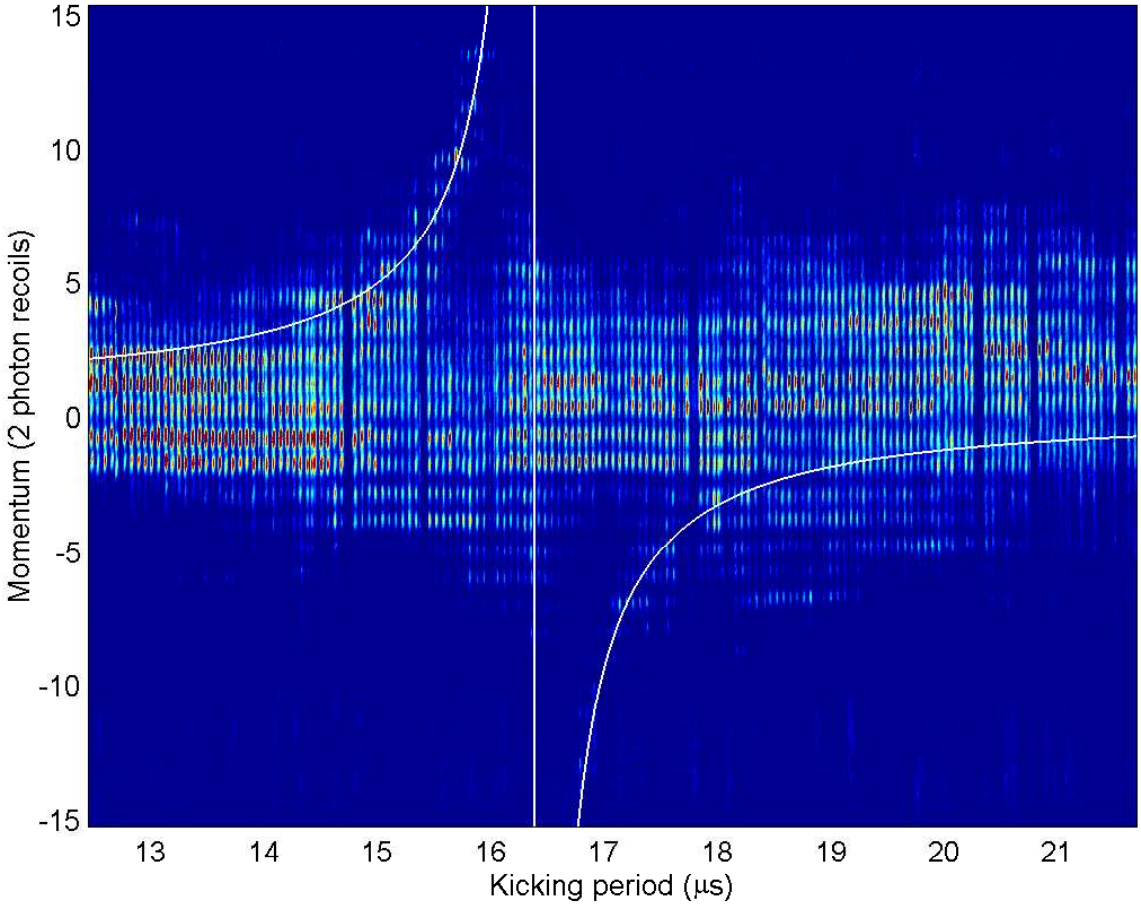

Figure 6.3: Horizontally stacked momentum distributions for different kicking periods after 40 kicks across $(1/2)T_{1/2}$ ($a = 1$ and $b = 2$) for the effective acceleration $g' = 6$ ms^{-2}, and $\phi_d = 1.4$. The initial momentum was chosen such that the part of the mode below the resonance time was more strongly populated. The solid curve is the result of the theory in Eq. (6.20).

6.4.4 Resonance at $T = (1/1)T_{1/2}$

For completeness a scan of kicking period around the half Talbot time $T_{1/2} = 33.2$ μs was performed. The result is displayed in Fig. 6.4. To generate this data a large $\phi_d = 2$ was used. As can be seen this populated more orders (5 orders) in the QAM than were observed in the data of Fig. (5.5). The initial momentum was chosen so that the component of the QAM appearing above the resonance time was populated most efficiently.

6.5 Kick scan near higher order resonances

To investigate the properties of the QAM near the higher order resonances further, a series of experiments where kick number was increased at a fixed kicking period close to a resonance were conducted. Three resonances $(2/3)T_{1/2}$, $(1/2)T_{1/2}$ and the resonance at Talbot time $(2/1)T_{1/2}$ were chosen since for these resonances $b = 3$, 2 and 1 respectively. These values of b were chosen because it is expected that rephasing occurs for orders separated by 3, 2, and 1 $\hbar G$ respectively. Figure 6.5(a) is a scan of number of kicks close to $(2/3)T_{1/2}$. This clearly shows that the QAM primarily consists of momentum states separated by $3\hbar G$ (indicated by horizontal arrows). The scan of kick number close to $(1/2)T_{1/2}$ of Fig. 6.5(b) shows much more clearly that the QAM is composed of momentum states separated by $2\hbar G$. These momentum states are again emphasized by horizontal arrows. In contrast, at the Talbot time $(2T_{1/2})$, the QAM includes neighboring momentum states as seen from Fig. 6.5(c). The right hand side of each of these figures shows a plot of the population vs. momentum at 33 kicks. Note again the separation of $b\hbar G$ between the momentum states participating in a QAM. This rephasing is analogous to what has been postulated to occur (but never directly observed) for the kicked rotor resonances [26], and is consistent with what is known of the fractional Talbot effect [109, 110].

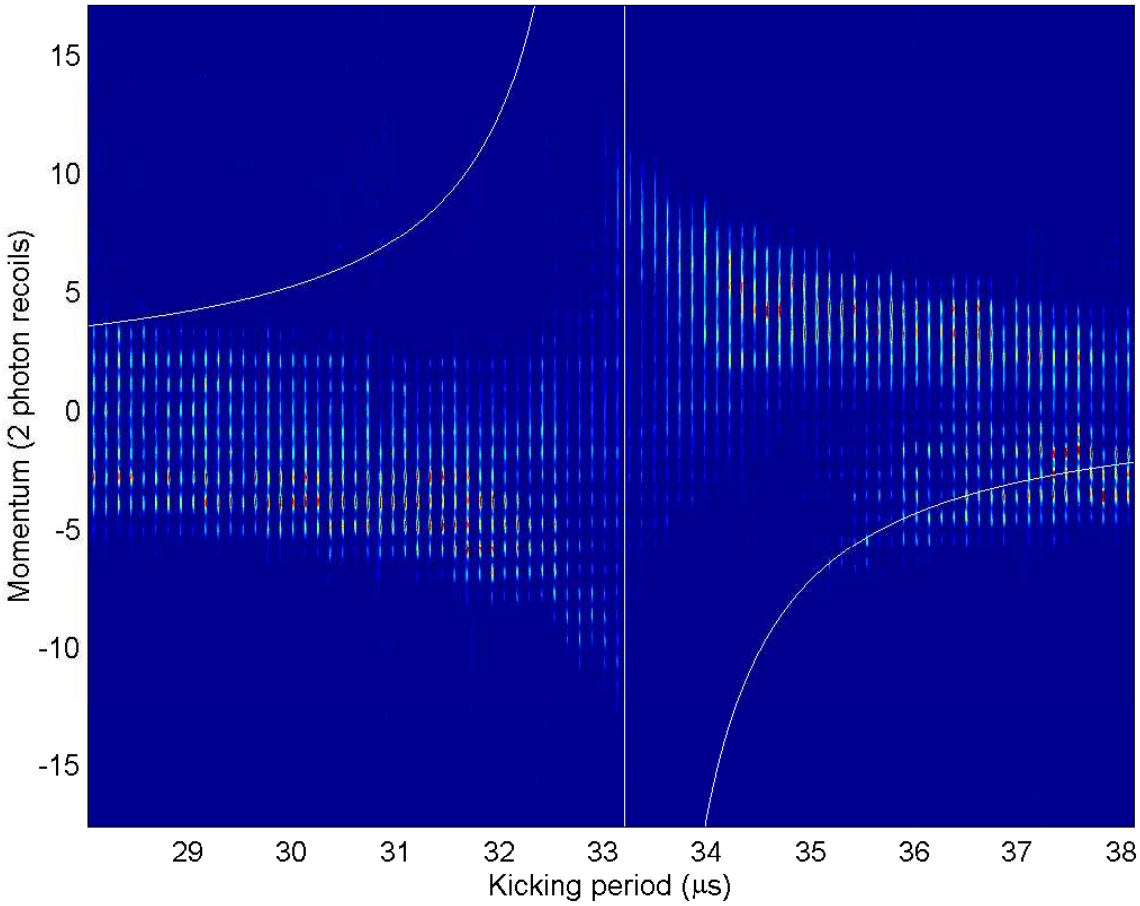

Figure 6.4: Horizontally stacked momentum distributions for different kicking periods across $(1/2)T_{1/2}$ ($a = 1$ and $b = 2$). The number of kicks was 15, the effective acceleration $g' = 6$ ms^{-2}, and $\phi_d = 2$. The initial momentum was chosen such that the part of the mode above the resonance time was more strongly populated. The solid curve is that of theory in Eq. (6.20).

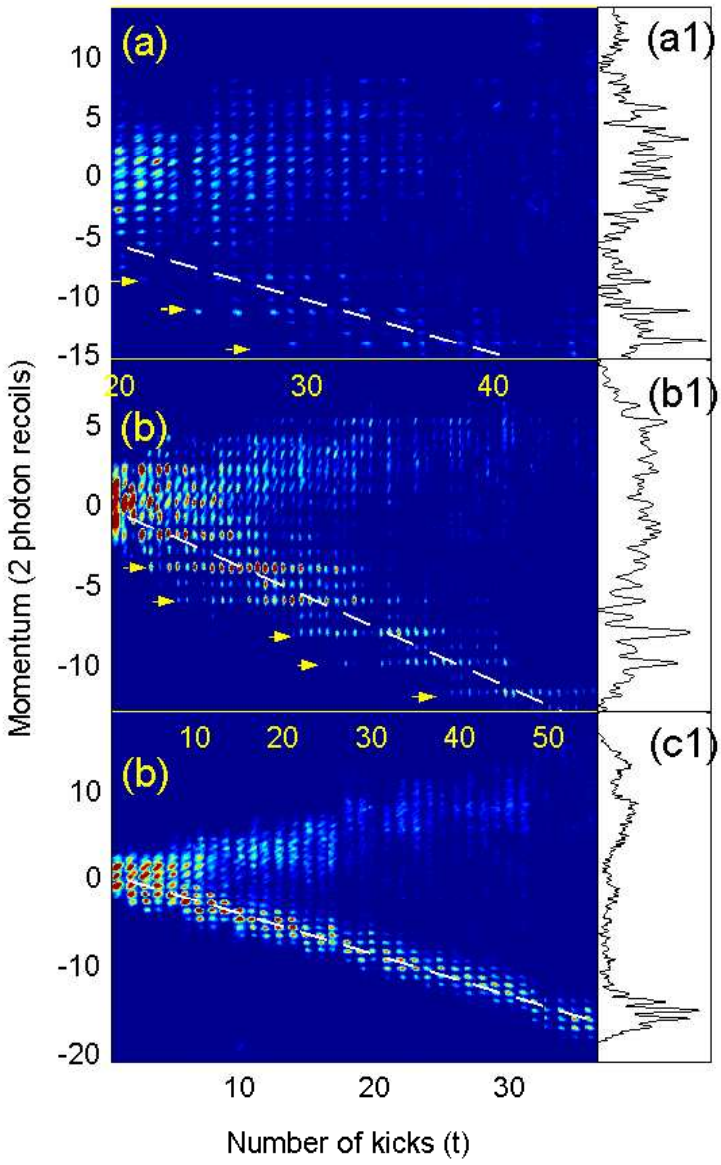

Figure 6.5: Horizontally stacked momentum distributions as a function of number of kicks (t) for (a) $T = 22.68$ μs, which is close to $(2/3)T_{1/2}$, (b) $T = 17.1$ μs, which is close to $(1/2)T_{1/2}$, and (c) $T = 72.4$ μs which is close to $2T_{1/2}$. Note the different axes for (a), (b) and (c). The horizontal arrows in (a) and (b) show that primarily orders separated by $b\hbar G$ participate in each of the QAMs. Dashed lines show the position of the QAM predicted by the theory of Eq. (6.20). The end panels show the momentum distribution for 33 kicks. A value of $g' = 6$ ms^{-2} was used for these experiments.

In the experiments, different values of ϕ_d were used to observe each higher order resonance. Since the range of momentum orders populated by a single kick is approximately proportional to ϕ_d, ϕ_d must be increased at the higher order resonances so that a single kick can diffract into a range of states comparable to $b\hbar G$ (the separation between the states participating in the QAM). Recall that the population of a momentum state $l\hbar G$ is proportional to $|J_l(\phi_d)|^2$ after a single Raman-Nath diffraction, with the highest population occurring in the state $l \sim \phi_d$. Paradoxically the high ϕ_d needed at these large b resonances can also make it difficult to observe QAMs. Since the distribution of momentum states that do not participate in a QAM broadens. This can mask the presence of a QAM in either a scan of kick period or kick number especially in the case of experiments with only a few kicks.

6.6 Phase Space maps

The rephasing model predicts that the QAMs in the δ-kicked accelerator are spaced in initial momentum by $\Delta p_i = 2\pi/\tau b \approx 1/a$. This means that the islands in the phase space map (which are attributed to the existence of the QAMs [76, 77]) shown in Fig. 6.6 are separated in momentum by $\hbar G/a$ [76]. Figure 6.6 shows these phase space islands close to $(1/2)T_{1/2}$ in Fig. 6.6(a) and $(2/3)T_{1/2}$ in Fig. 6.6(b). The momentum axes in these maps cover a range of $1\hbar G$. Thus to resolve the structures in phase-space within a unit cell and test the theory of Eq. (6.21), it is necessary that the momentum width should be much narrower than $\hbar G/a$. In our experiments the BEC had a momentum width of 0.056 $\hbar G$ [105] which makes it an excellent candidate for this task. The size of the BEC in momentum is shown in Fig. 6.6(b) with two dashed lines. In the θ direction, BEC covers many unit cells.

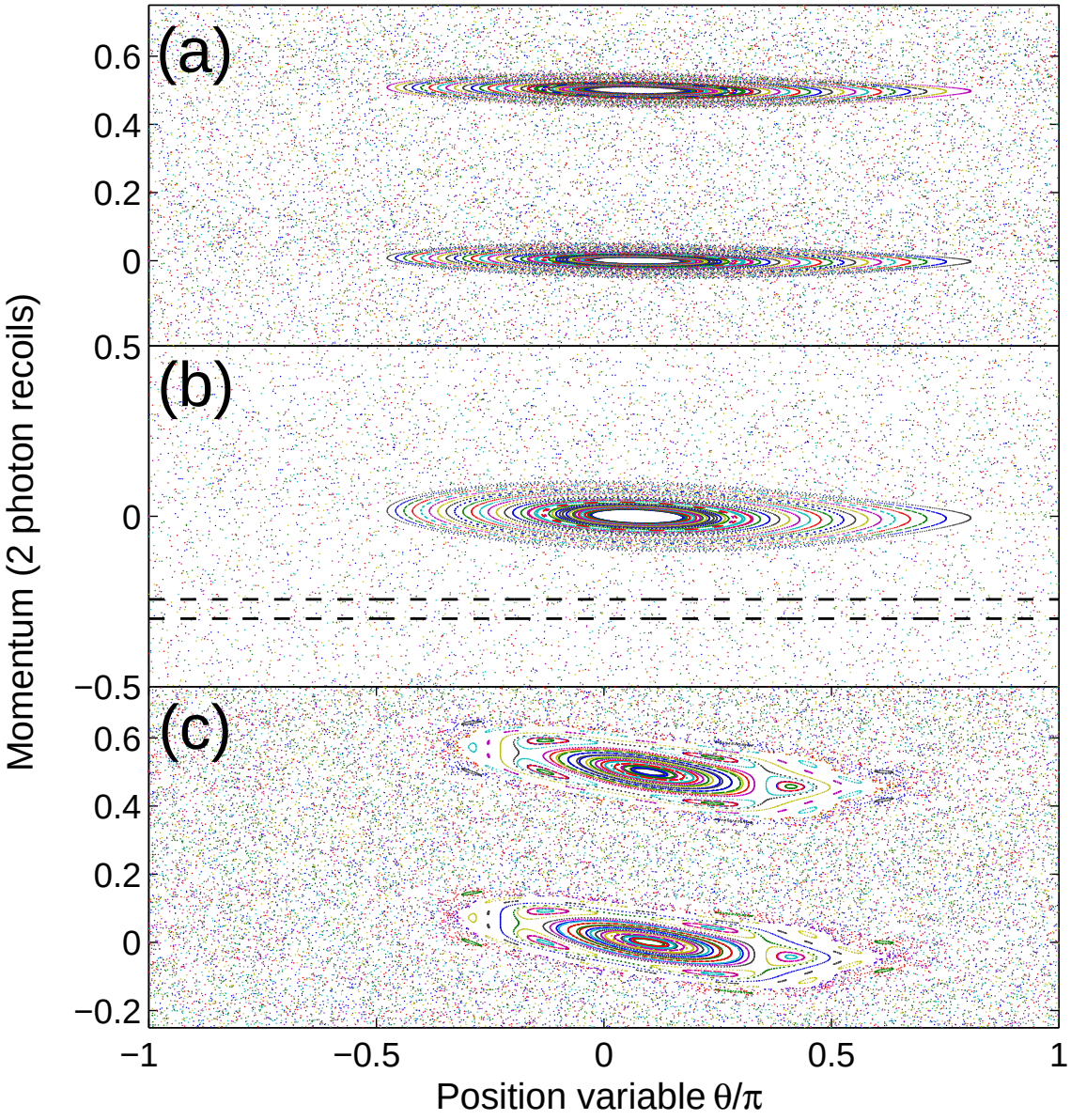

Figure 6.6: Phase space plot of the map in Eq. (6.12) for (a) $\phi_d = 1.5$, $g' = 6$ ms^{-2} and $T = 17.1$ μs, which is close to (1/2) $T_{1/2}$, (b) $\phi_d = 1.8$, $g' = 4.5$ ms^{-2} and $T = 22.68$ μs which is close to (2/3) $T_{1/2}$ and (c) $\phi_d = 1.4$, $g' = 6$ ms^{-2} and $T = 61$ μs which is close to the Talbot time ($2T_{1/2}$). When a wave packet is trapped in an island, a QAM is formed [76]. The dashed lines in (b) show the width of the BEC.

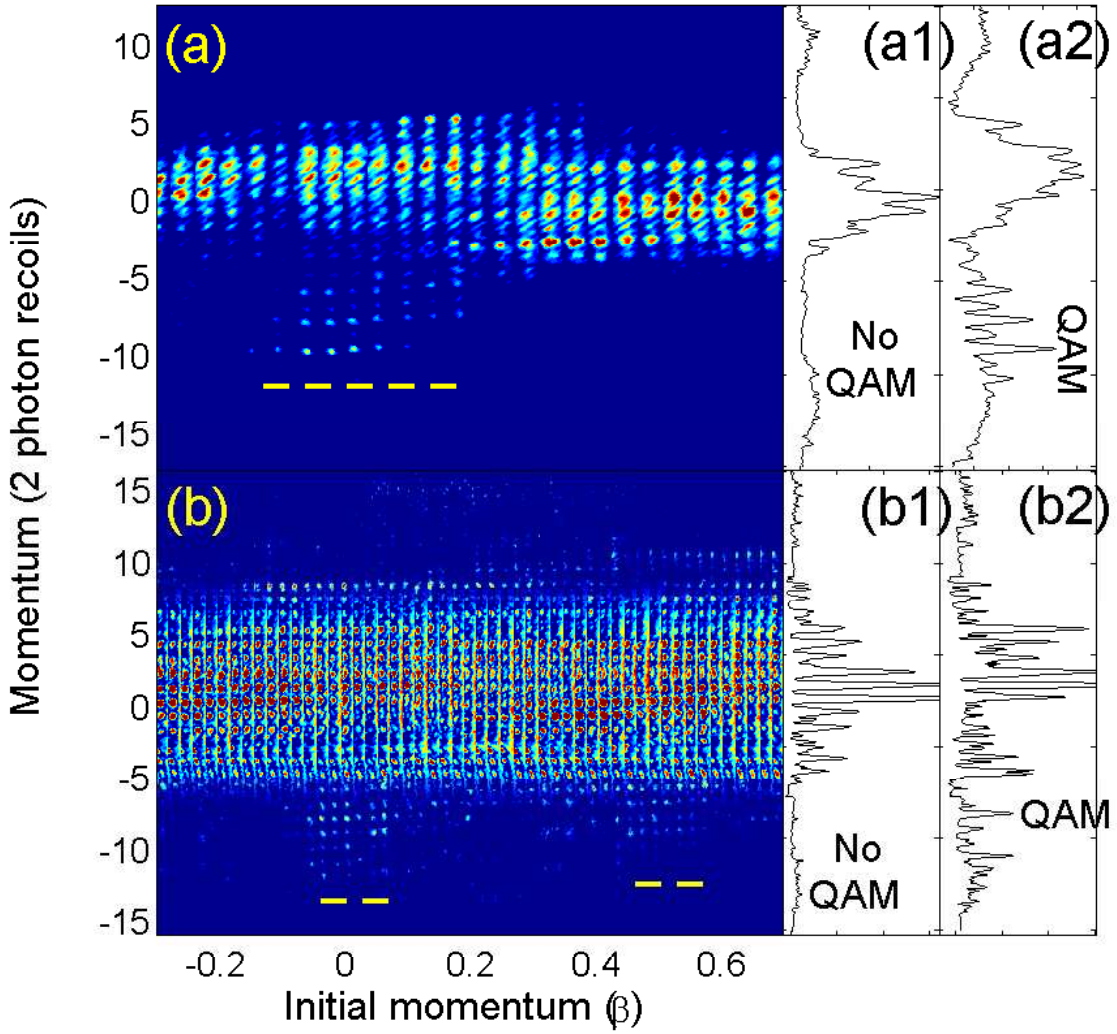

Figure 6.7: Horizontally stacked momentum distributions as a function of the initial momentum of the BEC before kicking. (a) 30 kicks with a period of 17.1 μs (close to $(1/2)T_{1/2}$, $a = 1$), and $g' = 6$ ms^{-2} (b) 40 kicks with the period of 22.53 μs (close to $(2/3)T_{1/2}$, $a = 2$), and $g' = 4.5$ ms^{-2}. The position of the modes are indicated by the dashed lines. The panels (a1) and (b1) show the final momentum distribution for initial momenta at which a QAM does not appear. Panels (a2) and (b2) correspond to initial momenta at which a QAM is seen. The range of initial momentum over which the QAMs is shown as double arrows in (a2) and (b2)

6.7 Scan of initial momentum

Figure 6.7 shows the results from experiments in which the effective initial momentum of the BEC was changed by moving the standing wave using a difference in frequency between the kicking AOMs. This is equivalent to taking the strip shown between the dashed lines in Fig. 6.6(b) and scanning it through the unit cell. The kicking period was near $(1/2)T_{1/2}$ in Fig. 6.7(a) and $(2/3)T_{1/2}$ in Fig. 6.7(b). To improve clarity, the initial momentum was scanned over a range of $-0.3\ \hbar G$ to $0.7\ \hbar G$. This range was chosen since the QAMs appear at $p_i = 0$ in both cases. During a scan over such an interval of initial momentum, the QAM appears once at $(1/2)T_{1/2}$ and twice at $(2/3)T_{1/2}$. This demonstrates that the initial momenta at which the modes can exist are separated by $\hbar G$ in the case of $(1/2)T_{1/2}$ ($a = 1$) and $\hbar G/2$ for $(2/3)T_{1/2}$ ($a = 2$) in agreement with Eq. (6.21).

6.8 Conclusion

The existence of higher order resonances in the quantum δ-kicked accelerator has been experimentally demonstrated. This was possible through the observation of QAMs near these resonances. The ϵ-classical theory of FGR was generalized to predict the behavior of the system near the higher order resonances. The narrow momentum distribution of the BEC enabled the observation of the momentum state structure of the QAMs and it was found that QAMs near higher order resonances have a structure which is reminiscent of that produced by the fractional Talbot effect. Furthermore, it was possible to explore the phase space structures produced by maps of the generalized theory. This work opens the door towards the study of higher order QAMs near higher order resonances. Other interesting questions include the effect of stronger mean field interactions [114], the enhancement of QAMs using more complex initial states, and the effect of finite pulse length.

CHAPTER 7

Quantum Ratchet using a kicked BEC

7.1 Introduction

A ratchet is a process of extracting a flow of particles in a well defined direction from a diffusive process without net bias. A key requirement for producing the net flow is an asymmetry between a time periodic potential and the distribution of particles. The first experiment to realize a ratchet was performed using Brownian particles subjected to time periodic saw tooth potential. Diffusion of particles played a critical role in the case of this classical ratchet [115, 116]. The mechanism in these experiments is illustrated in Fig. 7.1. When a potential, as shown in Fig. 7.1 is turned on, particles are trapped at the minima of the potential. When the potential is switched off, the distribution diffuses uniformly. When the potential is turned on again all the particles within the vertical lines shown in the figure are trapped again at the minima of the well. If the potential is symmetric with respect to the distribution as shown in Fig. 7.1(a), there is no net motion of the particles. If there is an asymmetry in the potential with respect to the distribution as shown in Fig. 7.1(b), when the potential is switched on the second time, part of the cloud that has expanded is trapped in the well that is to the left of the cloud. If this pulsing of the potential continues, there is a net flow of particles to the left. These so called Brownian motors have attracted much attention recently [117]. Interesting applications of this classical ratchet are a flow of current without any bias voltage in metals [118] and certain biological motors [119, 120, 121]. A good review of Brownian motors is given in an article in Physics Today [122].

An atom optics system is used in this chapter to realize a quantum ratchet. J. Gong and coworkers investigated theoretically a quantum ratchet using kicked systems [123, 124] such as the kicked Harper model. Here in this chapter the quantum δ-kicked rotor model is used. Thus the δ-kicked rotor is described in section 7.2. The classical evolution can be described using a map called the standard map. A Floquet operator is used to understand the quantum evolution and derive an expression for the mean momentum. In section 7.3 the theory of quantum ratchet investigated in this thesis is discussed. Details of the experimental configuration are presented in section 7.4 and in section 7.5, the experimental results are described. Finally, section 7.6 is devoted to conclusions of the chapter. This work was published in an article in Physical Review Letters [105].

7.2 The δ-kicked rotor

An atom optics version of the quantum δ-kicked rotor can be realized by subjecting the cold atoms to standing wave pulses of off-resonant light [12, 26, 46, 125]. Since the atoms experience a spatially periodic potential, it can be described as a kicked rotor as described in chapter 2. The time asymptotic dynamics such as dynamical localization and quantum resonances have played an important role in studying chaos in quantum world. Quantum resonance results when the pulsing period is a rational fraction of a time called the half-Talbot time. This phenomena is analogous to the Talbot effect in optics. For other pulse periods, quantum suppression of diffusion occurs. This is called the dynamical localization. The δ-kicked rotor can be described by a Hamiltonian (in dimensionless units) similar to the kicked accelerator but with the acceleration η set to zero. That is,

$$\mathcal{H} = \frac{P^2}{2} + \phi_d \cos(X - \gamma) \sum_n \delta(t - n\tau), \tag{7.1}$$

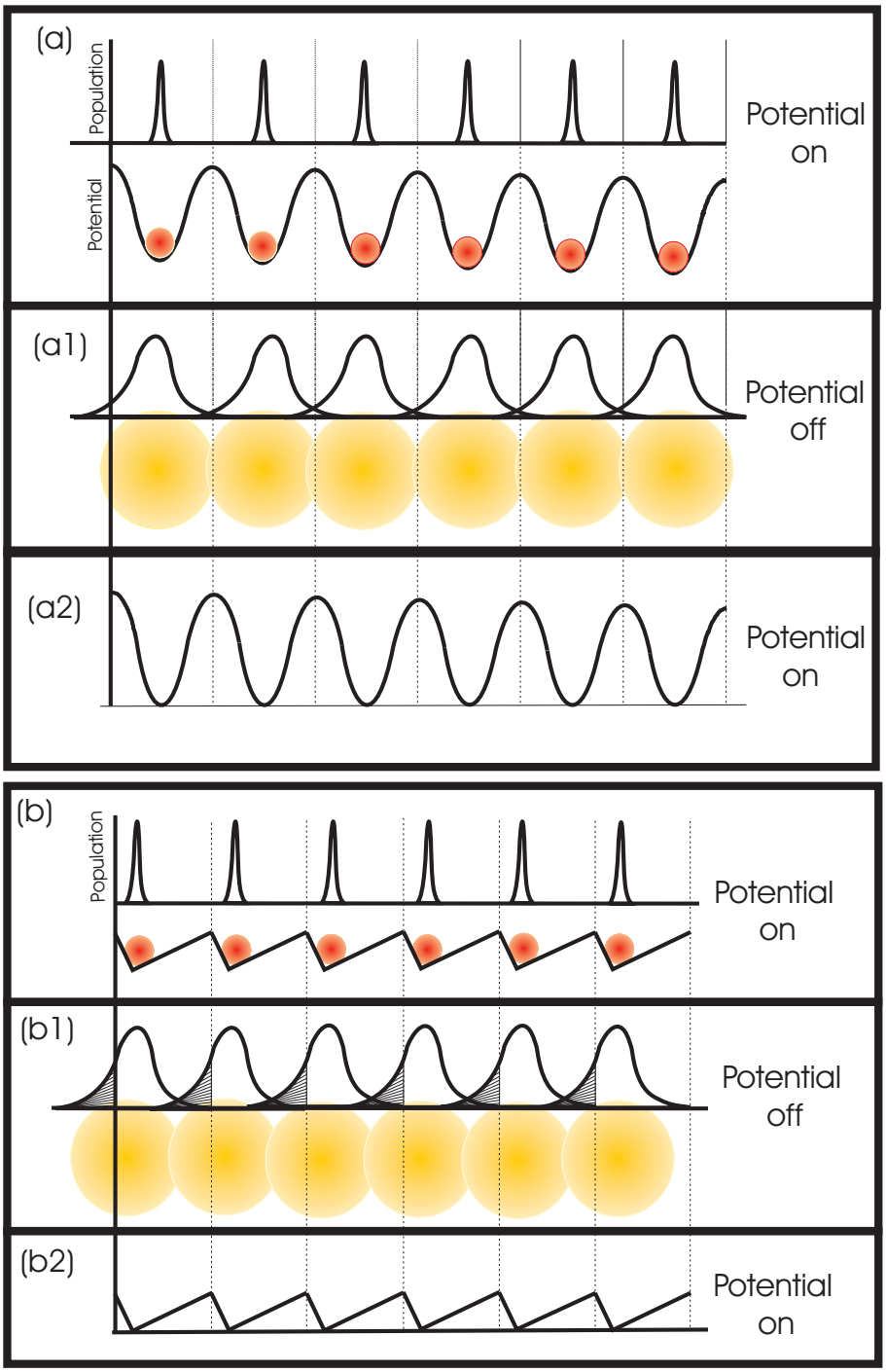

Figure 7.1: A ratchet resulting from asymmetry between the potential and the initial distribution. (a) the potential and the distribution have a symmetry and (b) The potential is not symmetric with respect to the distribution resulting in a net flow to the left

where the parameter γ is a constant phase of the potential. This parameter plays an important role in the quantum ratchet described later in this chapter

7.2.1 Classical Evolution

Starting from Hamilton's equations of motion for the Hamiltonian of Eq. (7.1) and following the procedure used for the case of the classical evolution of the δ-kicked accelerator described in section 2.3, the classical evolution of the kicked rotor results in the mapping given by

$$\begin{aligned} x_{n+1} &= x_n + \tau p_{n+1} \\ p_{n+1} &= p_n + \phi_d \sin(x_n - \gamma). \end{aligned} \tag{7.2}$$

Defining new variables $\tau p = p'$, and $\tilde{k'} = \tau\phi_d$, Eq. (7.2) becomes,

$$\begin{aligned} x_{n+1} &= x_n + p'_{n+1} \\ p'_{n+1} &= p'_n + \tilde{k'} \sin(x_n - \gamma). \end{aligned} \tag{7.3}$$

This mapping is called the standard mapping. Figure 7.2 shows a stroboscopic picture of p' vs. x of Eq. (7.3) for $\gamma = 0$ and various values of $\tilde{k'}$. It can be seen that as the kicking strength $\tilde{k'}$ increases, the chaotic region becomes more pronounced. At the value of $\tilde{k'} = 7$, there is no regular region (the elliptical orbits) in the maps.

7.2.2 Quantum evolution

In the Raman-Nath regime, the quantum evolution can be obtained from the repeated application of the one kick Floquet operator:

$$\hat{U}_R = \hat{F}_R \hat{R}_R = \mathrm{e}^{-i\phi_d \cos(\hat{X} - \gamma)} \mathrm{e}^{-i\tau \hat{P}^2/2}, \tag{7.4}$$

where $\hat{F}_R$ describes the evolution operator during kicking and $\hat{R}_R$ describes the free evolution between the kicks. The operator $\hat{U}_R$ commutes with spacial translations

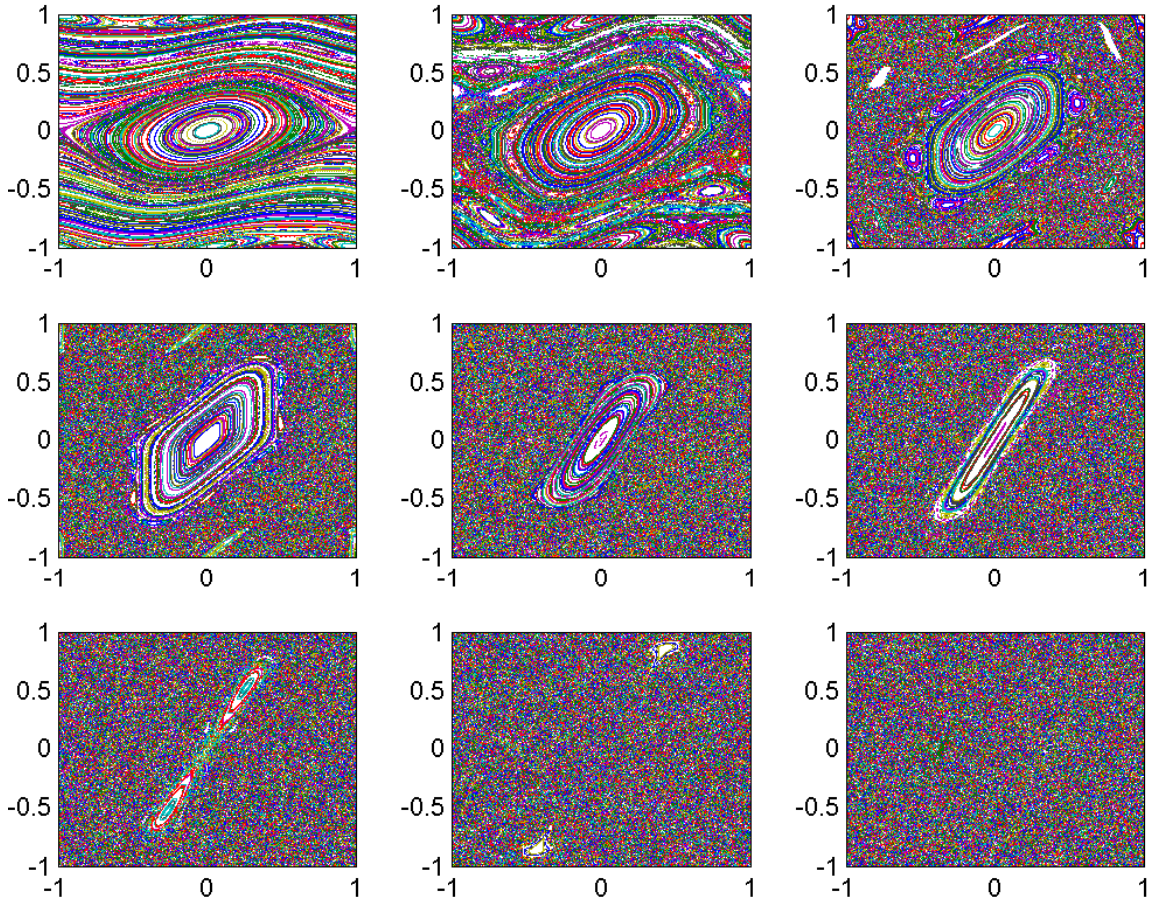

Figure 7.2: Phase space maps of Eq. 7.2 for $\gamma = 0$ and (a) $\tilde{k}' = 0.5$ where only the regular regions are seen, (b) $\tilde{k}' = 1$ where a small chaotic region develops around the central island, (c)$\tilde{k}' = 1.5$, (d) $\tilde{k}' = 2$, (e) $\tilde{k}' = 3$, (f) $\tilde{k}' = 4$ where the island becomes elongated, (g) $\tilde{k}' = 4.5$ where period 2 fixed point starts to visible, (h) $\tilde{k}' = 5.5$, and (i) $\tilde{k}' = 7$ where the whole phase space is chaotic.

by 2π. Hence Bloch theory requires that the quasi-momentum (initial momentum modulo 1) is conserved. Following the same construction as in section 2.4.4 and writing $P = N + \beta$, where $0 \leq |\beta| \leq 1$), N is an integer and $\theta = x \bmod 2\pi$, the evolution operator becomes

$$\hat{U_R} = \hat{F}_R \hat{R}_R = \mathrm{e}^{-i\phi_d \cos(\hat{\theta}-\gamma)} \mathrm{e}^{-i\frac{\tau}{2}(\hat{N}+\beta)^2} \tag{7.5}$$

Following the procedure described in section 2.4.3, the matrix elements of the operators $\hat{F}_R$ and $\hat{R}_R$ can be evaluated

$$\langle n|\hat{F}_R|m\rangle = (-i)^{m-n} J_{m-n}(\phi_d) \mathrm{e}^{i(m-n)\gamma}, \tag{7.6}$$

$$\langle n|\hat{R}_R|m\rangle = \langle n|\mathrm{e}^{-i(\tau/2)(\hat{N}+\beta)^2}|m\rangle = \delta_{nm} \mathrm{e}^{-i(\tau/2)(n+\beta)^2}. \tag{7.7}$$

These equations can also be obtained by setting $\eta = 0$ in the quantum evolution of the kicked accelerator of Eqs. (2.30) and (2.31).

7.2.3 The resonances

The quantum δ-kicked rotor exhibits a phenomenon known as quantum resonance. Quantum resonance results when the evolution operator is invariant in translations in momentum by an integer b, ($\hat{T}_b = \mathrm{e}^{-ib\hat{\theta}}$). Thus $\left[\hat{T}_b, \hat{U}_R\right] = 0$ for a resonance. Evaluating $\left[\hat{T}_b, \hat{U}_R\right]$, we obtain,

$$[\hat{T}_b, \hat{U}_R]\psi(\theta) = \mathrm{e}^{-i\phi_d \cos(\hat{\theta}-\gamma)} \left(\mathrm{e}^{-ib\hat{\theta}} \mathrm{e}^{-i\frac{\tau}{2}(\hat{N}+\beta)^2} - \mathrm{e}^{-i\frac{\tau}{2}(\hat{N}+\beta)^2} \mathrm{e}^{-ib\hat{\theta}}\right) \psi(\theta). \tag{7.8}$$

Using the relations

$$\begin{aligned} \mathrm{e}^{-i\frac{\tau}{2}\hat{N}^2} \left(\mathrm{e}^{-ib\hat{\theta}}\psi(\theta)\right) &= \mathrm{e}^{-ib\hat{\theta}} \mathrm{e}^{-i\frac{\tau}{2}(\hat{N}-b)^2} \psi(\theta), \\ \mathrm{e}^{i\theta_0 \hat{N}} \psi(\theta) &= \psi(\theta + \theta_0) \end{aligned}$$

(where the definition of $\hat{N} = -i\frac{\mathrm{d}}{\mathrm{d}\theta}$ is used and the second of these relations is the translations in position), Eq. (7.8) becomes,

$$\begin{aligned} [\hat{T}_b, \hat{U}_R]\psi(\theta) &= \mathrm{e}^{-i\phi_d \cos(\hat{\theta}-\gamma)} \mathrm{e}^{-ib\theta} \\ &\quad \left(\mathrm{e}^{-i\frac{\tau}{2}\hat{N}^2} \psi(\theta - \tau\beta) - \mathrm{e}^{ib\tau(\beta - b/2)} \mathrm{e}^{-i\frac{\tau}{2}\hat{N}^2} \psi(\theta - \tau\beta + \tau b)\right). \end{aligned} \tag{7.9}$$

Vanishing of this commutator requires that

$$\begin{aligned} \tau b &= 2\pi a, \text{ and} \\ b\tau(\beta - b/2) &= \pm 2\pi r, \end{aligned} \tag{7.10}$$

where a and r are any integers. Thus the resonance occurs whenever $\tau = 2\pi a/b$ (τ is a rational fraction of 2π) and the quasimomentum $\beta = b/2 \pm r/a$. For $b \geq 2$, the resonances are said to be high order resonances (these have been discussed for kicked accelerator in detail in chapter 6. Several of these resonances for the kicked rotor have been recently observed experimentally by William D Phillips and coworkers [27].

7.2.4 Rephasing model

The rephasing model that was successfully applied for the case of the δ-kicked accelerator can be used to get an intuitive understanding of the resonant behavior in the quantum δ-kicked rotor. In this picture, resonances result when the momentum states separated by $b\hbar G$ rephase (evolve an integer multiple of 2π in phase difference).

Following the procedure discussed in section 6.2.2, the difference in phase acquired by states $|m\rangle$ and $|m-b\rangle$ during the time between the kicks is given by,

$$\Phi_m - \Phi_{m-b} = \tau m b + \tau b(\beta - b/2). \tag{7.11}$$

The two terms in Eq. (7.11) evolve independently. Thus for resonances

$$\tau m b = 2\pi a m, \text{ and} \tag{7.12}$$

$$\tau b(\beta - b/2) = \pm 2\pi r. \tag{7.13}$$

Equation (7.12) results in the resonance condition that $\tau = 2\pi a/b$ (or the kicking period $T = (a/b)T_{1/2}$) and Eq. (7.13) shows the condition on the initial momentum for a resonance at $T = (a/b)T_{1/2}$. The resonances of the kicked rotor are shown in Figs. 7.3 and 7.10. A value of $\phi_d = 2.5$ was used at the half-Talbot time for $\beta = 0.5$ in

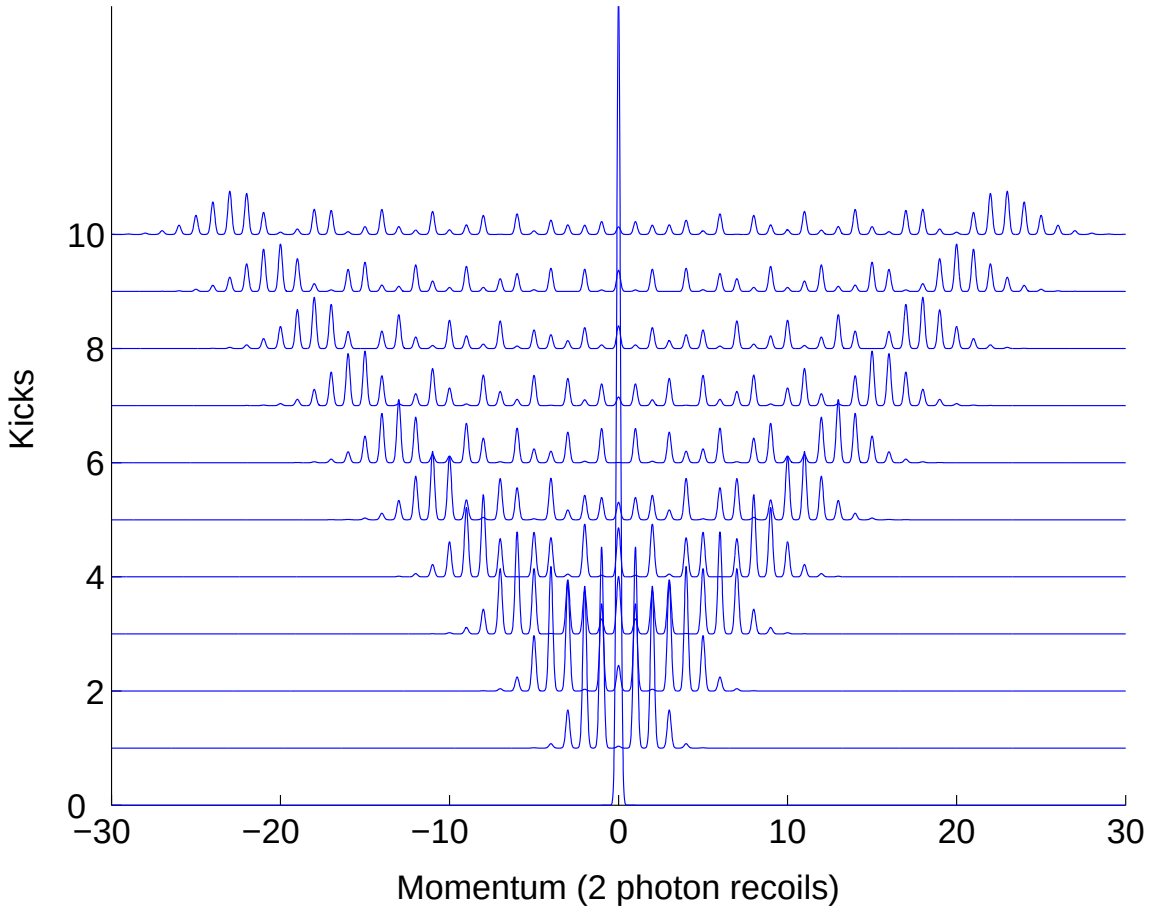

Figure 7.3: Numerical simulation results of a resonance of the quantum δ-kicked rotor. A value of ϕ_d of 2.5 and β of 0.5 were used at $T = T_{1/2}$. The QAM moves out symmetrically on either side.

Fig. 7.3, which shows a numerical simulation result of a scan of kicks at the resonance $T = T_{1/2}$. The experimental data of Fig. 7.4 shows a scan of initial momentum for the kicked rotor. The data indicates that the resonance occurs at $\beta = 0.5$.

7.2.5 Quantum Anti Resonance

For the half-Talbot time, Eq. (7.13) predicts that a resonance occurs for the initial momentum $\beta = 1/2$. For $\beta = 0$, Eq. (7.13) predicts that an order m at the half-Talbot time acquires a phase $\exp(-i\pi m^2) = \exp(-i\pi m)$. Thus the odd orders acquire a phase of π and even orders acquire 2π. This pattern of phase shifts in the orders means that the wavefunction after an evolution of $T_{1/2}$ looks like the wavefunction directly after the kick with a translation of π in the θ direction. Thus in a series of two kicks, the effect of the first kick is canceled by the second kick resulting in the original wavefunction. This can be seen in the numerical simulation results presented in Fig. 7.5. This phenomena has been termed quantum anti-resonance.

If the kicking period is not a rational fraction of the half-Talbot time, the phases of the orders randomize as the kicks are increased. This situation results in a process known as dynamical localization, which was first studied in atom optics by Mark Raizen [12], and is analogous to Anderson localization in a disordered lattice.

Thus a kicked rotor shows the phenomena of quantum resonance, quantum anti-resonance and the dynamical localization. In this chapter, quantum resonances are utilized to realize the quantum ratchet mechanism.

7.2.6 Evolution of a state $\psi_0(\theta)$ at resonance

In this section, the discussion is limited to the primary resonances which occur when $b = 1$. For these resonances ($\tau = 2\pi a$) and using the fact that for an integer n, $\mathrm{e}^{-i\pi n^2} = \mathrm{e}^{-i\pi n}$, the evolution operator becomes,

$$\hat{U}_R = \mathrm{e}^{-i\pi a\beta^2}\mathrm{e}^{-i\phi_d\cos(\hat{\theta}-\gamma)}\mathrm{e}^{-i\pi a(2\beta+1)\hat{N}} \tag{7.14}$$

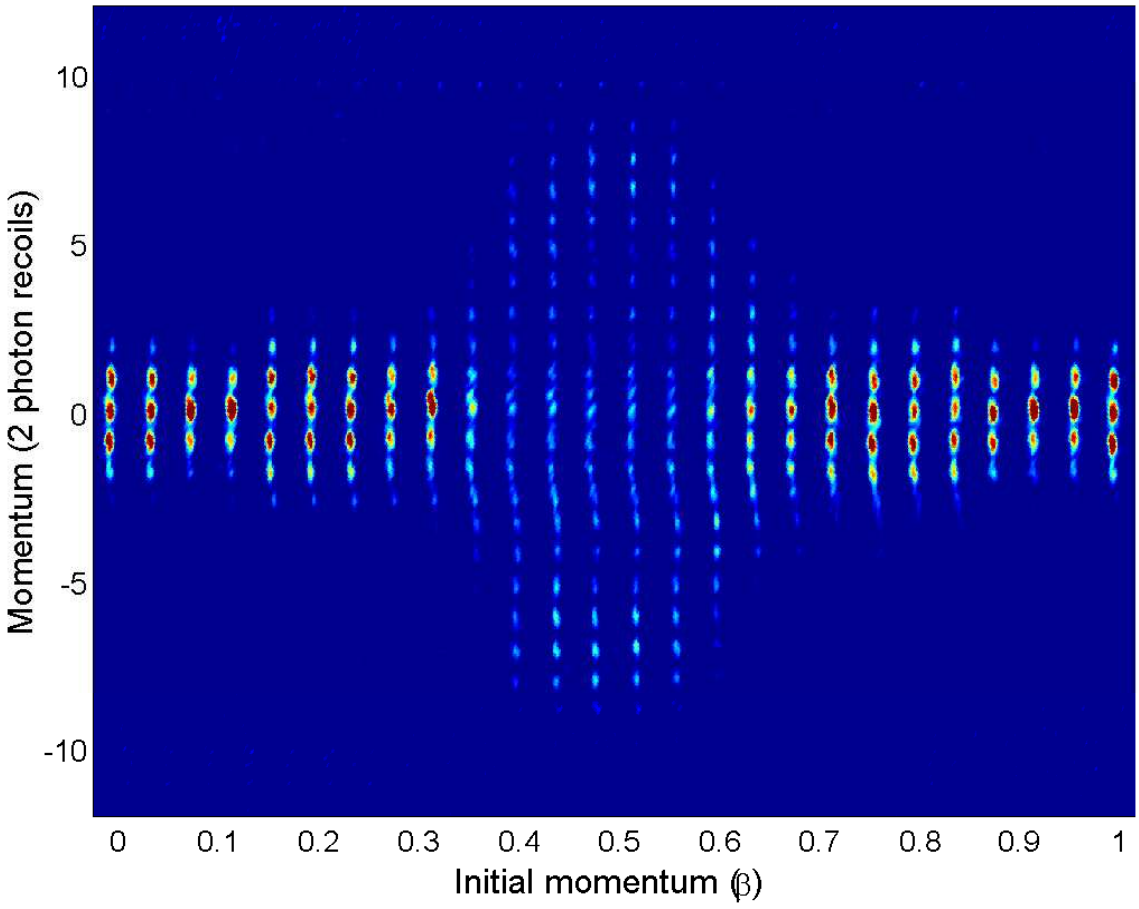

Figure 7.4: Experimental data of a scan of initial momentum of the quantum δ-kicked rotor. It can be seen that at the resonance momentum of $\beta = 0.5$, more momentum orders are populated. The parameters used are $\phi_d = 1.4$, $T = T_{1/2} = 33.152$ μs and kicks $n_p = 5$.

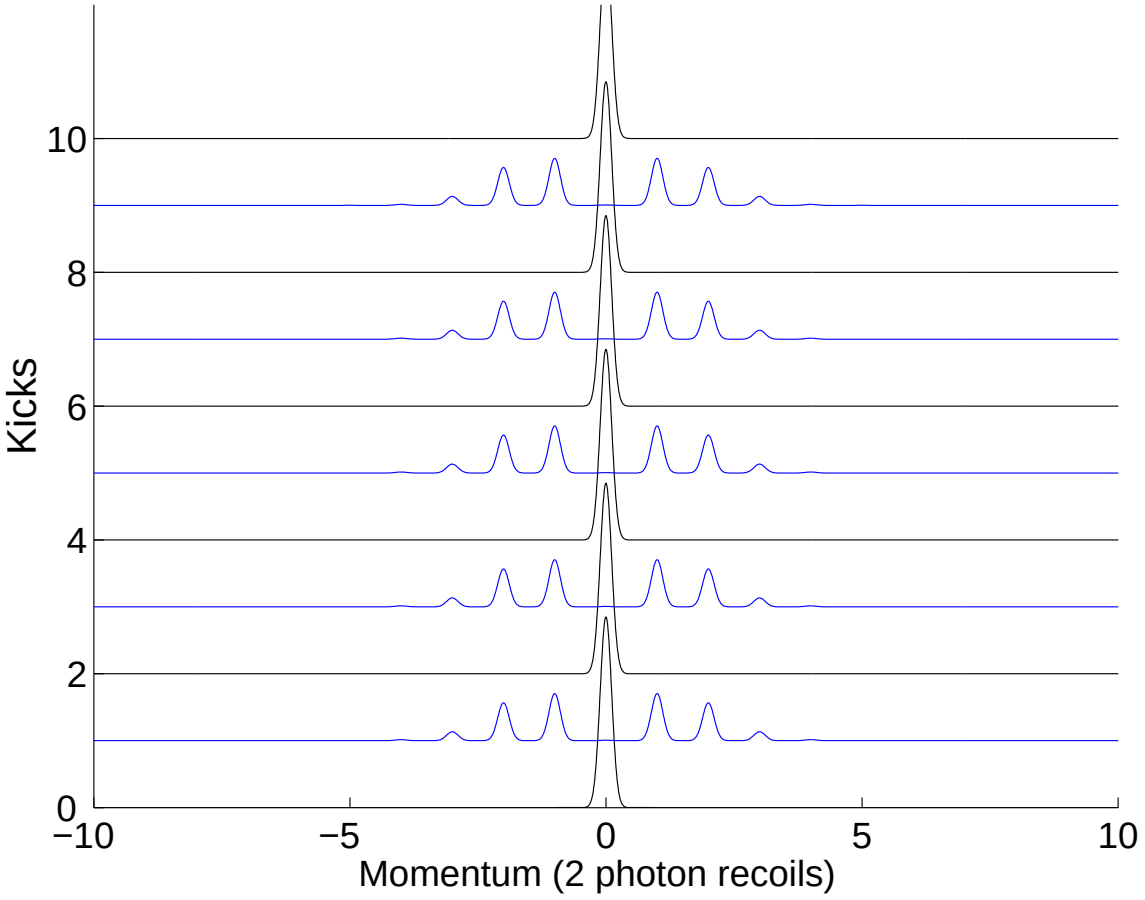

Figure 7.5: Numerical simulation of the quantum anti-resonance of the quantum δ-kicked rotor. Note how the effect ofthe first kick is "undone" by the second kick. A value of $\phi_d = 2.5$ and $\beta = 0$ were used at $T = T_{1/2}$.

Taking the initial state as $\psi_0(\theta)$, the state after the first kick is given (apart from a constant phase factor) by

$$\hat{U}_R\psi_0(\theta) = \mathrm{e}^{-i\phi_d\cos(\theta-\gamma)}\psi_0(\theta-\tau_\beta), \tag{7.15}$$

where $\tau_\beta = \pi a(2\beta+1)$. The state after two kicks, is

$$\hat{U}_R^2\psi_0(\theta) = \mathrm{e}^{-i\phi_d\cos(\theta-\gamma)}\mathrm{e}^{-i\phi_d\cos(\theta-\gamma-\tau_\beta)}\psi_0(\theta-2\tau_\beta). \tag{7.16}$$

Proceeding the same way, the state after t kicks is

$$\hat{U}_R^t\psi_0(\theta) = \exp\left(-i\phi_d\sum_{l=0}^{t-1}\cos(\theta-\gamma-l\tau_\beta)\right)\psi_0(\theta-t\tau_\beta). \tag{7.17}$$

The sum in the exponent can be simplified using the relation, $\sum_{s=0}^{t-1}\mathrm{e}^{\alpha s} = (1-\mathrm{e}^{\alpha t})/(1-\mathrm{e}^{\alpha})$. Thus

$$\sum_{l=0}^{t-1}\cos(\theta-\gamma-l\tau_\beta) = \alpha_t\cos(\theta-\phi_t), \tag{7.18}$$

where

$$\begin{aligned}\alpha_t &= \frac{\sin(\tau_\beta t/2)}{\sin(\tau_\beta/2)},\\ \phi_t &= \frac{\tau_\beta}{2}(t-1)+\gamma.\end{aligned} \tag{7.19}$$

It can be seen that $\alpha_t = t$ when $\tau_\beta = 0$. The wave function after t kicks reduces to

$$\langle\theta|\hat{U}_R^t\psi_0\rangle = \mathrm{e}^{-i\phi_d\alpha_t\cos(\theta-\phi_t)}\psi_0(\theta-t\tau_\beta). \tag{7.20}$$

In momentum representation, the wavefunction has the form

$$\langle n|\hat{U}_R^t\psi_0\rangle = \int_0^{2\pi}\mathrm{d}\theta\langle n|\theta\rangle\langle\theta|U_R^t\psi_0\rangle \tag{7.21}$$

$$= \frac{1}{\sqrt{2\pi}}\int_0^{2\pi}\mathrm{d}\theta\ \mathrm{e}^{-in\theta}\mathrm{e}^{-i\phi_d\alpha_t\cos(\theta-\phi_t)}\psi_0(\theta-t\tau_\beta) \tag{7.22}$$

$$= i^n\mathrm{e}^{-in\phi_t}\sum_m c_m\mathrm{e}^{im(\phi_t-t\tau_\beta-\pi/2)}J_{m-n}(\phi_d\alpha_t). \tag{7.23}$$

where an initial state of the form

$$\psi_0(\theta) = \sum_m\frac{c_m}{\sqrt{2\pi}}\mathrm{e}^{im\theta} \tag{7.24}$$

and the property of the bessel functions

$$\mathrm{e}^{-ik\cos(\theta)} = \sum_{l=-\infty}^{\infty} (-i)^l J_l(k)\mathrm{e}^{-il\theta} \tag{7.25}$$

are used. The momentum distribution is given by

$$\begin{aligned} p_n &= \left|\langle n|U_R^t\psi_o\rangle\right|^2 \\ &= \sum_m \sum_{m'} c_m^* c_{m'} \mathrm{e}^{-i(m-m')(\phi_t - t\tau_\beta - \pi/2)} J_{m-n}(\phi_d\alpha_t) J_{m'-n}(\phi_d\alpha_t). \end{aligned} \tag{7.26}$$

7.2.7 Mean momentum of a kicked rotor

The mean momentum is given by

$$\begin{aligned} \bar{P} &= \sum_{n=-\infty}^{\infty} (n+\beta) p_n \\ &= \sum_m \sum_{m'} [c_m^* c_{m'} \mathrm{e}^{-i(m-m')(\phi_t - t\tau_\beta - \pi/2)} \\ &\qquad \sum_{n=-\infty}^{\infty} (n+\beta) J_{m-n}(\phi_d\alpha_t) J_{m'-n}(\phi_d\alpha_t)]. \end{aligned} \tag{7.27}$$

Using the properties of the Bessel functions

$$\sum_{m_1=-\infty}^{\infty} m_1 J_{n-m_1}(k) J_{m-m_1}(k) = m\delta_{mn} - k/2(\delta_{m,n-1} + \delta_{m,n+1}) \tag{7.28}$$

and

$$\sum_{m_1=-\infty}^{\infty} J_{n-m_1}(k) J_{m-m_1}(k) = \delta_{mn}, \tag{7.29}$$

the mean momentum reduces to

$$\bar{p} - p_0 = -\phi_d\alpha_t/2 \sum_m \left(c_m^* c_{m+1} \mathrm{e}^{i(\phi_t - t\tau_\beta - \pi/2)} + c_m^* c_{m-1} \mathrm{e}^{-i(\phi_t - t\tau_\beta - \pi/2)} \right), \tag{7.30}$$

where $p_0 = \sum_m (m+\beta)\left|c_m\right|^2$ is the mean momentum corresponding to the initial state $\psi_0(\theta)$. If the initial state is a simple plane wave $|n_0\rangle$, then $c_m = \delta_{m,n_0}$, and $\bar{p} - p_0 = 0$. Thus an initial plane wave subjected to the QDKR spreads symmetrically in momentum. This result is independent of the phase γ associated with the kicking potential.

7.2.8 Mean energy of a kicked rotor

The mean energy of a kicked rotor is given by

$$\begin{aligned}
\langle E\rangle &= \frac{1}{2}\sum_{n=-\infty}^{\infty}(n+\beta)^2 p_n \\
&= \frac{1}{2}\sum_{mm'} c_m^* c_{m'} \mathrm{e}^{-i(m-m')(\phi_t - t\tau_\beta - \pi/2)} \\
&\quad \{\sum_{n=-\infty}^{\infty} n^2 J_{m-n}(\phi_d\alpha_t) J_{m'-n}(\phi_d\alpha_t) \\
&\quad +2\beta \sum_{n=-\infty}^{\infty} n J_{m-n}(\phi_d\alpha_t) J_{m'-n}(\phi_d\alpha_t) \\
&\quad +\beta^2 \sum_{n=-\infty}^{\infty} J_{m-n}(\phi_d\alpha_t) J_{m'-n}(\phi_d\alpha_t)\}
\end{aligned}$$

Applying the property of the Bessel functions

$$\begin{aligned}
\sum_{m_1=-\infty}^{\infty} m_1^2 J_{m_1-m}(x) J_{m_1-n}(x) = (n^2+\frac{x^2}{2})\delta_{mn} &- x\left[(m-\frac{1}{2})\delta_{m,n+1} + (n-\frac{1}{2})\delta_{n,m+1}\right] \\
&+\frac{x^2}{4}\left(\delta_{m,n+2}+\delta_{m,n-2}\right), \qquad (7.31)
\end{aligned}$$

and using $\langle E_0\rangle = \frac{1}{2}\sum_m |c_m|^2 (m+\beta)^2$ (the energy corresponding to the initial state), the mean energy is given by

$$\begin{aligned}
\langle E\rangle - \langle E_0\rangle &= \frac{1}{2}\sum_m \{\, |c_m|^2 \frac{\phi_d^2\alpha_t^2}{2} - c_m^* c_{m-1}\alpha_t\phi_d(m-\frac{1}{2}+\beta_0)\mathrm{e}^{-i(\phi_t - t\tau_\beta - \pi/2)} \\
&\quad -c_m^* c_{m+1}\alpha_t\phi_d(m+\frac{1}{2}+\beta_0)\mathrm{e}^{-i(\phi_t - t\tau_\beta - \pi/2)} \\
&\quad +\left(\frac{\alpha_t\phi_d}{2}\right)^2 \left(c_m^* c_{m+2}\mathrm{e}^{2i(\phi_t - t\tau_\beta - \pi/2)} + c_m^* c_{m-2}\mathrm{e}^{-2i(\phi_t - t\tau_\beta - \pi/2)}\right)\}.
\end{aligned}$$

For the simple initial state $|n_0\rangle$, the mean energy reduces to

$$\langle E\rangle - \langle E_0\rangle = \frac{\phi_d^2}{4}\frac{\sin^2(t\tau_\beta/2)}{\sin^2(\tau_\beta/2)}. \qquad (7.32)$$

It should be noted that for $\tau_\beta = 2r\pi$, where r is an integer, $\langle E\rangle - \langle E_0\rangle = \phi_d^2 t^2/4$. Thus a quadratic growth of mean energy can be observed for this resonant quasimomentum. This property has been used to identify resonances of the quantum kicked rotor [125, 27].

7.3 Quantum resonance ratchet

A natural question to arise out of the previous two sections is : can an initial state be created that leads to a non-zero mean momentum? As will be seen the answer to this question is yes. If the initial state is a superposition of two momentum states, i.e.,

$$\psi_0(\theta) = \frac{F}{\sqrt{2\pi}}\left(1 + A\mathrm{e}^{i\theta}\right) \tag{7.33}$$

where A is a complex number given by $A = |A|\exp(-i\gamma_0)$ and $F = \frac{1}{\sqrt{1+|A|^2}}$ is a normalization constant. Using this initial state in Eq. (7.30), the mean momentum becomes

$$\bar{p} - p_0 = -\frac{\phi_d|A|}{1+|A|^2}\frac{\sin(t\tau_\beta/2)}{\sin(\tau_\beta/2)}\sin\left[\gamma - \gamma_0 - (t+1)\tau_\beta/2\right]. \tag{7.34}$$

For the resonant case, i.e., $\tau_\beta = 2r\pi$, the mean momentum expression is even simpler

$$\bar{p}_r - p_0 = -\frac{\phi_d|A|}{1+|A|^2}t\sin(\gamma - \gamma_0) = Rt, \tag{7.35}$$

where R is called the ratchet coefficient and is given by

$$R = -\frac{\phi_d|A|}{1+|A|^2}\sin(\gamma - \gamma_0). \tag{7.36}$$

Thus the mean momentum increases linearly with time (number of kicks) at a resonance. This is the quantum resonance ratchet. The ratchet mechanism can be seen resulting from the non-coincidence of the symmetry centers of the atomic wave function γ_0 and the standing wave γ as shown in Fig. 7.6. There is no ratchet for the case when $\gamma = \gamma_0$. The mean energy for this case is given by

$$\langle E\rangle - \langle E_0\rangle = \frac{\phi_d^2}{4}\frac{\sin^2(t\tau_\beta/2)}{\sin^2(\tau_\beta/2)} + \frac{\tau_\beta}{\pi a}(\bar{p} - p_0). \tag{7.37}$$

For the resonant quasimomentum, the energy is given by

$$\langle E\rangle_r - \langle E_0\rangle = \frac{\phi_d^2 t^2}{4} - 2\left(\frac{r}{a}\right)Rt. \tag{7.38}$$

which shows that the mean energy is still quadratic in t. This case is called super-diffusive or ballistic expansion. Thus a net momentum (linear in t) can be extracted from a super-diffusive process.

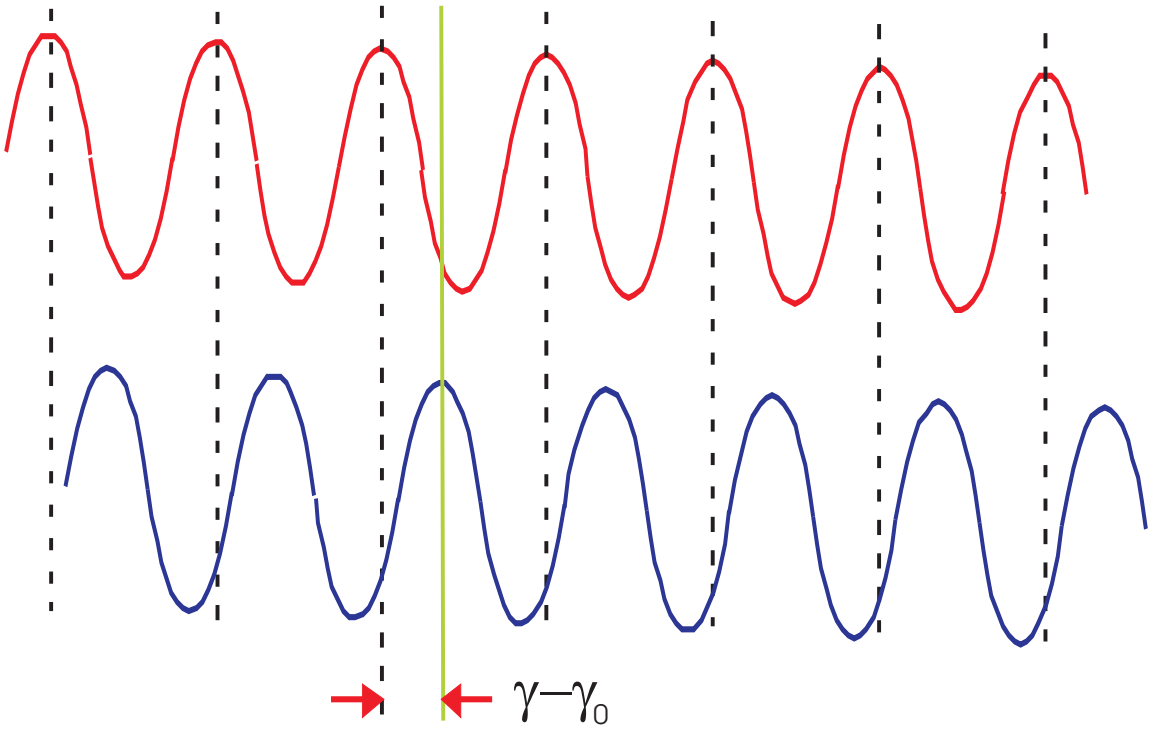

Figure 7.6: Physical picture of quantum ratchet. Diagram shows the symmetry centers of potential and the initial distribution. The non coincidence of the symmetry centers results in the quantum ratchet. The top red curve is the initial distribution $|\psi_0(\theta)|^2 \sim \cos(\theta - \gamma_0)$ and the bottom blue curve is the kicking potential (which is proportional to $\cos(\theta - \gamma)$).

7.4 Experimental configuration

The experimental setup is as shown in Fig. 7.7. BEC was produced as described in chapter 4. After making a BEC, it was released and a Bragg pulse was applied. A longer (typically around 38 μs) and less intense application of the standing wave creates the Bragg pulse. Bragg diffraction was first observed for atomic beams by David Pritchard's group [126] and later using a BEC by William Phillip's group [127]. Bragg diffraction can be used to measure the scattering length of the BEC which is an important parameter of the BEC [128, 129]. Bragg diffraction is a convenient way of splitting the atomic beam in atom interferometers [130]. The Bragg pulse diffracts atoms into a superposition of $|0\hbar G\rangle$ and $|1\hbar G\rangle$ states (referred to as $|0\rangle$ and $|1\rangle$ states from now on). The energy and momentum conservation in the diffraction process allows the atoms to diffract only at certain values of initial momentum [127]. This standing wave light was red detuned by 6.9 GHz to the atomic transition and was propagated through two Acousto-Optic Modulators (AOMs), were driven with rf electrical signals described by the equations

$$\begin{aligned} \text{AOM1}: &\quad \text{Amp} \quad \sin(\omega t') \\ \text{AOM2}: &\quad \text{Amp} \quad \sin\left[(\omega+\omega_D)\,t'-\gamma\right], \end{aligned}$$

where Amp is the amplitude of the rf waveform. An important property of the AOMs is that they can shift the frequency of the light passing through them by an amount equal to the frequency with which they are driven (in this case ω and $\omega+\omega_D$). An arbitrary wave form synthesizer was used to generate a 40 MHz sine wave to drive AOM1 given by $\omega/2\pi = 40$ MHz. Another synthesizer (which was phase locked to the first one) supplied a frequency that was varied according to

$$\omega_D = (2\pi/T_{1/2})\beta + Gat'/2 \tag{7.39}$$

so as to control the initial momentum β and the acceleration a of the standing wave with respect to the atoms. The standing wave was oriented at 52^o with respect to the

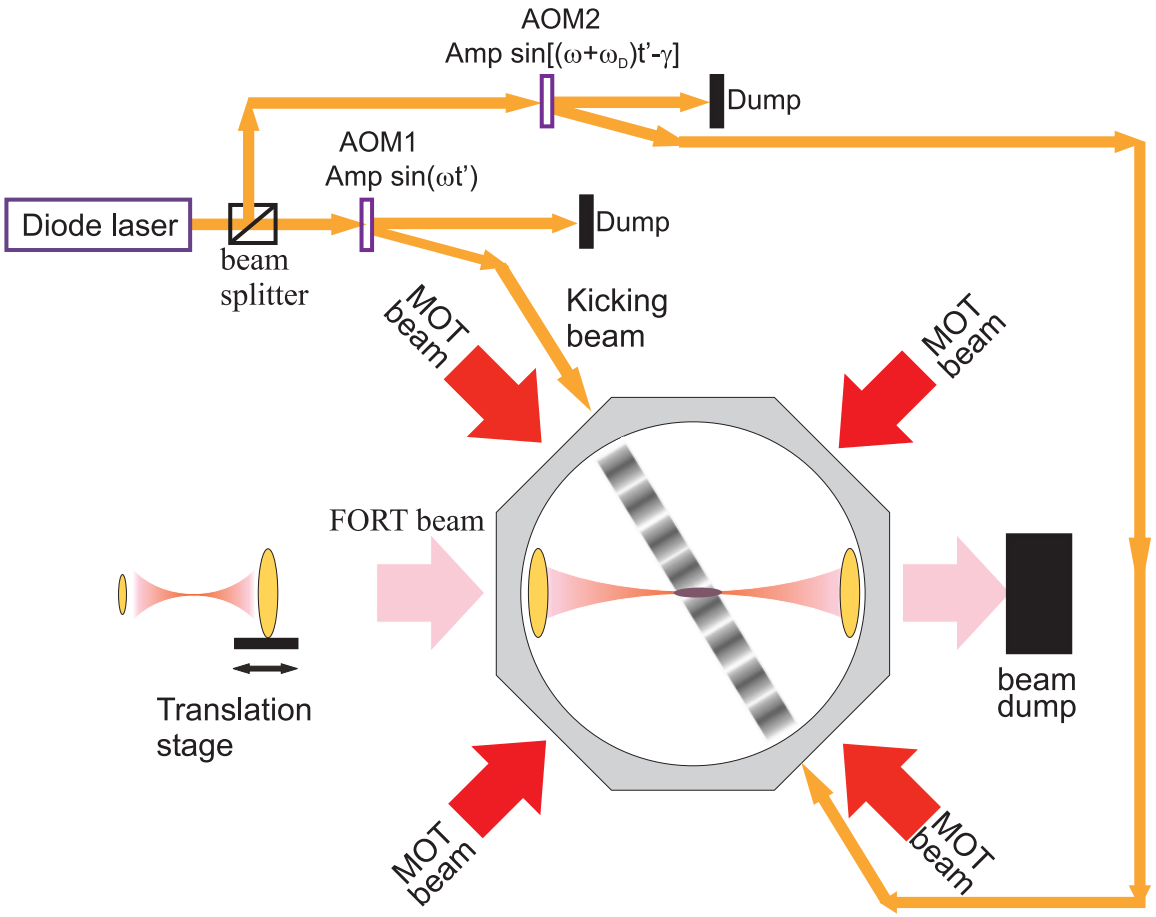

Figure 7.7: Experimental set up used for the realization of the quantum resonance ratchet

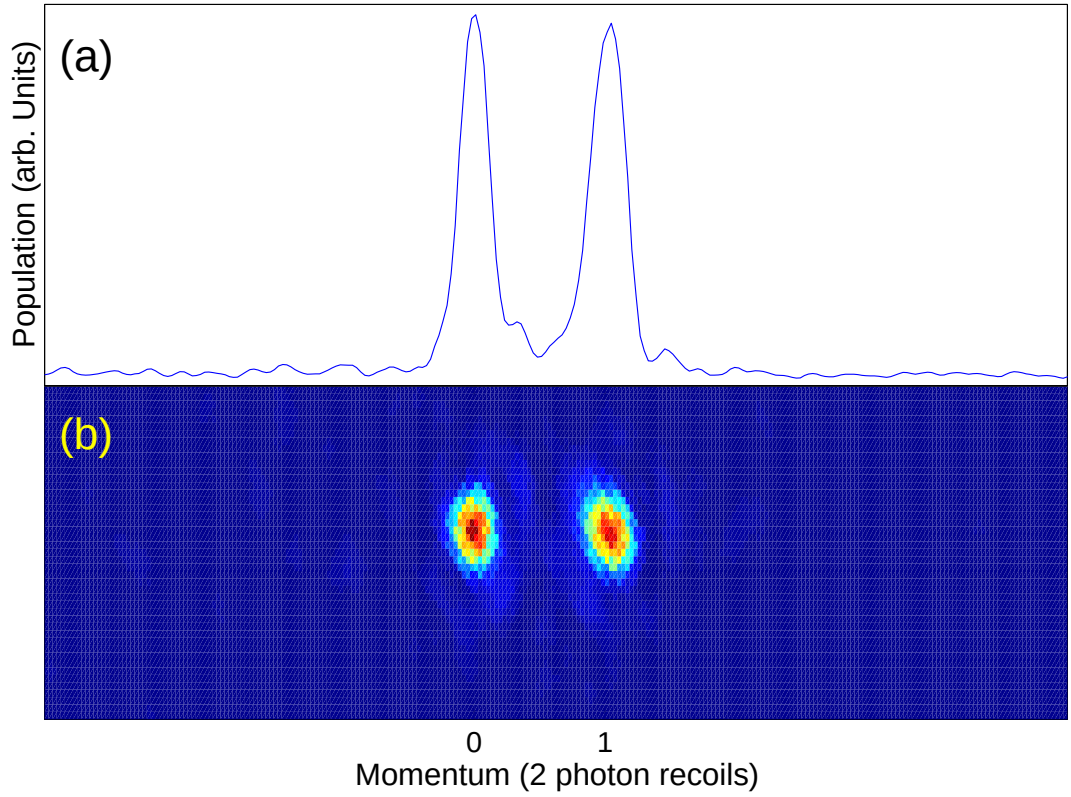

Figure 7.8: Momentum distribution of the superposition $|0\rangle$ and $|1\rangle$ states after Bragg diffraction. (a) is the signal integrated along the vertical axis and shows the equal population in the two states, (b) is a raw image of the momentum distribution

vertical. The method described above allowed the standing wave to be accelerated in order to cancel the component of gravitational acceleration along the direction of the standing wave. The Bragg diffraction of the BEC as a function of the initial momentum is displayed in Fig. 7.9. The figure shows the population of $|-1\rangle$, $|0\rangle$ and$|1\rangle$ levels as the initial momentum was changed. The standing wave that was producing the superposition state was moved to vary the initial momentum. For certain initial momenta, all the atoms can be transferred into the $|1\rangle$ state making it a π pulse. For the experiments discussed in this chapter, the initial momentum was chosen so that the $|0\rangle$ and $|1\rangle$ states were equally populated. This Bragg pattern is shown in Fig. 7.8. Figure 7.8(a) shows the distribution of atoms in the $|0\rangle$ and $|1\rangle$ states. After a superposition was created, a series of short intense pulses were applied. These pulses simulate δ pulses. In the experiments, the pulses were ~ 2 μs long with a period of 33.152 μs (which is the half-Talbot time for Rb-87 atoms). The pulsing sequence is shown in Fig. 7.10. The first long pulse represents the Bragg pulse. In the experiments, up to 5 pulses were used.

7.5 Experimental results

The experiments were carried out at $T = T_{1/2}$ which makes $a = 1$. Thus there is only one resonant τ_β possible (corresponding to $r = 1$). From Fig. 7.8, it can be seen that the states $|0\rangle$ and $|1\rangle$ have a non zero momentum width. This width was found to play an important role in the experiment. To account for the width, the BEC can be assumed to have a Gaussian distribution $(1/\sqrt{2\pi\sigma_\beta^2})\mathrm{e}^{-((\beta'-\beta)^2/2\sigma_\beta^2)}$ with a width σ_β and average $(\bar{p}-p_0)(\beta')$ over β',

$$\langle \bar{p}-p_0\rangle_\beta = \int_{-\infty}^{\infty} \mathrm{d}\beta'(\bar{p}-p_0)(\beta')\frac{1}{\sqrt{2\pi\sigma_\beta^2}}\mathrm{e}^{-\left((\beta'-\beta)^2/2\sigma_\beta^2\right)}. \tag{7.40}$$

Using the relation

$$\sum_{l=1}^{t}\sin\left(l\tau_\beta-\gamma\right) = \sin\left[\left(t+1\right)\tau_\beta/2-\gamma\right]\frac{\sin\left(t\tau_\beta/2\right)}{\sin\left(\tau_\beta/2\right)}, \tag{7.41}$$

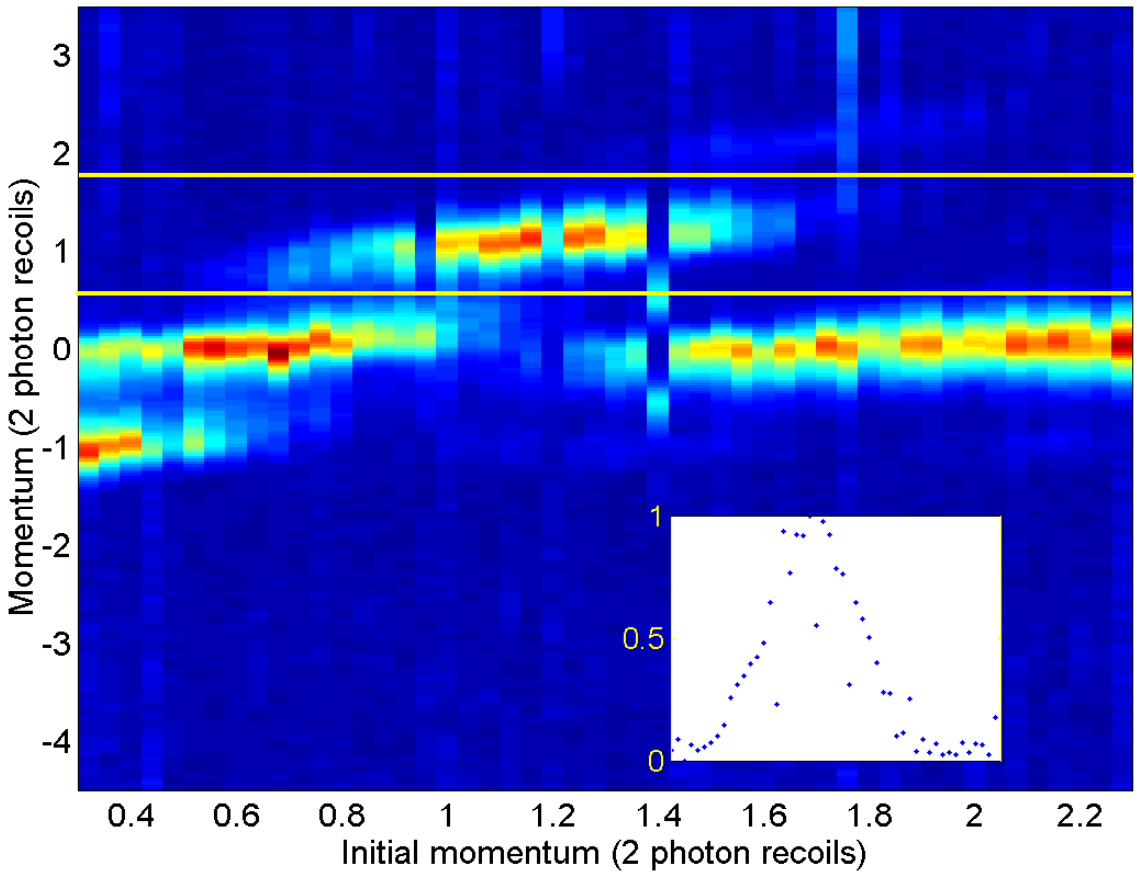

Figure 7.9: Scan of initial momentum to produce Bragg diffraction. The population in the $|1\rangle$ state is depicted between the two solid lines. The inset shows the population in the $|1\rangle$ state as a function of the initial momentum of BEC.

the averaged mean momentum is

$$\langle \bar{p} - p_0 \rangle_\beta = \frac{\phi_d |A|}{1 + |A|^2} \sum_{l=1}^{t} \mathrm{e}^{-2l^2\sigma_\beta^2\pi^2} \sin(l\tau_\beta - \gamma) \tag{7.42}$$

In the experiments, the equal superposition of $|0\rangle$ and $|1\rangle$, corresponding to $|A| = 1$ was used.

The plot of mean momentum vs γ is shown in Fig. 7.11. The data was obtained by subjecting the BEC to a Bragg pulse followed by 5 standing wave pulses. The initial momentum used in the experiment was $\beta = 0.5$. The data fits well with a width $\sigma_\beta = 0.056$. This value was in accordance with the value of the width measured using time-of-flight. Both the theory and experiments suggested that the mean momentum was maximum for $\gamma = \pi/2$. Thus $\gamma = \pi/2$ was used in the later experiments on pulse number and quasi-momentum. The data also demonstrated that the finite (but small) width can suppress the ratchet effect. Figure 7.12 shows a scan of the initial momentum of the distribution after a Bragg pulse on the BEC. This initial momentum was changed by moving the standing wave with respect to the atoms after the Bragg pulse was applied. Five standing wave pulses were applied. The data shows that the oscillations shown by the theory curve (dotted line) are smoothed out because of the finite width of the BEC. The experimental data again fits well with a width $\sigma_\beta = 0.056$. Figure 7.13 shows the plot of mean momentum vs pulse number. The saturation of the mean momentum which is a result of finite width of BEC can be seen. For the experimental parameters of $\tau_\beta = 2\pi$, $a = 1$, the value of the ratchet coefficient is $-\phi_d/2$. The experiments were performed at $\phi_d = 1.4$. Thus R is -0.7. The theoretical line shows this slope well.

To summerize, a the ratchet mechanism was demonstrated in this chapter using a δ-kicked rotor. The suppression of the mean momentum due to the finite width of the BEC was for the first time investigated and shown to have a significant effect, which was not accounted for in the experiments performed in another group at the same time as this work was pursued [36]. The quantum ratchet mechanism predicts

that a large mean momentum can be transferred by increasing ϕ_d.

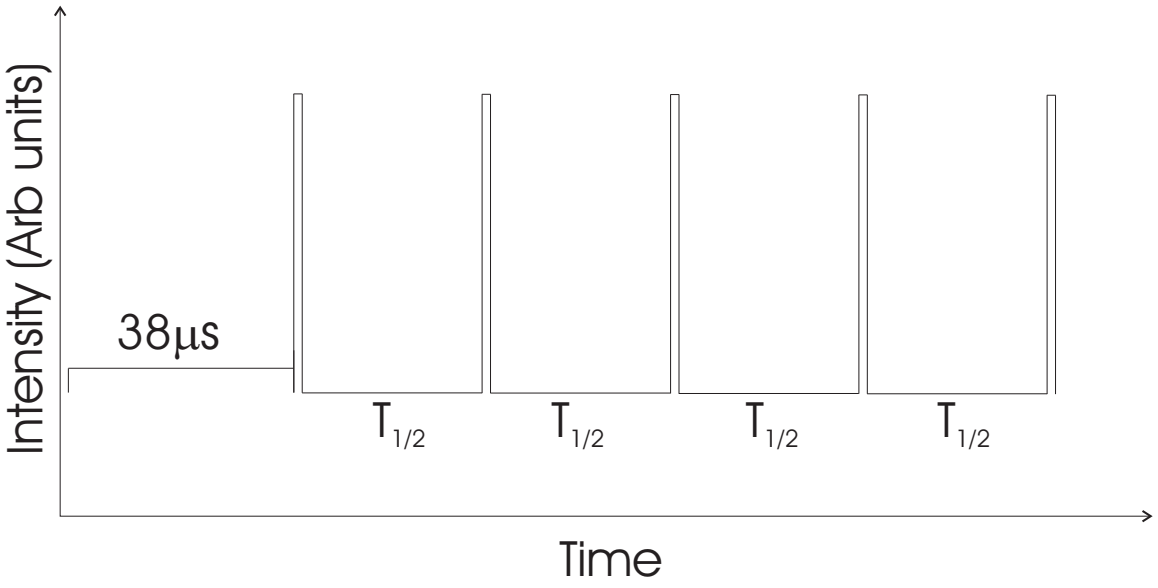

Figure 7.10: Pulsing sequence used in realizing the quantum ratchet. The long and less intense Bragg pulse creates a superposition of $|0\rangle$ and $|1\rangle$. The short intense kicking pulses produce the potential required to realize the ratchet.

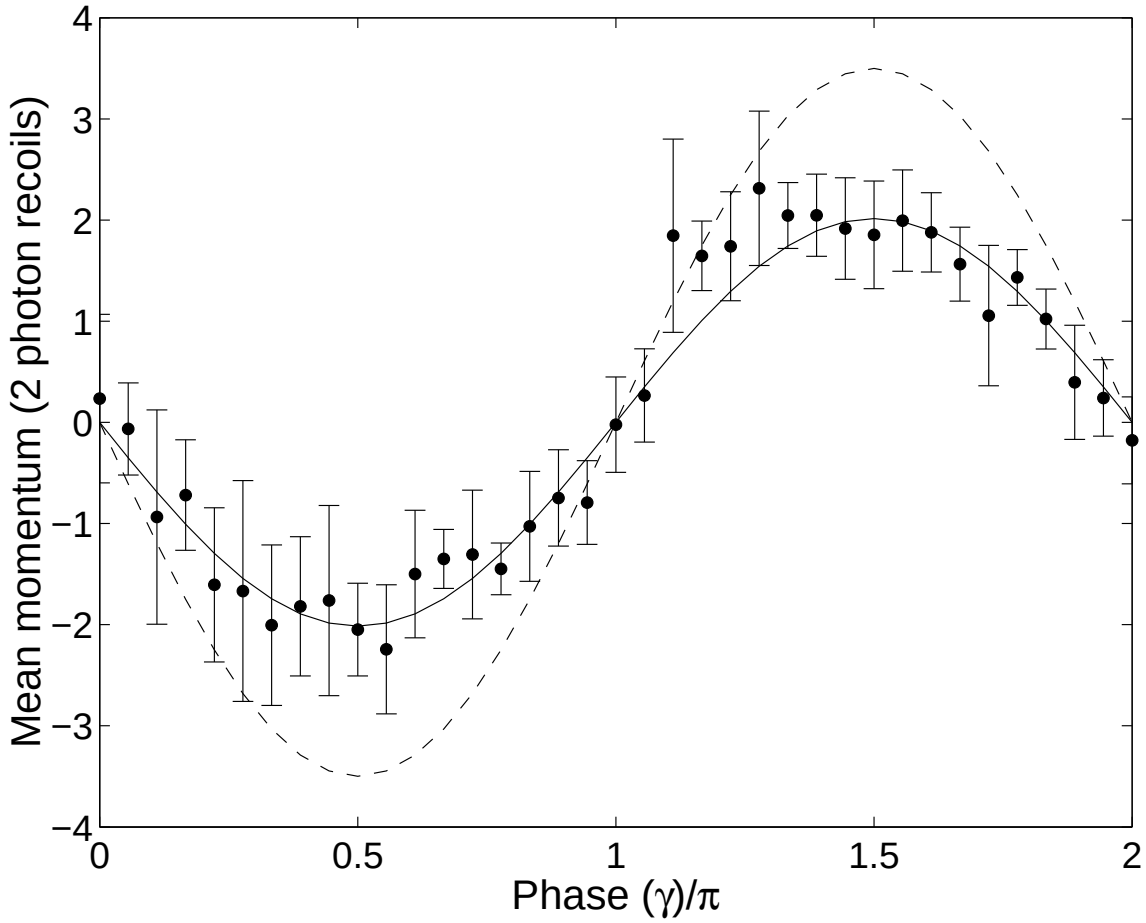

Figure 7.11: Mean momentum as a function of the phase γ for $\gamma_0 = 0$ after 5 pulses. Dotted line corresponds to Eq. (7.34) and the solid line corresponds to Eq. (7.42) with $\sigma_\beta = 0.056$.

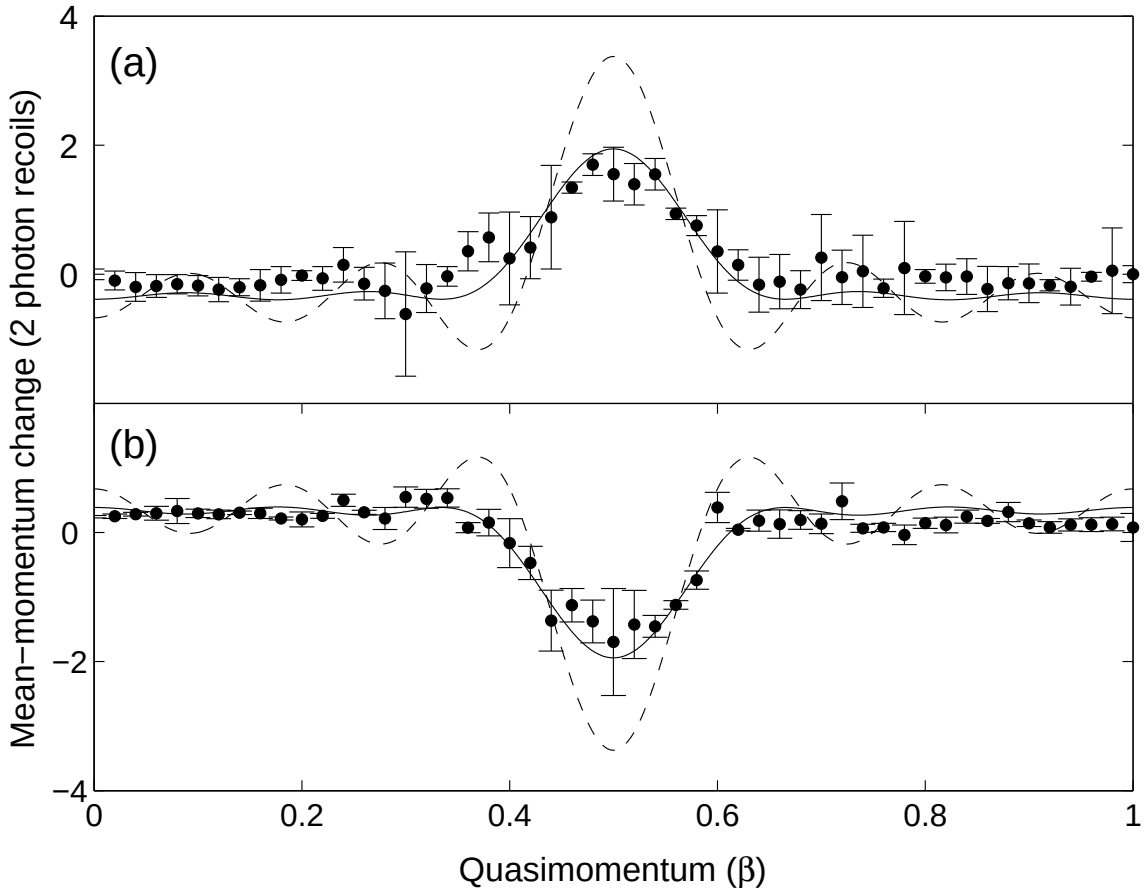

Figure 7.12: Plot of mean momentum as a function of the quasimomentum β. The ratchet happens at the resonance value of β which can be seen to be 0.5 for this case. The dotted curve is a fit to Eq. (7.34). The solid curve is the result of averaging the mean momentum over the initial momentum (or a convolution of the data with a gaussian of width 0.056)

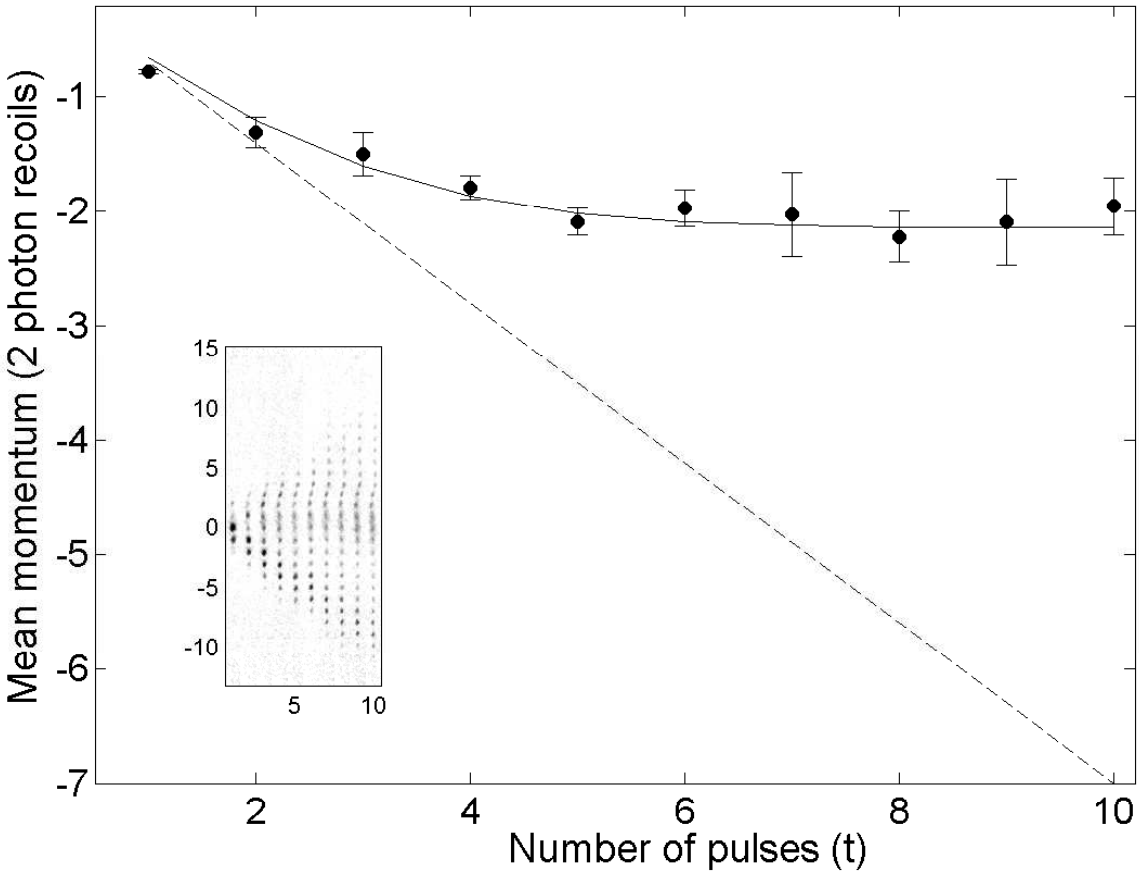

Figure 7.13: Plot of mean momentum vs pulse number. The dotted line corresponds to Eq. (7.34) and the solid line corresponds to the Eq. (7.42) with $\sigma_\beta = 0.056$. The inset shows the raw data and the drift of mean momentum towards the lower part of the figure.

CHAPTER 8

Ratchet using the δ-kicked accelerator

8.1 Introduction

The realization of the quantum ratchet using a δ-kicked rotor has been explored in chapter 7. It is thus pertinent to ask the question: does such a ratchet mechanism also exist in the kicked accelerator? Dana and coworkers answered this question theoretically [131]. Thus as an extension to the experiments described in chapter 7, the ratchet mechanism in the quantum δ-kicked accelerator was investigated. The results of this chapter were presented at the DAMOP 2008 conference [132]

8.2 Theory

According to the theory of I. Dana *et. al.* [131], for an initial state $|0\rangle + |1\rangle$, the kicked accelerator at resonance can show a ratchet effect for certain values of the acceleration. These values are given by $\eta = w/(LT_n)$ where w and T_n are integers and L is an integer representing a primary resonance of the kicked accelerator. In addition the resonance only occurs when the number of kicks is $n_p = v_n T_n$, where v_n is an integer. The mean momentum at these special values of the acceleration and kick number is given by

$$\langle \hat{N} \rangle - \langle \hat{N}_0 \rangle = \frac{\phi_d}{2} \frac{\sin(\tau_{\beta w} v_n T_n/2)}{\sin(\tau_{\beta w} T_n/2)} \sum_{s=0}^{T_n-1} \sin\left[\gamma + (v_n+1)\tau_{\beta w}\frac{T_n}{2} - \left(\tau_\beta s - \frac{\pi w s^2}{T_n}\right)\right], \tag{8.1}$$

where

$$\tau_{\beta w} = \tau_\beta + \pi w \tag{8.2}$$

and

$$\tau_\beta = \pi L(2\beta + 1). \tag{8.3}$$

The mean momentum is proportional to v_n when $\tau_{\beta w} T_n = \pi r$ for an integer r. The parameter values accessible within the experimental regime are shown in Table 8.1. For comparison, the parameters are also listed for the acceleration g' of 6 ms^{-2} (which

Table 8.1: Experimental parameters to observe a ratchet for $T = T_{1/2}$.

$\eta = w/T_n$	g' (ms^{-2})	w	T_n	v	Kicks
1/1	355	1	1	integer	integer
1/10	35.5	1	10	1	10
				2	20
				3	30
				4	40
1/20	17.75	1	20	1	20
				2	40
1/15	23.7	1	15	1	15
				2	30
1/5	71	1	5	1	5
				2	10
				3	15
				4	20
				5	25
				6	30
				7	35
				8	40
1/59	6 (*natural* gravity)	1	59	1	59

corresponds to the *natural* value of gravity) in the last row of the table. Table 8.2

shows parameters that would be necessary to observe the ratchet at $T = 2T_{1/2}$. The tables were generated up to kick number of 40. In the experiments, it was found that at a a resonance, for kick numbers greater than 20, the distribution would go beyond the field of view of the CCD camera used for imaging the atoms.

8.3 Numerical simulation results of the ratchet with a kicked accelerator

The numerical simulations were performed for the parameters that were feasible in the experiments. The simulation program described in section 3.7 was modified to take account of the initial state being a superposition of the $|0\rangle$ and $|1\rangle$ momentum states. The results of the numerical simulation were then compared with the theory of Eq. (8.1). Figure 8.1 shows a plot of the numerical simulation compared to the theory of Eq. (8.1). The simulation data in Fig. 8.1 was generated assuming a width of the BEC of $\sigma_\beta = 0.056$, identical to the width found in the experiments described in chapter 7. The solid curve in the Fig. 8.1 corresponds to the theory of Eq. (8.1) averaged over a Gaussian distribution of initial momentum with a width of $\sigma_\beta = 0.056$. The plot was generated for 15 kicks at an acceleration of $g' = 71$ ms^{-2} and a kicking period of the half-Talbot time, $T_{1/2}$. These parameters fix the values of $w = 1$, $T_n = 5$ and $v = 3$. The plot thus indicates that there is a good agreement between theory and the numerical simulations and that the width of the BEC is important as well.

The simulations were then extended to see the behavior of the ratchet mechanism as a function of kick number as shown in Fig. 8.2. It can be seen that the ratchet saturates due to the finite width of the BEC. The theory predicts that the variation in the mean momentum is small (maximum variation of 0.25 $\hbar G$). This makes it difficult to observe this ratchet behavior in the case of kicked accelerator. Both numerical simulations and the theory show the general trend of saturation, but there is a small disagreement between the theory and simulation for kick numbers greater than 25. It should be noted that the theory is only valid for kick numbers which are

Table 8.2: Experimental parameters to observe a ratchet at $T = 2T_{1/2}$.

$\eta = w/T_n$	g' (ms^{-2})	w	T_n	v	Kicks
1/1	89.1	1	1	integer	integer
1/10	8.91	1	10	1	10
				2	20
				3	30
				4	40
1/20	4.45	1	20	1	20
				2	40
1/15	5.94	1	15	1	15
				2	30
1/5	19.82	1	5	1	5
				2	10
				3	15
				4	20
				5	25
				6	30
				7	35
				8	40

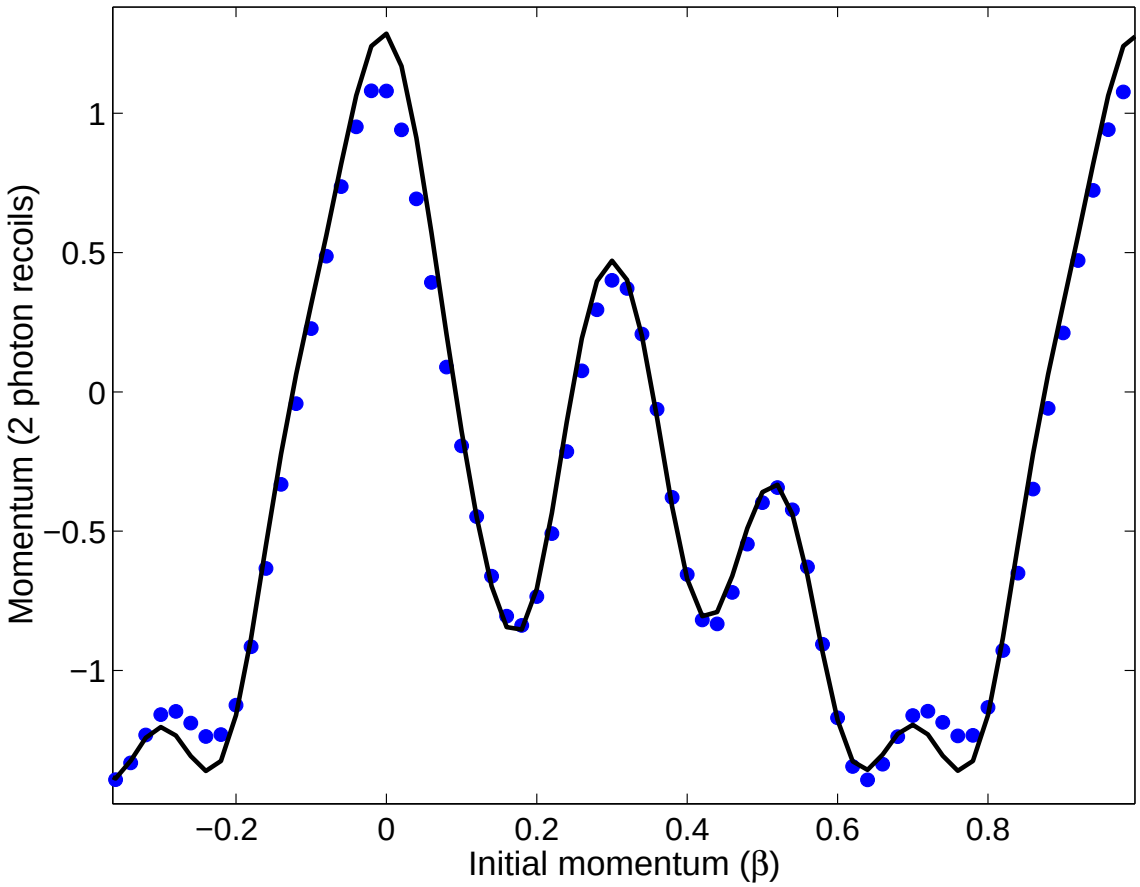

Figure 8.1: Plot of mean momentum as a function of initial momentum for the δ-kicked accelerator. Filled circles are the results of the numerical simulations. Solid line corresponds to eq. (8.1) with $\sigma_\beta = 0.056$.

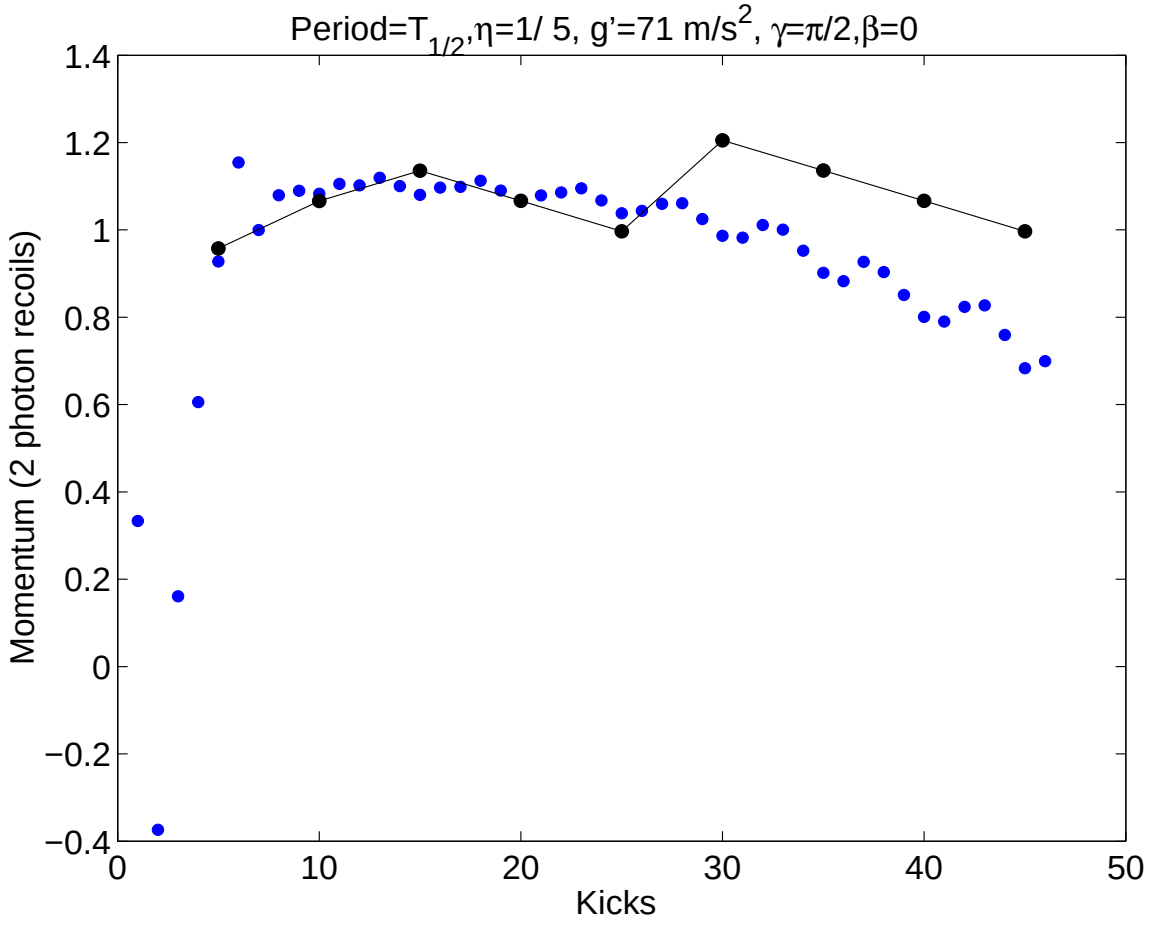

Figure 8.2: Plot of mean momentum as a function of kicks for the δ-kicked accelerator. Filled blue circles are the results of the numerical simulations. Solid line and the filled black circles correspond to Eq. (8.1) with $\sigma_\beta = 0.056$. The parameters used in the in this scan are $g' = 71$ ms^{-2},$T = T_{1/2}$ $w = 1$ and $T_n = 5$,

a multiples of T_n, which is 5 for the parameters used in generating this data. The values of the acceleration $g' = 71$ ms^{-2} and kicking period $T = T_{1/2}$ were used. For the identical parameters used to scan the initial momentum displayed in Fig. 8.1, the mean momentum is maximum for $\beta = 0$. Thus $\beta = 0.5$ was used in Fig. 8.2. The momentum distribution used for generating Fig. 8.2 is shown in Fig. 8.3. The asymmetric distribution of the population gives a qualitative picture of the ratchet mechanism.

8.4 Experimental results

The experiment to realize a ratchet with gravity is very similar to the experimental set up discussed in chapters 6 and 7. Briefly, the experiment consists of two AOMs which are used to accelerate and move the standing wave. It was found that the frequency change used on one of the AOMs (to accelerate the standing wave) was small enough (KHz range) that the first order beam from the AOM did not significantly deviate from the original direction, even for accelerations as high as 500 ms^{-2}. Experiments were performed for the parameters used in the simulations with a value of $\phi_d = 1.4$ used throughout.

Figure 8.4 shows the experimental result of a kick scan. The asymmetry in the population hints that a ratchet exists for these particular conditions. The parameters used are $g' = 35.5$ ms^{-2}, $\beta = 0.5$ and $T = T_{1/2}$. For these parameters the theory is valid for kick numbers that are a multiple of T_n which is 10.

A scan of initial momentum was undertaken to verify the predictions of the theory and is displayed in Fig. 8.5. The parameters used were $T = T_{1/2}$, $g' = 71$ ms^{-2}, and $\beta = 0$ (same as the parameters used in Fig. 8.1). This data shows that in general the trend of mean momentum as a function of initial momentum is predictable in the experiments.

In summary, a quantitative analysis of the experimental data for a quantum

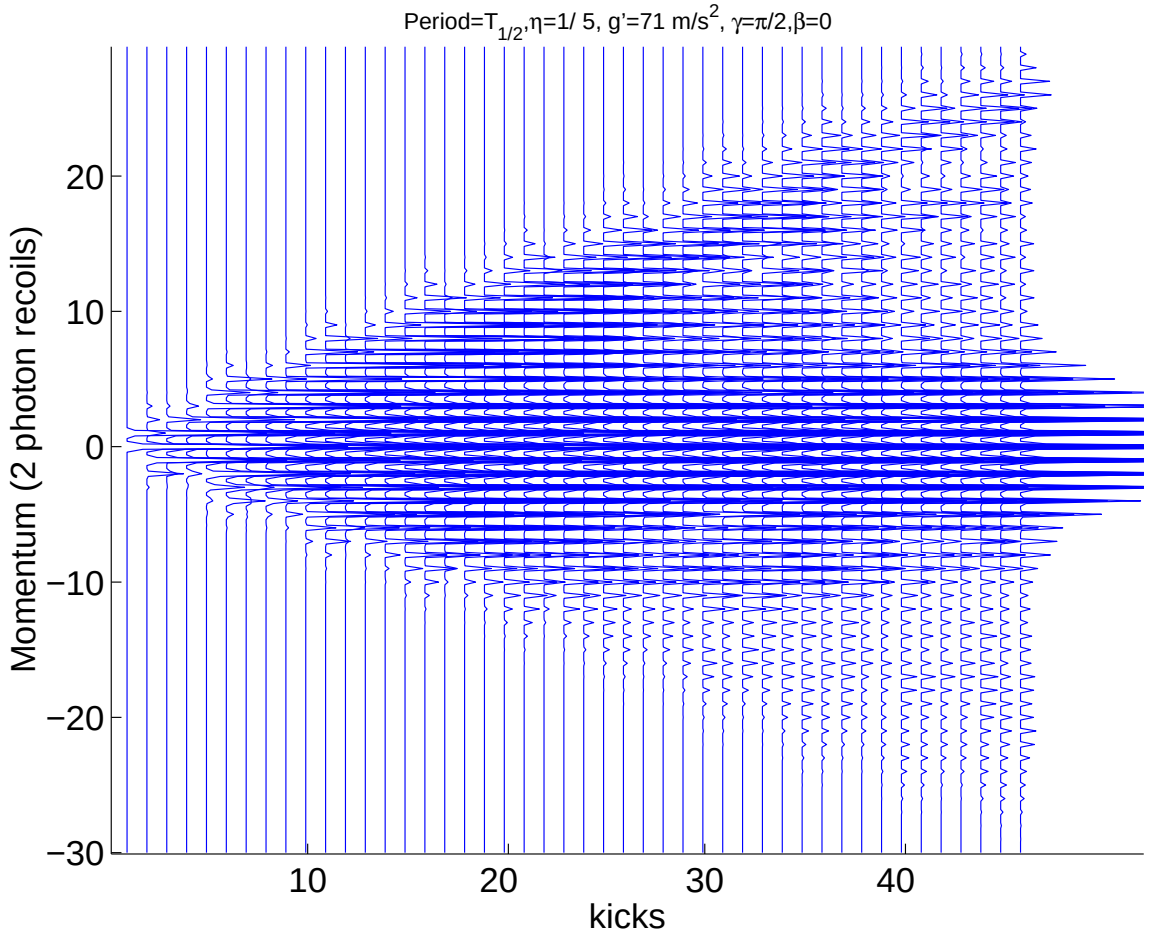

Figure 8.3: Numerical simulation of the momentum distribution for a scan of kicks. The asymmetry in the distribution of the population of orders on either side of zero momentum is a manifestation of the ratchet effect.

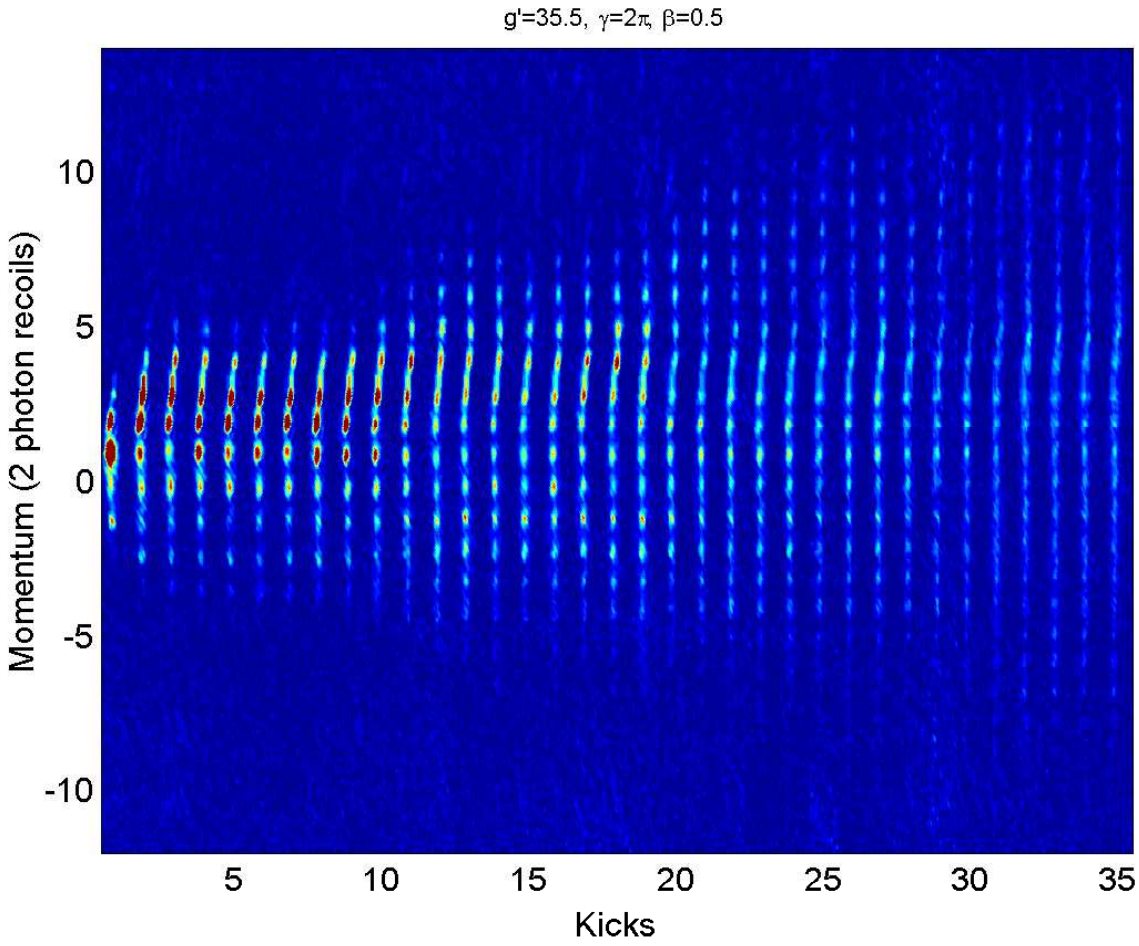

Figure 8.4: Experimental momentum distribution for a scan of kicks displaying the ratchet for the kicked accelerator. The asymmetry in the distribution of the population of orders on either side of zero momentum is a manifestation of the ratchet.

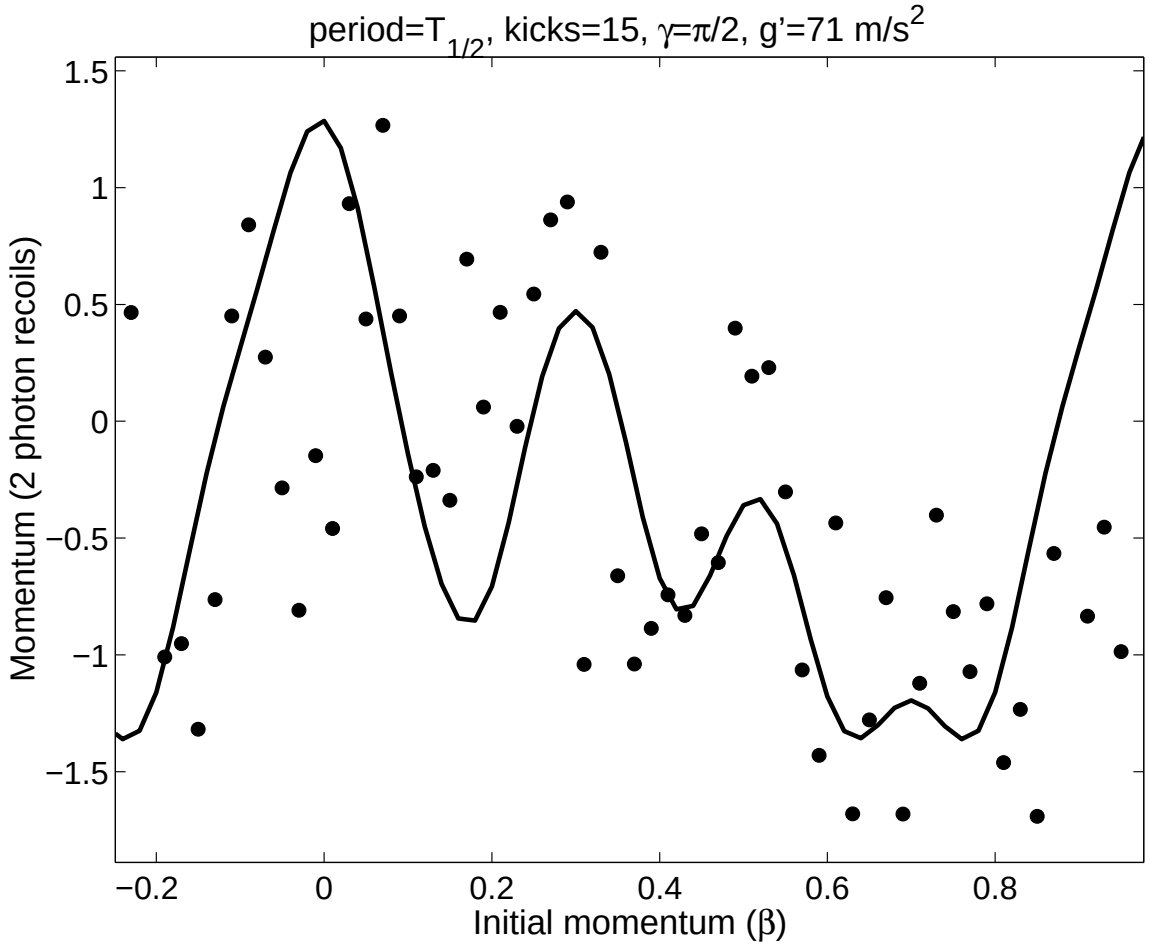

Figure 8.5: Experimental data of mean momentum as a function of initial momentum for the δ-kicked accelerator. Filled circles are the experimental data. The solid line corresponds to Eq. (8.1) with $\sigma_\beta = 0.056$.

ratchet in the case of the δ-kicked accelerator has been presented in this chapter. It is interesting to study the ratchet mechanism experimentally for this system because of the rich parameter regime predicted by the theory. The quantum ratchet effect for the δ-kicked accelerator is not as large as that of a δ kicked rotor for the identical parameters.

CHAPTER 9

Conclusions and Future work

9.1 Summary

The work described in this thesis involved the charecterization of several new aspects of kicked quantum systems. Although Bose-Einstein Condensation (BEC) was separately achieved in an independent experiment, the unexpected observation of multiple micro optical traps using the aberration of a lens was investigated as part of this report. An experimental design was developed which allowed cold atoms to be kicked by a standing light wave. This led to first observation of the quantum δ-kicked accelerator (and quantum accelerator modes) in BEC. Using a BEC to produce the quantum accelerator modes enabled us to successfully study details of phase space maps produced by modeling the δ-kicked accelerator as a classical system. When the BEC had a good overlap with the stable islands of the phase space, quantum accelerator modes were produced. This idea was utilized in chapter 5 to measure the size of the island and compare it to theory. This work has motivated the study of mean field interactions on quantum accelerator modes [114].

As discussed in chapter 6, higher order resonances of the quantum δ-kicked accelerator were observed for the first time. A generalized ϵ-classical theory was described in this chapter and the rephasing theory of primary resonant QAM was extended to explain the behavior of the higher order resonances. The rephasing of momentum orders separated by $b\hbar G$ for a resonance occurring at a/b of $T_{1/2}$ was clearly visible in the scans of the kick number. This fundamental aspect of higher order resonances was not observed in the earlier work of William D Phillips and coworkers [27]. Numerical

simulations were carried out and helped to understand the experimental data. These numerical results were used to identify the parameter regime where the high order resonances of the quantum δ-kicked accelerator were to be expected.

Perhaps the most important achievement of the work described here involved the first observation of a quantum ratchet using the resonances of the quantum δ-kicked rotor. Although similar work was concurrently conducted by a Japanese group, we developed a comprehensive theory to explain the ratchet and performed experiments that confirmed the dependence of the ratchet on quasimomentum β. (The Japanese group looked at the ratchet mechanism only at the initial momentum of $\beta = 0.5$.) It was also found that the finite width of the BEC had a dramatic effect on the ratchet and led to a saturation of the mean momentum after many kicks. For a much narrower momentum distribution, and a large value of ϕ_d, it is possible to produce a high mean momentum since the saturation effect is reduced. In the presence of a linear potential such as the one produced by gravity, the ratchet is seen only at certain values of gravity and kick number. This has been qualitatively investigated and was described in chapter 8. The experimentally accessible parameters at which the ratchet appears have been tabulated. Unfortunately the small change in the mean momentum made it difficult to observe the ratchet mechanism of the kicked accelerator with the current experimental parameters.

9.2 Future work

The apparatus and procedures developed in this thesis have opened up many new avenues of investigation which will help test fundamental theory. Some of the experiments that are currently being perused as well as some that are further in the future, are described below.

9.2.1 Loschmidt cooling

Laser cooling and trapping has revolutionized atom optics. When a sample of atoms are cooled, the velocity distribution gets narrowed. This is the signature of low temperatures used in all laser cooling and trapping experiments. Evaporative cooling is a process where atoms at the high end of the Boltzmann velocity distribution are lost in order to lower the temperature of the remaining atoms. Loschmidt cooling can occur when two sequences of kicks are applied to an atomic sample. If an atom has a certain initial momentum, then, the second set of kicks can reverse the effect of the first set. This time reversing process results in narrowing the momentum distribution [133]. The following theory sketches out the reason for this reversal.

Take the kicked rotor at $\beta = 0$. Two series of kicks are produced to observe the Loschmidt cooling. A first set of t_r kicks are produced at a kicking period of $\tau = 2\pi + \epsilon$. The one kick evolution operator for the first set of kicks is given by

$$U_1 = e^{-i\phi_d \cos\theta} e^{-i(2\pi+\epsilon)m^2} = e^{-i\phi_d \cos\theta} e^{-i\epsilon m^2}, \tag{9.1}$$

where ϕ_d is kicking strength. To observe Loschmidt cooling, a second set of t_r kicks are produced at a kicking period of $\tau = 2\pi L - \epsilon$, the kicking strength ϕ_d is changed to $-\phi_d$ and the kicking sequence is reversed. The one kick evolution operator for the second set of t_r kicks is given by

$$U_2 = e^{i\epsilon m^2} e^{i\phi_d \cos\theta} = U^{\dagger}. \tag{9.2}$$

The resulting evolution operator after $2t_r$ kicks becomes unity and thus the final state should be the same as the initial state. For a distribution of atoms around $\beta = 0$ (as in realistic experiments), the reversal is not perfect for atoms not exactly at $\beta = 0$. These atoms diffuse away and will not be observed in the final momentum distribution. This narrowing results in cooling. Such an experiment is straightforward to implement with the present experimental configuration. kicking period can easily

be varied and the sign of ϕ_d can be changed by altering the phase in cosine factor by π, i.e. $\phi_d \cos\theta$ can be replaced by $\phi_d \cos(\theta + \pi) = -\phi_d \cos\theta$.

9.2.2 Double kicking

Section 3.8 described how double kicking can produce a rich structure of quantum accelerator modes. Understanding these modes theoretically and experimentally by repeating these results using a BEC would enhance the understanding of the higher order modes. Furthermore, another kicking beam in a direction perpendicular to the current experimental arrangement could allow for the implementation of 2D kicked rotor. Theoretical work shows that there are two kicking time scales involved in the 2D kicked rotors [134, 135].

9.2.3 Kicked harmonic oscillator

The kicked Harmonic Oscillator (HO) can be described using the Hamiltonian

$$H = \frac{P^2}{2m} + \frac{1}{2}kx^2 + \hbar\phi_d \cos(Gx) \sum_{n_p} \delta(t' - n_p T). \tag{9.3}$$

The harmonic potential $(1/2)kx^2$ in the kicked harmonic oscillator replaces the linear potential of the kicked accelerator. The classical evolution results in a mapping given by

$$X_{n_p+1} = X_{n_p} \cos(\omega T) + \left[P_{n_p} + \hbar\phi_d G \sin(GX_{n_p})\right] \frac{\sin(\omega T)}{m\omega} \tag{9.4}$$

$$P_{n_p+1} = \left[P_{n_p} + \hbar\phi_d G \sin(GX_n)\right] \cos(\omega T) - m\omega X_{n_p} \sin(\omega T) \tag{9.5}$$

where $\omega = \sqrt{k/m}$ was used. Using new dimensionless variables $\theta = GX$ and $J = G/m\omega P$ and $\tilde{k} = (T_{1/2}/T_{HO})\phi_d$ where $T_{HO} = 2\pi/\omega$, the period of the harmonic potential, the mapping equations can be rewritten as

$$\theta_{n_p+1} = \theta_{n_p} \cos(\omega T) + \left(J_{n_p} + \tilde{k} \sin(\theta_{n_p})\right) \sin(\omega T) \tag{9.6}$$

$$J_{n_p+1} = \left(J_{n_p} + \tilde{k} \sin(\theta_n)\right) \cos(\omega T) - \theta_{n_p} \sin(\omega T). \tag{9.7}$$

Such a map has two time scales which are important: the kicking period T and the period of the harmonic potential T_{HO}. This map produces the stochastic web for certain parameter values of $\tilde{k}$ and the regular dynamics are with in the cells defined by the web [136]

With the experimental apparatus developed in the lab it is straightforward to perform the experiments on the kicked harmonic oscillator. The harmonic potential may be derived from the trap that is used to produce the BEC. The strength of the harmonic potential can be varied by changing the power in the CO_2 laser beam.

9.2.4 Quantum Accelerator Modes with atomic interactions

The investigation of QAM in BEC presented in chapter 5 motivated a further study of QAM with atomic interactions [114]. The QAM can be enhanced or depressed depending on the sign of the interaction. For large interactions, the QAM can even be suppressed. In the experiments, the strength of the interaction between the atoms in BEC can be changed via the Feshbach resonance. The QAM can be studied with atoms interacting with both attractive and repulsive atom atom interactions.

9.2.5 Study of complex potentials using BEC

Complex potentials can be produced by introducing spontaneous emission by mixing a controllable amount of on-resonant light with the kicking beams or introducing noise in the amplitude of the kicking potential. Atom interferometry with such complex potentials allows the study of the refractive index of the atomic beam in the potential.

Besides the use of kicked systems such as the δ-kicked rotor and δ-kicked accelerator studied in this dissertation as a candidates to study quantum chaos, the coherent manipulation of atomic waves can be useful in several contexts in atom optics such as interferometry and quantum information processing.

BIBLIOGRAPHY

BIBLIOGRAPHY

[1] Edward N. Lorenz, "Deterministic non-periodic flow," J. Atmos. Sci., **20**, 130 (1963).

[2] Herbert Goldstein, Charles Poole and John Safko, *Classical Mechanics,* 3rd edition, Addison Wesley, New York (2000)

[3] Reuben H. Simoyi, Alan Wolf, andHarry L. Swinney, "One-Dimensional Dynamics in a Multicomponent Chemical Reaction," Phys. Rev. Lett. **49**, 245 (1982).

[4] Rajarshi Roy, T. W. Murphy Jr., T. D. Maier, Z. Gills, and E. R. Hunt, "Dynamical Control of a Chaotic Laser: Experimental Stabilization of a Globally Coupled System," Phys. Rev. Lett. **68**, 1259 (1992).

[5] R. D. Hazeltine and J. D. Meiss, Plasma confinement (Addison-Wesley, Redwood City, 1992).

[6] Apostolos Serletis and Periklis Gogas, "Purchasing Power Parity Nonlinearity and Chaos," Applied Financial Economics, **10**, 615, (2000).

[7] A. Peres, *Quantum Theory: Concepts and Methods,* Kluwer Academic Publishers, Dordrecht, (1993).

[8] Boris V. Chirikov, "A universal instability of many-dimensional oscillator systems," Phys. Rep. **52**(5), 263, (1979).

[9] G. Casati, B. V. Chirikov, F. M. Izraelev, and Joseph Ford, "Stochastic behavior of a quantum pendulum under a periodic pertubation," in *Stochastic Behavior*

in Classical and Quantum Hamiltonian Systems, edited by G. Casati and J. Ford (Springer, Berlin, 1979), p. 334.

[10] J. E. bayfield, G. Casati, I Guarneri, and D. W. Sokol, "Localization of classically chaotic diffusion for Hydrogen atoms in microwave fields," Phys. Rev. Lett. **63**, 364 (1989).

[11] P. M. Koch, K. A. H. van Leeuwen, "The importance of resonances in microwave "ionization" of excited Hydrogen Rydberg atoms," Phys. Rep. **255**, 289 (1995).

[12] F. L. Moore, J. C. Robinson, C. Bharucha, P. E. Williams, and M. G. Raizen, "Observation of dynamical localization in atomic momentum transfer: A new testing ground for quantum chaos," Phys. Rev. Lett. **73**, 2974 (1994).

[13] F. L. Moore, J. C. Robinson, C. F. Bharucha, Bala Sundaram, and M. G. Raizen, "Atom optics realization of the quantum delta-kicked rotor," Phys. Rev. Lett. **75**, 4598 (1995).

[14] M. G. Raizen, F. L. Moore, J. C. Robinson, C. F. Bharucha, and Bala Sundaram, "An Experimental Realization of the Quantum delta-Kicked Rotor," Quantum and Semiclass. Optics **8**, 687 (1996).

[15] Robinson, C. Bharucha, F. L. Moore, R. Jahnke, G. A. Georgakis, Q. Niu, M. G. Raizen, and Bala Sundaram, "Study of Quantum Dynamics in the Transition from Classical Stability to Chaos," Phys. Rev. Lett. **74**, 3963 (1995).

[16] B. G. Klappauf, W. H. Oskay, D. A. Steck, and M. G. Raizen, "Observation of Noise and Dissipation Effects on Dynamical Localization,". Phys. Rev. Lett. **81**, 1203 (1998).

[17] B. G. Klappauf, W. H. Oskay, D. A. Steck, and M. G. Raizen, "Experimental Study of Quantum Dynamics in a Regime of Classical Anomalous Diffusion," Phys. Rev. Lett. **81**, 4044 (1998).

[18] B. G. Klappauf, D. A Steck, W. H. Oskay, and M. G. Raizen, "Quantum Chaos with Cold Cesium Atoms," Laser Physics **9**, 265 (1999).

[19] M. G. Raizen "Quantum Chaos with Cold Atoms," Advances in Atomic, Molecular and Optical Physics. **41**, Academic Press (1999) p.43-81.

[20] B. G. Klappauf, W. H. Oskay, D. A. Steck, and M. G. Raizen, "Quantum Chaos with Cesium Atoms: Pushing the Boundaries," Physica D **131**, 78 (1999).

[21] M. G. Raizen, "Experimental study of quantum chaos with cold atoms," Phil. Mag. B **80**, 2109 (2000).

[22] V. Milner, D. A. Steck, W. H. Oskay, and M. G. Raizen, "Recovery of Classically Chaotic Behavior in a Noise-Driven Quantum System," Phys. Rev. E **61**, 7223 (2000).

[23] Daniel A. Steck, Valery Milner, Windell H. Oskay, and Mark G. Raizen, "Quantitative Study of Amplitude Noise Effects on Dynamical Localization," Phys. Rev. E **62**, 3461 (2000).

[24] Daniel A. Steck , Windell H. Oskay , Mark G. Raizen, "Observation of Chaos-Assisted Tunneling Between Islands of Stability," Science, **293**, 274 (2001).

[25] D. A. Steck, W. H. Oskay, M. G. Raizen,"Fluctuations and decoherence in chaos-assisted tunneling," Phys. Rev. Lett. **88**, 120406 (2002).

[26] L. Deng, E. W. Hagley, J. Denschlag, J0i-9080 E. Simsarian, Mark Edwards, Charles W. Clark, K. Helmerson, S. L. Rolston, and W. D. Phillips, "Temporal, matter-wave-dispersion Talbot effect," Phys. Rev. Lett. **83**, 5407 (1999).

[27] C. Ryu, M. F. Andersen, A. Vaziri, M. B. d'Arcy, J. M. Grossman, K. Helmerson, and W. D. Phillips, " High-order quantum resonances observed in a periodically kicked Bose-Einstein Condensate," Phys. Rev. Lett. **96**, 160403 (2006).

[28] W. K. Hensinger, H. Hffner, A. Browaeys, N. R. Heckenberg, K. Helmerson, C. McKenzie, G. J. Milburn, W. D. Phillips, S. L. Rolston, H. Rubinsztein-Dunlop and B. Upcroft, " Dynamical tunnelling of ultracold atoms," Nature **412**, 52 (2001).

[29] J. Ringot, P. Szriftgiser, J. C. Garreau, D. Delande, "Experimental evidence of dynamical localization and delocalization in a quasi-periodic driven system," Phys. Rev. Lett. **85**, 2741 (2000).

[30] Pascal Szriftgiser, Jean Ringot, Dominique Delande, and Jean Claude Garreau, "Observation of Sub-Fourier resonances in a quantum chaotic system," Phys. Rev. Lett. **89**, 224101 (2002).

[31] A. J. Daley, A. S. Parkins, R. Leonhardt, and S. M. Tan, "Diffusion Resonances in Action Space for an Atom Optics Kicked Rotor with Decoherence," Phys Rev. E **65**, 035201(R) (2002).

[32] H. Ammann, R. Gray, I. Shvarchuck, N. Christensen, Quantum delta-kicked rotor: Experimental observation of decoherence, Phys. Rev. Lett. **80**, 4111, (1998).

[33] P. H. Jones, M. Goonasekera, D. R. Meacher, T. Jonckheere, and T. S. Monteiro, " Directed Motion for Delta-Kicked Atoms with Broken Symmetries: Comparison between Theory and Experiment," Phys. Rev. Lett. **98**, 073002 (2007).

[34] P. H. Jones, M. Goonasekera, and F. Renzoni, "Rectifying fluctuations in an optical lattice," Phys. Rev. Lett. **93**, 073904 (2004).

[35] G. Hur, C. E. Creffield, P. H. Jones, and T. S. Monteiro, " Chaotic quantum ratchets and filters with cold atoms in optical lattices: Analysis using Floquet states," Phys. Rev. A **72**, 013403 (2005).

[36] Mark Sadgrove, Munekazu Horikoshi, Tetsuo Sekimura, and Ken'ichi Nakagawa, " Rectified momentum transport for a kicked Bose-Einstein Condensate," Phys. Rev. Lett. **99**, 043002 (2007).

[37] S. R. Wilkinson, C. F. Bharucha, K. W. Madison, Qian Niu, and M. G. Raizen, "Observation of Atomic Wannier-Stark Ladders in an Accelerating Optical Potential," Phys. Rev. Lett. **76**, 4512 (1996).

[38] Qian Niu, Xian-Geng Zhao, G. A. Georgakis, and M. G. Raizen, "Atomic Landau-Zener Tunneling and Wannier-Stark Ladders in Optical Potentials," Phys. Rev. Lett. **76**, 4504 (1996).

[39] S. R. Wilkinson, C. F. Bharucha, M. C. Fischer, K. W. Madison, P. R. Morrow, Qian Niu, Bala Sundaram, and M. G. Raizen. "Experimental evidence for non-exponential decay in quantum tunnelling," Nature **387**, 575 (1997).

[40] K. W. Madison, C. F. Bharucha, P. R. Morrow, S. R. Wilkinson, Q. Niu, Bala Sundaram, and M. G. Raizen, "Quantum Transport of Ultra-Cold Atoms in an Accelerating Optical Potential," Applied Physics B **65**, 693 (1997).

[41] Q. Niu and M. G. Raizen, "How Landau-Zener Tunneling Takes Time," Phys. Rev. Lett. **80**, 3491 (1998).

[42] K. W. Madison, M. C. Fischer, and M. G. Raizen, "Observation of the Wannier-Stark fan and the fractional ladder in an accelerating optical lattice," Phys. Rev. A **60**, R1767 (1999).

[43] M. C. Fischer, B. Gutirrez-Medina, and M. G. Raizen, "Observation of the Quantum Zeno and Anti-Zeno Effects in an Unstable System," Phys. Rev. Lett. **87**, 040402 (2001).

[44] M. K. Oberthaler, R. M. Godun, M. B. d'arcy, G. S. Summy, and K. Burnett, "Observation of quantum accelerator modes," Phys. Rev. lett. **83**, 4447 (1999).

[45] R.M. Godun, M.B. d'Arcy, M.K. Oberthaler, G.S. Summy, and K Burnett, "Quantum accelerator modes: a tool for atom optics," Phys. Rev. A **62**, 013411 (2000).

[46] M. B. d'Arcy, R. M. Godun, M. K. Oberthaler, D. Cassettari, and G. S. Summy, "Quantum enhancement of momentum diffusion in the δ-kicked rotor," Phys. Rev. Lett. **87**, 074102 (2001).

[47] M.B. d'Arcy, R.M. Godun, G.S. Summy, K. Burnett, and S.A. Gardiner, "Approaching classicality in quantum accelerator modes through decoherence," Phys. Rev. E **64**, 056233 (2001).

[48] M. B. dArcy, R. M. Godun, D. Cassettari, and G. S. Summy, "Accelerator-mode-based technique for studying quantum chaos," Phys. Rev. A **67**, 023605 (2003).

[49] S. Schlunk, M.B. dArcy, S.A. Gardiner, D. Cassettari, R.M. Godun, and G.S. Summy, "Signatures of quantum stability in a classically chaotic system," Phys. Rev. Lett. **90**, 054101 (2003).

[50] S. Schlunk, M.B. dArcy, S.A. Gardiner, D. Cassettari, R.M. Godun, and G.S. Summy "Signatures of quantum stability in a classically chaotic system,", Phys. Rev. Lett. **90**, 124102 (2003).

[51] M.B. dArcy, R.M. Godun, G.S. Summy, I. Guarneri, S. Wimberger, S. Fishman, and A. Buchleitner, "Decoherence as a probe of coherent quantum dynamics," Phys. Rev. E **69**, 027201, (2004).

[52] M.B. dArcy, G.S. Summy, S. Fishman, and I. Guarneri, "Novel quantum chaotic dynamics in cold atoms," Physica Scripta **69**, C25 (2004).

[53] Z.-Y. Ma, M. B. d'Arcy, S. A. Gardiner, "Gravity-sensitive quantum dynamics in cold atoms," Phys. Rev. Lett. **93**, 164101 (2004).

[54] S. N. Bose, "Plancks Gesetz und Lichtquantenhypothese," Zeitschrift f*ü*r Physik **26**, 178 (1924).

[55] Albert Einstein, "Qunatentheorie des einatomigen idealen gases," Diese. Ber. **22** 261 (1924).

[56] Albert Einstein, "Qunatentheorie des einatomigen idealen gases. Zweite abhandlung," Sitzungsber. Preuss. Akad. Wiss., Bericht **1**, 3, (1925).

[57] Albert Einstein, "Zur quantentheorie des idealen gases," Sitzungsber. Preuss. Akad. Wiss., Bericht **3**, 18 (1925).

[58] F. London, "The λ-Phenomenon of Liquid Helium and the Bose-Einstein Degeneracy," **643**, 643 (1938).

[59] F. London, "On the Bose-Einstein Condensation," Phys. Rev. **54**, 947 - 954 (1938).

[60] M. H. Anderson, J. R. Ensher, M. R. Matthews, C. E. Wieman, and E. A. Cornell, "Observation of Bose-Einstein Condensation in a dilute atomic vapor," Science, **269**, 198 (1995).

[61] K. B. Davis, M. -O. Mewes, M. R. Andrews, N. J. van Druten, D. S. Durfee, D. M. Kurn, and W. Ketterle, "Bose-Einstein Condensation in a gas of Sodium atoms," Phys. Rev. Lett. **75**, 3969 (1995).

[62] Franco Dalfovo, Stefano Giorgini, Lev P. Pitaevskii, Sandro Stringari, "Theory of Bose-Einstein condensation in trapped gases," Rev. Mod. Phys. **71**, 463 (1999).

[63] A. Ashkin, "Trapping of Atoms by Resonance Radiation Pressure," Phys. Rev. Lett. **40**, 729 (1978).

[64] D. Wineland, R. Drullinger and F. Walls, "Radioation-pressure cooling of bound resonant absorbers," Phys. Rev. Lett. **40**, 1639 (1978).

[65] W. Neuhauser, M. Hohenstatt, P. Toschek, and H. Dehmelt, "Optical side band cooling of visible atom cloud confined in parabolic well," Phys. Rev. Lett. **41**, 233 (1978).

[66] W. D. Phillips, and H. Metcalf, "Laser deceleration of an atomic beam," Phys. Rev. Lett. **48**, 596 (1982).

[67] John V. Prodan, William D. Phillips, and Harold Metcalf, "Laser Production of a Very Slow Monoenergetic Atomic Beam," Phys. Rev. Lett. **49**, 1149, (1982)

[68] A. Migdall, J. Pradan. W.Phillips, T. Bergeman and H.Metcalf, "First observation of magnetically trapped neutral atoms," Phys. Rev. Lett. **54** 2596 (1985).

[69] Steven Chu, L. Hollberg, J. E. Bjorkholm, Alex Cable, and A. Ashkin, "Three-dimensional viscous confinement and cooling of atoms by resonance radiation pressure," Phys. Rev. Lett. **55**, 48 (1985).

[70] S. Chu, J.E. Bjorkholm, A. Shkin, and A. Cable, "Experimental observation of optically trapped atoms," Phys. Rev. Lett. **57** 314 (1986).

[71] E. L. Raab, M. Prentiss, Alex Cable, Steven Chu, and D. E. Pritchard, "Trapping of Neutral Sodium Atoms with Radiation Pressure," Phys. Rev. Lett. **59**, 2631 (1987).

[72] P. D. Lett, R. N. Watts, C. I. Westbrook, W. D. Phillips, P. I. Gould and H. J. Matcalf, "Observation of atoms laser cooled below the Doppler limit," Phys. Rev. Lett. **61**, 169 (1988).

[73] J. Dalibard and C. Cohen-Tannoudji, "Laser cooling below the doppler limit by polarization gradients: simple theoretical models," J. Opt. Soc. Am. B, **6**(11) (1989).

[74] K.B. Davis, M.-O. Mewes, M.A. Joffe, M.R. Andrews, and W. Ketterle "Evaporative cooling of sodium atoms," Phys. Rev. Lett. **74**, 5202 (1995); Erratum: Phys. Rev. Lett. **75**, 2909 (1995).

[75] W. Ketterle and N.J. van Druten, "Evaporative cooling of atoms," Advances in Atomic, Molecular, and Optical Physics, edited by B. Bederson and H. Walther, **37**, 181 (1996).

[76] S. Fishman, I. Guarneri, L. Rebuzzini, "Stable quantum resonances in atom optics," Phys. Rev. Lett., **89**, 084101 (2002).

[77] S. Fishman, I. Guarneri, L. Rebuzzini, " A theory for quantum accelerator modes in atom optics," J. Stat. Phys. **110**, 911 (2003).

[78] A. Buchleitner, M. B. d'Arcy, S. Fishman, S. A. Gardiner, I. Guarneri, Z.-Y. Ma, L. Rebuzzini, G. S. Summy, "Quantum Accelerator Modes from the Farey Tree," Phys. Rev. Lett., **96**, 164101 (2006).

[79] Italo Guarneri, Laura Rebuzzini, and Shmuel Fishman, "Arnol'd tongues and quantum accelerator modes," Nonlinearity **19**, 1141 (2006).

[80] M. Jensen, P. Bak, T. Bohr, "Transition to chaos by interaction of resonances in dissipative systems. I. Circle maps," Phys. Rev. A **30**, 1960 (1984).

[81] S. Schlunk, M. B. dArcy, S. A. Gardiner, and G. S. Summy, "Experimental Observation of High-Order Quantum Accelerator Modes," Phys. Rev. Lett. **90**, 124102 (2003).

[82] Z. -Y. Ma, K. Burnett, M. B. d'Arcy, and S. A. Gardiner, " Quantum random walks using quantum accelerator modes" Phys. rev. A **73**, 013401 (2006).

[83] Brian P. Timmons, "Dynamics of kicked laser cooled rubidium atoms," Doctoral thesis, Oklahoma State University, July 2006.

[84] Daniel A. Steck, "Rubidium 87 D line data," available online at `http://steck.us/alkalidata` (revision 2.0.1, 2 May 2008).

[85] Peyman Ahmadi, "Investigating optical atom traps for Bose-Einstein Condensation," Doctoral thesis, Oklahoma State University, July 2006.

[86] William D. Phillips, "Nobel Lecture: Laser cooling and trapping of neutral atoms," Rev. Mod. Phys. **70**, 721 (1998).

[87] P. L. Gould, P. D. Lett and W. D. Phillips, "New measurements with Optical Molasses," in *Laser Spectroscopy VIII*, W. Pearsson, S, Svanberg, Ed. (Springer-Verlag, Berlin 1987) p.64.

[88] Harold J. Metcalf and Peter van der Straten, "Laser Cooling and Trapping," Springer-verlag, New York 1999.

[89] Michael Brendan d'Arcy, "Quantum chaos in atom optics," DPhil thesis, University of Oxford, Oxford, United Kingdom, (2002).

[90] C. E. Creffield, S. Fishman, and T. S. Monteiro, " Theory of 2 δ-kicked quantum rotors," Phys. Rev. E **73**, 066202 (2006).

[91] P. H. Jones, M. M. Stocklin, G. Hur, and T. S. Monteiro, "Atoms in Double-δ-Kicked Periodic Potentials: Chaos with Long-Range Correlations," Phys. Rev. Lett. **93**, 223002 (2004).

[92] M.D. Barrett, J.A. Sauer, and M.S. Chapman, "All-optical formation of an atomic Bose-Einstein condensate," Phys. Rev. Lett, **87**, 010404 (2001).

[93] Murray D Barrett, "A QUEST for BEC : An all optical alternative," Doctoral thesis, Georgia Institute of Technoology, May 2002.

[94] Toshiya Kinoshita, Trevor Wenger, and David S. Weiss, " All-optical Bose-Einstein condensation using a compressible crossed dipole trap," Phys. Rev. A **71**, 011602(R) (2005).

[95] Peyman Ahmadi, Vijayashankar Ramareddy, Gil S. Summy, "Multiple micro-optical atom traps with a spherically aberrated laser beam," New J. Phys. **7**, 4 (2005).

[96] C. C. Bradley, C. A. Sackett, J. J. Tollett, and R. G. Hulet, "Evidence of Bose-Einstein Condensation in an atomic gas with attractive interactions," Phys. Rev. Lett. **75**, 1687 (1995).

[97] C. C. Bradley, C. A. Sackett, J. J. Tollett, and R. G. Hulet, "ERRATA: Evidence of Bose-Einstein Condensation in an Atomic Gas with Attractive Interactions," Phys. Rev. Lett. **75**, 1687 (1995)

[98] C. C. Bradley, C. A. Sackett, and R. G. Hulet, "Analysis of in situ images of Bose-Einstein condensates of lithium," Phys. Rev. A **55**, 3951 (1997).

[99] M. Born and E. Wolf "Principles of Optics," 7th edn (Cambridge: Cambridge University Press), (1999).

[100] A. Yoshida, T. Asakura,"Diffraction patterns of off-axis gaussian beams in the presence of third-order spherical aberration in the optical system," Opt. Comm, **19**, 387 (1976).

[101] Jixiong Pu, Huihua Zhang, "Intensity distribution of Gaussian beams focused by a lens with spherical aberration," Optics Communications **151**, 331 (1998).

[102] W. T. Welfold "Aberrations of the Symmetrical Optical System," (London: Academic) (1974).

[103] Peyman Ahmadi, Brian P. Timmons, and Gil S. Summy, " Geometrical effects in the loading of an optical atom trap," Phys. Rev. A **72**, 023411 (2005).

[104] Ghazal Behin-aein, Vijayashankar Ramareddy, Peyman Ahmadi, Gil S Summy, "Exploring the phase space of the quantum delta kicked accelerator," Phys. Rev. Lett. **97**, 244101 (2006).

[105] Itzhack Dana, Vijayashankar Ramareddy, Ishan Talukdar, and Gil S. Summy, " Experimental realization of quantum-resonance ratchets at arbitrary quasi-momenta," Phys. Rev. Lett. **100**, 024103 (2008).

[106] R. E. Sapiro, R. Zhang, G. Raithel, "1-D Mott insulator transition of a Bose-Einstein condensate," arXiv:0805.0247v1 [physics.atom-ph], 2008.

[107] J. F. Kanem, S. Maneshi, M. Partlow, M. Spanner, and A. M. Steinberg, " Observation of high-order quantum resonances in the kicked rotor," Phys. Rev. Lett. **98**, 083004 (2007).

[108] Sandro Wimberger, Riccardo Mannella, Oliver Morsch, and Ennio Arimondo, " Resonant nonlinear quantum transport for a periodically kicked Bose Condensate," Phys. Rev. Lett. **94**, 130404 (2005).

[109] M.V. Berry and S. Klein, "Integer, fractional and fractal Talbot effects," J. Mod. Opt. **43**, 2139 (1996).

[110] M.V. Berry, and E. Bodenschatz, "Caustics, multiply reconstructed by Talbot interference," J. Mod. Opt. **46**, 349 (1999).

[111] Vijayashankar Ramareddy, Ghazal Behia-aein, Peyman Ahmadi, Ishan Talukdar, Gil S Summy, "High-order resonances of the quantum δ-kicked accelerator" submitted to Euro. Phys. Lett. (2008).

[112] I. Guarneri, L. Rebuzzini, "Quantum accelerator modes near higher-order resonances," Phys. Rev. Lett. **100**, 234103 (2008).

[113] F.M. Izrailev, and D.L. Shepelyanskii, Sov. Phys. Dokl. **24**, 996 (1979); "Quantum resonance for a rotator in a nonlinear periodic field," Theor. Math. Phys. **43**, 553, (1980).

[114] Laura Rebuzzini, Roberto Artuso, Shmuel Fishman, and Italo Guarneri, " Effects of atomic interactions on quantum accelerator modes" Phys. Rev. A **76**, 031603R (2007).

[115] J. Rousselet, L. Salome, A. Ajdari, and J. Prost, "Directional motion of brownian particles induced by a period," Nature (London) **370**, 446 (1994).

[116] L. P. Faucheux, L. S. Bourdieu, P. D. Kaplan, and A. J. Libchaber, "Optical thermal tatchet," Phys. Rev. Lett. **74**, 1504 (1995).

[117] P. Hänggi, F. Marchesoni, and F. Nori, "Brownian motors," Ann. Phys. (Leipzig), **14**, No 1-3,51 (2005).

[118] H. Linke, W. Sheng, A. Löfgren, H. Xu P. Omling and P. E. Lindelof, "A quantum dot ratchet: Experiment and theory," Europhys. Lett., **44**, (3), 341 (1998).

[119] William J. Greenleaf, Michael T.Woodside, and Steven M. Block, "High-Resolution, Single-Molecule Measurements of Biomolecular Motion," Annu. Rev. Biophys. Biomol. Struct. **36**, 171 (2007).

[120] J. Christof M. Gebhardt, Anabel E.-M. Clemen, Johann Jaud, and Matthias Rief, "Myosin-V is a mechanical ratchet," Proc. Nat. Acad. Sci. **103**, 8680 (2006).

[121] I. Andricioaei, A. Goel, D.R. Herschbach and M. Karplus, "Dependence of DNA polymerase replication rate on external forces: A model based on molcular dynamics simulations," Biophys. J., **87**, 1478 (2004).

[122] R Dean Astumian, P Haenggi, "Brownian motors," Physics Today, **55**, 33 (11), (2002).

[123] J. Gong, and P. Brumer, " Generic quantum ratchet accelerator with full classical chaos," Phys. Rev. Lett., **97**, 240602 (2006).

[124] Jiangbin Gong and Paul Brumer, "Directed anomalous diffusion without a biased field: A ratchet accelerator," Phys. Rev E **70**, 016202 (2004).

[125] W.H. Oskay, D.A. Steck, V. Milner, B.G. Klappauf, M.G. Raizen, "Ballistic peaks at quantum resonance," Opt. Comm. **179**,137 (2000).

[126] P. J. Martin, B. G. Oldaker, A. H. Miklich, and D. E. Pritchard, "Bragg scattering of atoms from a standing light wave," Phys. Rev. Lett. **60**, 515 (1988).

[127] M. Kozuma, L. Deng, E. W. Hagley, J. Wen, R. Lutwak, K. Helmerson, S. L. Rolston, and W. D. Phillips, "Coherent splitting of Bose-Einstein Condensed atoms with optically induced Bragg diffraction," Phys. Rev. Lett. **82**, 871 (1999).

[128] J. Stenger, S. Inouye, A. P. Chikkatur, D. M. Stamper-Kurn, D. E. Pritchard, and W. Ketterle, "Bragg spectroscopy of a Bose-Einstein Condensate," Phys. Rev. Lett. **82**, 4569 (1999).

[129] M. Theis, G. Thalhammer, K. Winkler, M. Hellwig, G. Ruff, R. Grimm, and J. Hecker Denschlag, "Tuning the scattering length with an optically induced Feshbach resonance," Phys. Rev. Lett. **93**, 123001 (2004).

[130] D. E. Miller, J. R. Anglin, J. R. Abo-Shaeer, K. Xu, J. K. Chin, and W. Ketterle, "High-contrast interference in a thermal cloud of atoms," Phy. Rev. A **71**, 043615 (2005).

[131] Itzhack Dana and Vladislav Roitberg, "Quantum resonances and ratchets in free-falling frame," Phys. Rev. E **76**, 015201(R) (2007).

[132] V. Ramareddy *et. al.* "Quantum ratchet using a delta kicked accelerator," APS DAMOP L2.00071 (2008).

[133] J. Martin, B. Georgeot, and D. L. Shepelyansky, "Cooling by Time Reversal of Atomic Matter Waves," Phys. Rev. Lett. **100**, 044106 (2008).

[134] Eyal Doron and Shmuel Fishman, "Anderson localization for a two-dimensional rotor," Phys. Rev. Lett. **60**, 867 (1988).

[135] Jiao Wang, Antonio M. Garcia-Garcia, "Anderson transition in a three dimensional kicked rotor," arXiv:0808.4039 (2008).

[136] Andrè R. R. Carvalho and Andreas Buchleitner, "Web-Assisted Tunneling In The Kicked Harmonic Oscillator," Phys. Rev. Lett. **93**, 204101 (2004).

VITA

VIJAYASHANKAR RAMAREDDY

Candidate for the Degree of

Doctor of Philosophy

Thesis: Study of Quantum chaos using a kicked Bose-Einstein condensate

Major Field: Physics

Biographical:

Personal Data: Born in Hosur, TN, India, on June 2, 1978, the son of Rama Reddy and Suguna Ramareddy.

Education: Graduated from RVGB Higher Secondary School, Hosur, India in May 1995; received Bachelor of Science degree in Physics, Chemistry and Mathematics with college topper and 27th rank in university from VVPCS College, Bangalore University, Bangalore, India in May 1999 and received Master of Science degree in Physics with university topper in Bangalore University. Completed the requirements for the Doctor of Philosophy degree with a major in Physics at Oklahoma State University in December 2008.

Professional Memberships: American Physical Society.

Name: Vijayashankar Ramareddy Date of Degree: December, 2008

Institution: Oklahoma State University Location: Stillwater, Oklahoma

Title of Study: QUANTUM CHAOS USING DELTA KICKED SYSTEMS

Pages in Study: 163 Candidate for the Degree of Doctor of Philosophy

Major Field: Physics

Scope and Method of Study: The purpose of this research was to experimentally study quantum dynamics of systems whose classical dynamics are chaotic. Quantum δ-kicked systems such as kicked rotor and kicked accelerator were used. The cold non condensed atoms were kicked first to realize the kicked accelerator. Among the objectives were the realization of resonances of the kicked accelerator and associated phenomena of quantum accelerator modes using a Bose-Einstein Condensation (BEC). One of the major achievements of the work in this thesis was the creation of the quantum δ-kicked rotor and its associated resonances to realize a quantum ratchet. The properties of the ratchet were studied in detail.

Findings and Conclusions: The Quantum Accelerator Modes (QAM) were realized using both thermal samples of atoms and a BEC. Multiple micro optical traps were accidentally observed and in order to understand their behavior a theory was developed using spherical aberration of a lens. The maps produced by an effective classical theory were studied using the QAM. The resonances of the δ-kicked accelerator were observed for the first time and the theory was developed. One of the models that describes the QAM using rephasing of momentum states was observed in the experiments. The ratchet was realized using the resonances of the kicked rotor and accelerator where the diffusion in the case of classical ratchets was replaced by chaos in the quantum ratchet mechanism.

Dr. Gil Summy

ADVISOR'S APPROVAL: _____